Understanding Electronic Structure and Interfaces of Positive Electrodes for Lithium Ion Batteries

by

Pınar Karayaylalı

B.S. Mechanical Engineering

Bilkent University, 2014

SUBMITTED TO THE DEPARTMENT OF MECHANICAL ENGINEERING
IN PARTIAL FULFILLMENT OF THE REQUIREMENTS FOR THE DEGREE OF

MASTER OF SCIENCE IN MECHANICAL ENGINEERING

AT THE

MASSACHUSETTS INSTITUTE OF TECHNOLOGY

June 2016

Signature of Author..... Signature redacted .....
Department of Mechanical Engineering
May 20, 2016

Certified by ..... Signature redacted .....
Yang Shao-Horn
W.M. Keck Professor of Energy
SMART Research Professor of Mechanical Engineering
Thesis Supervisor

Accepted by..... Signature redacted .....
Rohan Abeyaratne
Quentin Berg Professor of Mechanics
Chairman, Department Graduate Committee

Understanding Electronic Structure and Interfaces of
Positive Electrodes for Lithium Ion Batteries

by

Pınar Karayaylalı

Submitted to the Department of Mechanical Engineering
on May 20, 2016 in Partial Fulfillment of the
Requirements for the Degree of Master of Science in
Mechanical Engineering

ABSTRACT

Lithium ion batteries are the currently the best commercial battery in the market and they are used as energy storage devices for mobile phones, laptops, and other portable electronic devices. This is due to their balance of high energy density with high power density compared to other electrochemical energy devices. Also, these days the automotive industry wants to use lithium ion batteries to electric vehicles to reduce the pollution and independence to oil. Although lithium ion batteries are currently one of the best energy storage devices, there is still an ample room for improvement. One of the key parameters to study is electrode/electrolyte interface of electrodes.

EEI on the negative electrode, also known as Solid Electrolyte Interphase (SEI) has the well-known structure with organic and inorganic compounds. Although EEI on negative electrodes is well known, it is not the case for positive electrodes. Numerous studies have been done on positive electrodes; however, there is still a need for systematic study of these interfaces on positive electrodes.

This thesis is about understanding the reactivity and interactions of Li-ion battery positive electrode materials with the electrolyte. By understanding reactions at the EEI, we can develop a way to improve cycle life and safety of lithium ion batteries. To unambiguously pinpoint the electrode/electrolyte interface layers on different positive electrode materials, 100 % active materials are used as positive electrodes instead of composite electrodes.

Thesis Supervisor: Yang Shao-Horn
Title: W.M. Keck Professor of Energy; SMART Research Professor of Mechanical Engineering

ACKNOWLEDGMENTS

I would like to thank my advisor, Prof. Yang Shao-Horn for her guidance and her support throughout this work. She has given me the chance to do the research that was of great interest to me.

I would also like to thank Magali Gauthier who was my mentor in the lab for at least one year and taught me everything in the lab. I am really grateful that she took her time to teach me electrochemistry and show me how to do experiments at EEL.

I am grateful to BMW subgroup for supporting me all the time and they answered my questions diligently and their comments helped me to shape my research. I am looking forward to doing more research in this group.

I would like to express my gratitude to BMW who funded my research. I hope to see this project grow and produce important results in next years.

It has been an enormous pleasure to work with EEL family. I never thought that, people could be this much friendly and supportive in a lab. I hope we will have more social events like tea time and 505 in the future. Especially, I would like to thank Reshma Rao for our meaningless conversations and her support throughout these two years.

Also, many friends far away from Boston have helped me in this journey, many thanks to all of them. They all supported me via our Skype conversations. Last but definitely not least, I would like to thank my family: My parents, my sister, my grandparents and my nephew. I could not have done this without their support.

Table of Contents

LIST OF FIGURES

1 Introduction

1.1 Motivation

During 20th and 21st century, combustion of hydrocarbons has been the main energy source for transportation, but there are problems associated with these energy sources. These problems are the rate of global warming by emission (primarily CO_2) of greenhouse gasses into the atmosphere and limited oil supply. Also, there is a significant increase in energy demand in each year. Because of these reasons, there is a need for new sustainable 'green' energy alternative. Also for a continuous usage, energy storage is necessary. The alternatives to these combustion engines are electrochemical storage devices such as batteries.[1]

Energy storage is necessary to store the energy from renewable energy sources and use them for different applications such as power grid or electrical appliances. Batteries are one of the most important devices for energy storage. Batteries consist of electrochemical cells, which have positive and negative electrodes separated by an electrolyte. These positive and negative electrodes will react chemically and electrochemically, once the battery starts to work.[2]

The critical applications for batteries are electric and hybrid electric vehicles. Electric vehicles use one or more electric motor, which mostly uses batteries as an energy source. Hybrid Electric Vehicles are a combination of standard vehicle and electric vehicle. The idea behind this car is to have both efficiency of using gasoline and the decrease of gasoline consumption. There are types of these HEV and EV which you can plug these vehicles and charge them at night. Today, batteries are used for electric and hybrid

electric vehicles (EV/HEV). Specifically, lithium ion batteries are used for EV/HEV because of their high power and high capacity properties.[3-4]

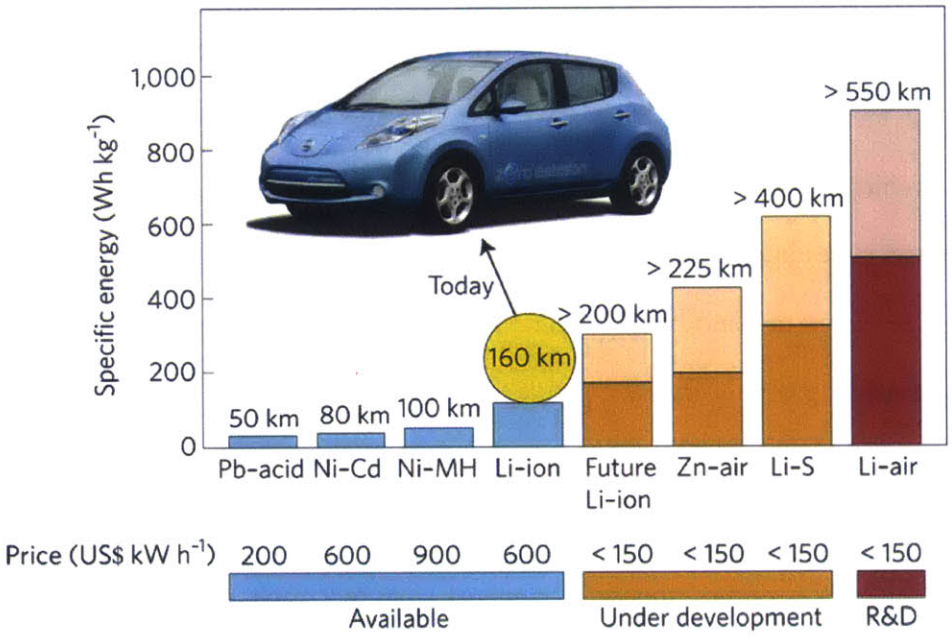

Figure 1. Comparison between different rechargeable batteries with specific energies and estimated driving distances. Lithium ion batteries are the best energy storage devices in the market and there is still a room for improvement.[5]

As it is seen from Figure 1, lithium based batteries are known to have the highest gravimetric and volumetric energy storage capacity when it is compared with to other battery technologies such as the lead-acetate battery, nickel-cadmium battery.[5] Principally, lithium ion batteries are the best commercial battery in the market since lithium has low electronegativity and the lowest weight of all metals. Nevertheless, there is room for improvement. Especially lithium ion batteries are essential for applications that are sensitive to weight and size. For instance, portable electronic devices and telecommunication equipment are two examples that use lithium ion batteries. Companies also want to use lithium ion batteries to electrical vehicles. By having these

battery-powered cars, customers can plug into an electrical plug at night, which would reduce pollution and secure energy independence.[6]

1.2 Principles of Li-ion Batteries

Lithium ion batteries convert energies between chemical and electrical energies. Specifically, electrical energy is generated by redox chemical reaction at the positive and negative electrodes. Energy storage and conversion occur at the same place inside a battery. This means the electrodes are not only the charge-transfer medium but also an active element. Lithium ion batteries consist of positive electrode that is usually $LiCoO_2$ (lithium cobalt oxide) and the negative electrode, which is usually graphite, or lithium metal. It also has non-aqueous, aprotic electrolyte that allows the lithium ion movement. A separator separates the positive electrode and the negative electrode.[7-8]

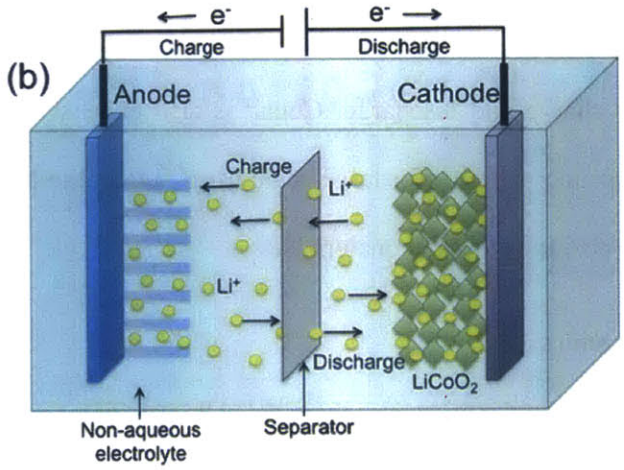

Figure 2. Schematic of a lithium ion battery: The cell consists of positive and negative electrode, non-aqueous electrolyte and a separator. Lithium ion batteries work by lithium insertion-extraction mechanism.[9]

Lithium ion battery operates by the movement of lithium ions and electrons, which can also be called as lithium insertion-extraction mechanism (Figure 2). For charging,

positive electrode delithiates meaning it loses lithium ions to the negative electrode and electrons move to the positive electrode. For discharge, the opposite reactions occur.[10-11] The charge and discharge half-cell and whole cell reactions are:[12]

Positive electrode: $LiMO_2 \rightleftharpoons Li_{1-x}MO_2 + xLi^+$

Negative electrode: $C_6 + xLi^+ + xe^- \rightleftharpoons Li_xC_6$

Whole cell reaction: $LiMO_2 + C_6 \rightleftharpoons Li_{1-x}MO_2 + Li_xC_6$

A typical electrolyte is a mixture of ethylene carbonate (EC) and dimethylcarbonate (DMC) with 1M $LiPF_6$ salt. Half-cell potential of positive electrodes is usually greater than 3 V_{Li} and potential of negative electrodes is closer to 0 V_{Li}. The difference between these potentials is called thermodynamic potential of the cell.[12-13]

For $LiCoO_2$, the current positive electrode used in lithium ion batteries, x is at most can be 0.5 due to safety reasons, which corresponds to 4.2 V_{Li}. Furthermore, Co is relatively toxic and charging $LiCoO_2$ causes safety concerns especially it reacts exothermically during high-power charge and discharge. Cobalt is also expensive, which is the major challenge for lithium ion batteries for large-scale use.[14-15] Because of these reasons, there is a search for new positive electrode materials.

1.2.1 Thermodynamics

The basic thermodynamics for an electrochemical cell is given by:

$$\Delta G = \Delta H - T\Delta S$$

where ΔG is the Gibbs Free Energy, ΔH is the enthalpy, T is the absolute temperature and ΔS is the entropy. $T\Delta S$ term is the heat associated with the reaction. One important aspect of $\Delta G, \Delta S$ *and* ΔH is that they are all state functions. This suggests these functions are only depending on the electrode materials and initial and final states of the reactions.

The Gibbs free energy, ΔG, can be also expressed in terms of electrical energy from a reaction in a battery cell. This equation can be written as:

$$\Delta G = -ZF\varepsilon$$

where ε is the potential of the cell (also can be expressed as open circuit voltage), Z is the number of electrons transferred per mole of reactants and F is the Faraday constant. This equation is crucial because it represents the relation between chemical and electrical driving forces. The ZFε can be expressed as the amount of electricity produced and the total number of materials available for reaction and the voltage determines it.

Another relevant definition for thermodynamics is chemical potential. The chemical potential defines the change of free energy for a given species. Chemical potential can be defined as:

$$\mu_i = \mu_i^0 + RTlna_i$$

where μ_i^0 is the chemical potential in its standard state, R is the gas constant, T is the absolute temperature. In an electrochemical cell, we need to consider the chemical potentials of both positive and negative electrodes. The difference between the chemical potentials of the positive electrode and of the negative electrode can be written as:

$$\mu_{i,products} - \mu_{i,reactants} = RTln\left[\frac{\prod a_{products}}{\prod a_{reactants}}\right]$$

The difference in chemical potentials can also be written as electrical energy, which is also known as Nernst equation:

$$\varepsilon = \varepsilon_o - \frac{RT}{ZF} ln\left[\frac{\prod a_{products}}{\prod a_{reactants}}\right]$$

The Nernst equation relates the cell voltage to the chemical difference across an electrochemical cell. This comparison determines cell potential under non-standard conditions. It compares the effective concentration of the components of a cell reaction to the standard cell potential. [16]

1.2.2 Kinetics

Thermodynamics of a cell defines the equilibrium conditions and gives the maximum energy available for a given reaction. Because of kinetic limitation of reactions, the cell will not have the maximum energy and the voltage drops off because of these constraints. There are three important losses that should be kept in mind for an electrochemical system: Ohmic loss related to resistance of individual cell components; mass transport limitations during cell operation and kinetics of the electrochemical redox reactions taking place at the interface of anode and cathode.

Last type of voltage loss can be best understood by looking into transition state theory. The current flow for this case is usually defined by Butler-Volmer equation. The Butler-Volmer equation is:

$$j = j_o \left\{ exp\left[\frac{\alpha_a Z F \eta}{RT}\right] - exp\left[\frac{\alpha_c Z F \eta}{RT}\right] \right\}$$

where j is the electrode current density, j_o is the exchange current density, η is the activation overpotential, R is the universal gas constant, T is the absolute temperature, Z is the number of electrons involved in the reaction, F is the Faraday constant, α_c is the cathodic charge transfer coefficient and α_a is the anodic charge transfer coefficient.

Butler-Volmer equation explains the electric current on an electrode and it considers both cathodic and anodic reactions occur on the same electrode. It should be noted that Butler-

Volmer is for equilibrium cases and in the case of lithium ion batteries, we should look at non-equilibrium thermodynamics, which is much more complicated than Butler- Volmer equation. For nonequilibrium cases, mathematical modeling is necessary to understand these cases. [17]

1.3 Positive electrode materials

In this section, three types of positive electrode materials for lithium ion batteries are explained in detail: layered oxides, spinel oxides and phosphates.

1.3.1 Phosphates

$LiFePO_4$ is currently the most promising phosphate as positive electrodes in lithium ion batteries, because this is the first positive electrode material with low cost, abundant amount and also environmental friendly. It has the olivine structure, which can be seen in Figure 3. The structure of $LiFePO_4$ is composed of LiO_6 and FeO_6 in the space group Pmna and it is unit cell is orthorhombic. It has lower cost and less toxic than $LiCoO_2$.[18] The theoretical specific charge is about 170 mAh/g[19], but practically this number decreases to 130 mAh/g[15]. The main problem is discharge occurs lower potentials than $LiCoO_2$.

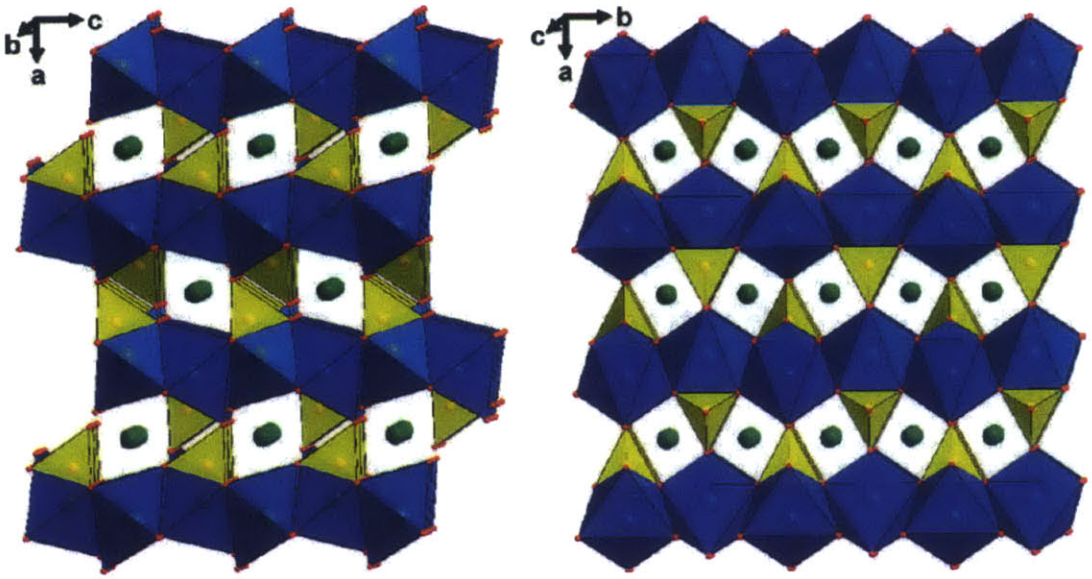

Figure 3. Crystal structure of $LiFePO_4$ with spacegroup Pnma viewed (a) along the b-axis and (b) along the c-axis. The iron octahedral, phosphate tetrahedral and the lithium ions are shown in blue, yellow, and green, respectively.[18]

Lithium extraction occurs in two parts, which are $FePO_4$ growing a shell and shrinking $LiFePO_4$ core. The insertion reaction is a two-phase reaction between $FePO_4$ and $LiFePO_4$. It has a poor electric conductivity because each of these phases is highly stoichiometric with a very low concentration of mixed-valence states. $LiFePO_4$ is an example of material, which has improved properties when the particle size is significantly decreased.[18]

1.3.2 Spinel oxides

One of the important spinel oxides is $LiMn_2O_4$ (Figure 4), which is proposed by Thackeray et al. The general formula of spinels is AB_2X_4 and crystal structure of spinels is based on $MgAl_2O_4$. This material has adopted the structure of Fd3m. The stability of this structure is supplied by the octahedral Mn_2O_4 structure and this possesses a serious of tunnels, which is formed by tetrahedral lithium (8a) and empty octahedral (16c) sites.

Lithium ions diffuse from 8a site to 16c site consequently, which makes a 3D lithium movement.[20]

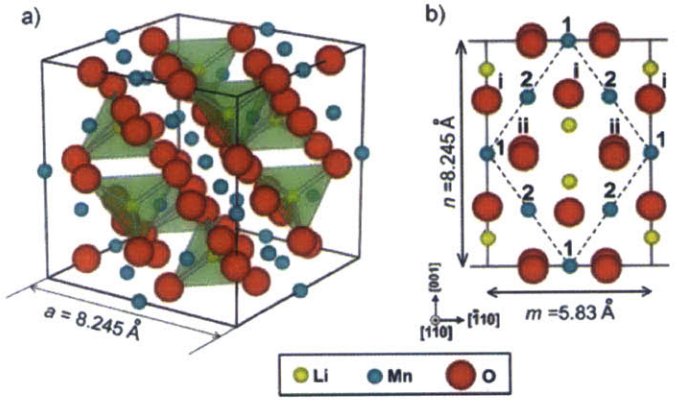

Figure 4. Crystal structure of $LiMn_2O_4$ (a) Unit cell (space group: Fd3m) (b) Projection to [110] zone. The lithium, manganese and oxygen are shown in yellow, green, and red respectively.[20]

During charging, there are two charging plateaus at 4 and 4.15 V_{Li}. There is another plateau around 3 V, however, $LiMn_2O_4$ usually cannot be cycled because of the Jahn-Teller instability of Mn(III). At elevated temperatures, 4 V plateau disappears as well and this means capacity fades at these temperatures. The spinel structure theoretically has a specific charge of 148 mAh/g, but the practical specific charge is between 115 to 125 mAh/g when cycled between 3.5 V_{Li} and 4.3 V_{Li}. This specific capacity is less than $LiCoO_2$; however, it has an advantage relative to cost and manganese is less toxic than cobalt.[7,21]

1.3.3 Layered oxides

1.3.3.1 Conventional layered positive electrodes ($LiMO_2$ compounds)

Layered lithium transition metal oxides, $LiMO_2$ where M= Co, Ni, Mn or combination of there materials, are widely studied as positive electrodes for lithium ion batteries. $LiCoO_2$ is one of the best representations of these kinds of layered oxides, but other examples are $LiNiO_2$ and $LiMnO_2$. The structure of these compounds is isostructural to α-$NaFeO_2$ with the oxygen in the cubic closed-packed arrangement. It is composed of periodic layers of MO_6, M is the transitional metal and LiO_6 alternately stacked. In other words, the lithium and cobalt ions occupy octahedral sites in alternating layers. This structure can be seen in Figure 5.[22]

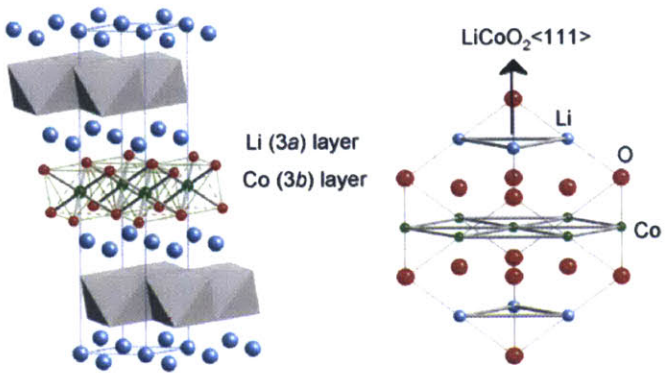

Figure 5. Crystal structure of $LiCoO_2$, which is isostructural to α-$NaFeO_2$ with the oxygen in the cubic closed-packed arrangement. It is composed of periodic layers of MO_6, M is the transitional metal and LiO_6 alternately stacked.[22]

When lithium is completely extracted from positive electrode, x is 1, hexagonal close packing is formed by CoO_2 by rearranging of oxygen layers. As it is known, several phase transition happens when cell is charged to 4.2 V which is approximately when x is 0.5, so full theoretical capacity (~270 mAh/g) cannot be extracted from $LiCoO_2$. The

success of lithium ion batteries is the cycling stability of $LiCoO_2$ when x is between 0 to 0.5. Within this x, this battery can operate over thousand cycles and the capacity is about 140 mAh/g for x= 0.5. [14-15, 23]

Other positive electrode materials has been investigated because of the stability problem of $LiCoO_2$. On the other hand, other positive electrodes such as $LiNi_xCo_yMn_zO_2$ (NMC) and $LiNi_xCo_yAl_zO_2$ (NCA) has better electrochemical performance than LCO, since they have higher capacities at high potentials. One of the important positive materials from this NMC or NCA family is the Ni-rich materials, especially for EV applications. They have high energy density and their cost is lower since nickel and magnesium are cheaper than cobalt. Their theoretical capacity is similar to other positive electrodes; however, the reversible capacities are better than LCO due to the Ni content. For example, for NMC 111 ($LiNi_{1/3}Mn_{1/3}Co_{1/3}O_2$) the reversible capacity is ~163 mAh g^{-1} and this value increases for NMC 811 ($LiNi_{0.8}Mn_{0.1}Co_{0.1}O_2$) and NCA ($LiNi_{0.8}Co_{0.15}Al_{0.05}O_2$) to > 200 mAh g^{-1}.[6] Because of these reasons, a lot of research groups have started investigating these materials to the full extent.

1.3.3.2 Li-rich (Li_2MO_3) compounds

As it is mentioned in previous chapter, conventional Li-ion positive electrode materials such as layered $LiMO_2$ (M = Co, Ni) yields ~140 mAh g^{-1} upon charging to 4.2 V_{Li}. On the other hand, new developments in Li-overstoichiometric layered materials proposes greater reversible capacities around >200 mAh g^{-1} than layered $LiMO_2$.[24] One of the problems with these materials is that their irreversible capacity upon charging to high potentials such as 4.5-4.6 V_{Li}. In few years, new materials were proposed by Tarascon et

al. which are $Li_2(Ru,M)O_3$ (M = Sn and Mn) where they have reversible capacity higher than 200 mAh g^{-1}.[25] This reversible capacity is attributed to the reversible oxidation of oxygen. It has been proposed that bulk oxygen redox can proceed by the reversible oxidation of O^{2-} in the bulk lattice to form O_2^{n-} peroxo-like groups and it is believed that because of this, it avoids O_2 evolution. This new concept opens a new era for lithium ion batteries. [26] The difference between $LiMO_2$ and Li_2RuO_3 is shown in Figure 6.[27-29]

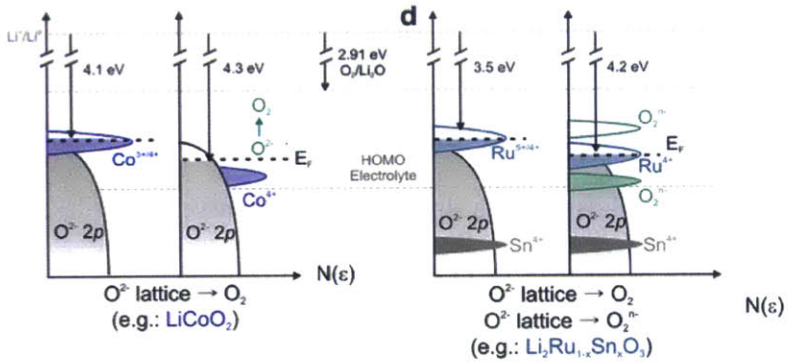

Figure 6. a) Proposed experimental schematic of irreversible anionic oxidation during charging at high potential of $Li_{1-x}CoO_2$ b) Proposed experimental schematic of the reversible anionic oxidation during charge at high potential for $Li_{2-x}Ru_{1-y}Sn_yO_3$.[27-29]

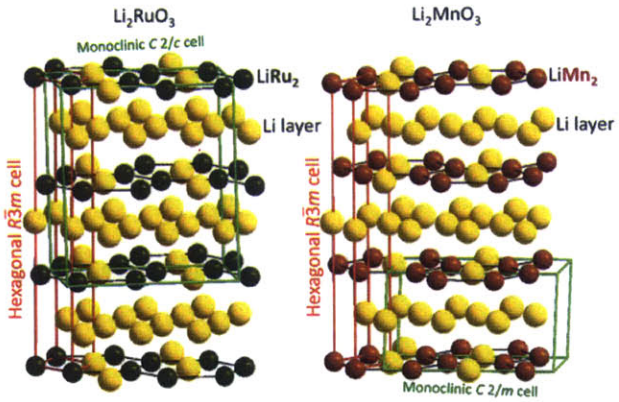

Figure 7. Crystal structure of Li_2RuO_3 and Li_2MnO_3: Lithium, ruthenium and manganese are represented as yellow, green and red respectively. They both have a rocksalt-type structure with the same type of oxide-ion lattice filling. The space groups of Li_2RuO_3 and Li_2MnO_3 are C2/c and C2/m respectively because of a distortion of rocksalt oxygen stacking.[30]

The crystal structures of Li_2RuO_3 and Li_2MnO_3 are seen in Figure 7. Li_2MnO_3 has a rocksalt-type layered structure. The similar structure can be seen at O3-$LiMO_2$ structure. The difference is the ratio of Li:Mn is 1:2 for Li^+ ions lying in the transition metal layers. Similar to Li_2MnO_3, Li_2RuO_3 has a rocksalt structure with the same ratio of Li:Ru. Only difference is the difference between space group definitions for Li_2RuO_3 and Li_2MnO_3. Li_2RuO_3 and Li_2MnO_3 are defined as C2/c and C2/m respectively since Li_2RuO_3 has a distortion of the rocksalt oxygen stacking.[30]

The $Li_2Ru_{1-y}Mn_yO_3$ family has similar crystallographic space groups. Li_2RuO_3 and Li_2RuO_3 have the space group of C2/C and C2/m, respectively. For $Li_2Ru_{0.5}Mn_{0.5}O_3$, it is mostly considered as C2/m but that are some papers suggesting that it might be C2/C as well. Figure 8 shows the transition from C2/C to C2/m.[30]

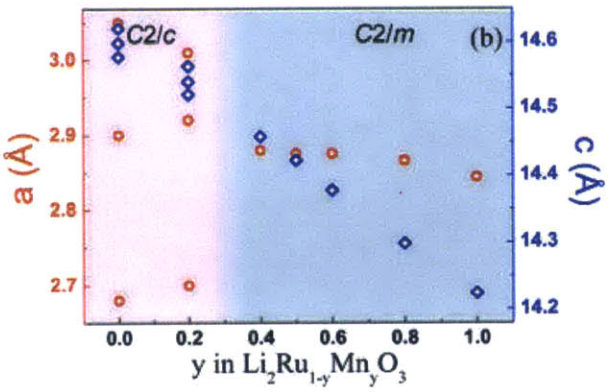

Figure 8. Transition from C2/c to C2/m while increasing Mn content for $Li_2Ru_{1-y}Mn_yO_3$. This transition between C2/m to C2/c is caused by the distortion of the rocksalt oxygen stacking.[30]

When Li_2RuO_3 is charged the first time to 4.6 V_{Li}, until 3.4 V_{Li} - 3.6 V_{Li}, there is a phase transition from monoclinic Li_2RuO_3 to monoclinic $Li_{1.4}RuO_3$and after 3.6 V_{Li} till 3.8 V_{Li}, phase transition from monoclinic $Li_{1.4}RuO_3$ to rhombohedral $Li_{0.9}RuO_3$ occurs. Until this point, there is only oxidation of Ru from Ru^{+4} to Ru^{+5}.[31]After 4.25 V, there is a nucleation

of a disordered phase, which forms the peroxo/superoxo-like species. This region is where the reversible anionic redox occurs and this region is the most interested region for Li_2RuO_3 since this reversible anionic redox does not happen for conventional positive electrode materials[27]

Since today, layered oxide compounds are the most investigated positive electrode materials for lithium ion batteries because $LiCoO_2$ can operate over thousand cycles and it is the only commercial cathode material, but also other new materials such as nickel rich NMC and Li-rich compounds shows better theoretical capacity than any other material.

2 Electrode-Electrolyte Interface (EEI)

During first few cycles, specifically first charging, the electrode-electrolyte interface forms both on the positive electrode and the negative electrode. The formation of a stable EEI layer, conductive to Li^+ but electronically insulating is crucial for high Coulombic efficiency, cycle life and safety.[32-34] However, there is a chance that the non-uniform EEI to form which can lead to battery short and failure because those kinds of EEI causes lithium dendrites formation.[35-37] Because of these reasons, understanding electrochemical and chemical reactions on EEI is crucial to develop a stable and efficient Li-ion batteries.

2.1 Thermodynamics of Electrode-Electrolyte Interface

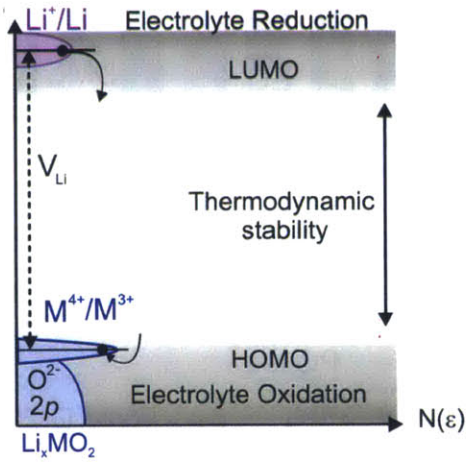

Figure 9. Thermodynamic stability of electrode/electrolyte by checking the difference between electron energy levels that are related to HOMO/LUMO of the electrolyte. Potential range between electrolyte reduction and oxidation are presented in shaded areas.[8,29]

The Figure 9 indicates the thermodynamic stability of the electrode/electrolyte by HOMO (highest occupied molecular orbital) and LUMO (lowest unoccupied molecular orbital) of

the electrolyte. The Fermi level of the negative electrodes, which are usually graphite or lithium metal, is higher than LUMO (lowest unoccupied molecular orbital) of the electrolyte. Thus, there is a thermodynamic driving force to reduce the electrolyte and form electrode-electrolyte interface on negative electrodes.[38-40]

However, for positive electrode, the conditions are different. The Fermi level of the positive electrodes are lower than the LUMO of the electrolyte, so there will not be any reduction of the electrolyte on positive electrodes. However, for high-voltaged positive electrodes (delithiated samples), the Fermi level of the positive electrodes may be lower than HOMO (highest occupied molecular orbital) of the electrolyte, which may cause oxidation of the electrolyte.[41-42]

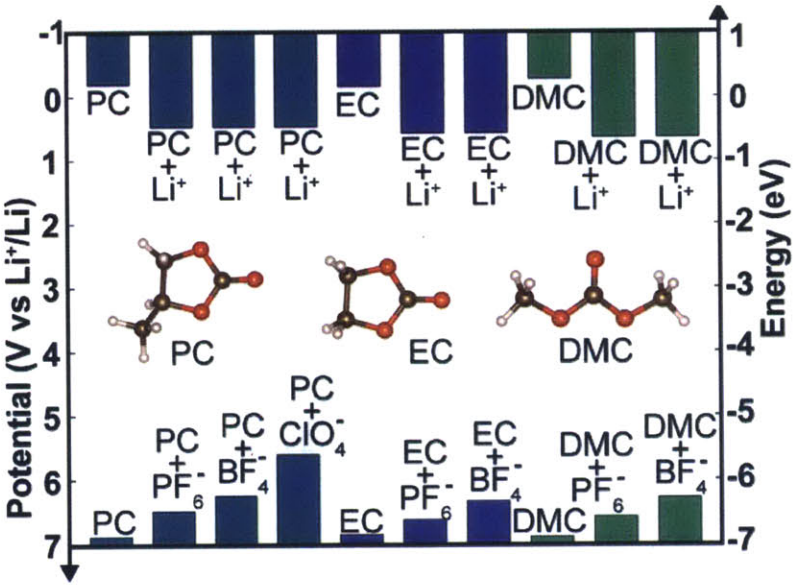

Figure 10. Computed oxidation and reduction of typical Li-ion battery solvents and solvated salts. First adiabatic electron transfer to and from the bulk of the electrolyte is used to estimate the HOMO and LUMO of the electrolytes. Hybrid functional DFT level in Polarizable Continuum Model (PCM) is used to compute the reduction potential that is associated with the LUMO levels. [43-45,29]

In order to have a better understanding of EEI, the HOMO-LUMO levels of the electrolytes should be explored. In this computational study, three electrolytes have been studied which are propylene carbonate (PC), ethylene carbonate (EC) and dimethyl carbonate (DMC). As it is seen from Figure 10, LUMO levels of electrolytes are quite similar. When Li^+ are added to the calculation, LUMO levels of electrolytes are lower than the original circumstance, which means there is a thermodynamic driving force to reduce the electrolyte on the negative electrode. [46-48,29]

On the other hand, if we look at the HOMO levels of the electrolytes, the state is a little bit different. HOMO levels of different electrolytes are quite similar and after salt anions are added to the calculation, the HOMO levels are increased but even with this increase, electrolyte is thermodynamically stable below 5.5 V_{Li}. Experimentally, electrolyte is usually stable between 4.5–6.5 V_{Li}.[49-51,29] These numbers imply that there is no thermodynamic driving force to oxidize the electrolyte at positive electrode. Because of this reason, in addition to these electrochemical reactions, we should also consider chemical reactions for electrolyte decomposition. These chemical reactions can also influence the components on the EEI layer.

2.2 EEI on negative electrodes

EEI on negative electrode is also known as solid electrolyte interphase because it acts like a solid electrolyte: It is electronically insulator but ionic conductor. SEI has been studied lengthily because it protects the negative electrode from co-intercalation of electrolyte solvent molecules. Also, it protects from the consumption of Li-ions in the formation of the layer leading to an irreversible loss of battery capacity.[52]

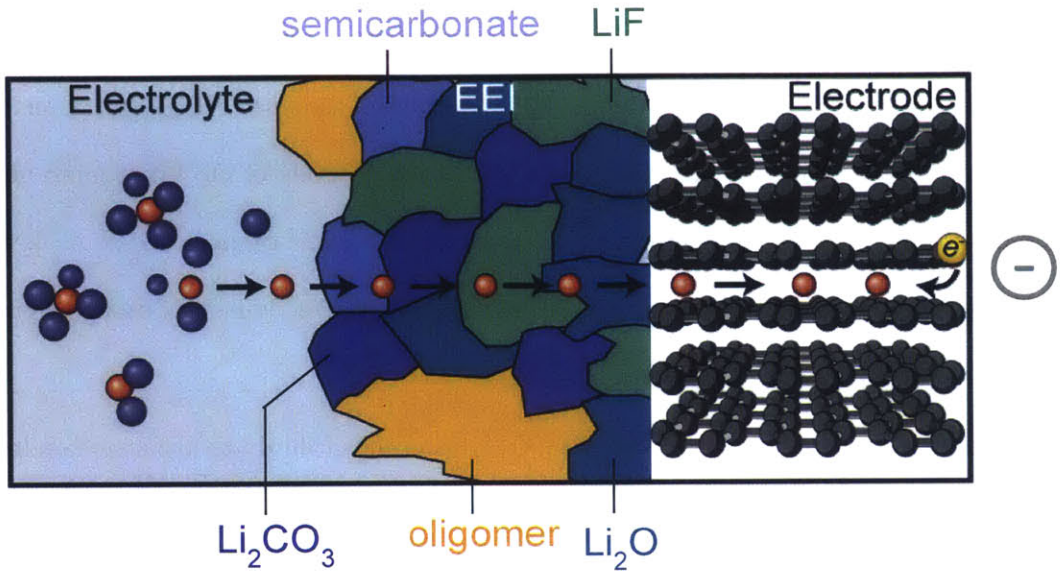

Figure 11. Schematic of the Solid Electrolyte Interphase: It is electronically insulator but ionic conductor. SEI has a well-known structure where inorganic species (LiF, Li_2O) are formed near the negative electrode and oligomers, semicarbonates and Li_2CO_3 are formed close to electrolyte. [53-54,29]

SEI has a well-known structure. The structure can be seen in Figure 11. The SEI mosaic structure consists of multiple inorganic and organic products from electrolyte decomposition. Near the negative electrode, layers are formed of inorganic species like Li_2O, Li_2CO_3 and LiF and these species are thermodynamically stable against the negative electrode. Close to electrolyte, oligomer species and semicarbonates are formed.[53-54]

Aurbach et al.[55-57] showed that the SEI impedance is greatly influenced by salt in the electrolyte. By changing the salt anion, the impedance increases as follows: $PF_6^- > BF_4 > ClO_4^-$. The impedance PF_6^- impedance is twice as ClO_4^-. Also, with $LiPF_6$ salt, the formation of EEI is faster than $LiBF_4$ and $LiClO_4$. This corresponds that the EEI layer

influences the impedance of the system. This impedance is attributed to higher concentration of LiF, which is known as highly resistive material.

Formation of a dendrite is affected by the composition of the electrolyte. In order to form a stable SEI, the usage of highly concentrated electrolytes based on ether or amids is required. This is critical to have a stable SEI, which would increase the safety and the Coulombic efficiency of the cell.[58-59]

2.3 EEI on positive electrodes

There has been a research EEI on positive electrodes for at least four decades; however, there is a little understanding on what different components form on EEI and how this influences the EEI layer properties. Especially, recent studies on Li_2MO_3 [27-28] indicate that there is a need for systematic study for EEI layers on positive electrodes. These kinds of study will determine the key for reducing the electrolyte reactivity with the electrode, which can affect the battery life and safety as exothermic reactions of positive electrodes. As it is stated in previous chapters, there is no thermodynamic driving force to oxidize electrolyte on most conventional positive electrode materials. There are few studies, which revealed surface films on positive electrodes. The first group, which suggested EEI layer on positive electrode, was Goodenough et al.[60] The detailed history of EEI study of positive electrodes can be seen at Figure 12.[29] After Goodenough numerous studies has been done by different groups. The structure of EEI layer usually consists of similar compositions as at SEI on negative electrodes, although mostly it is proposed that mostly EEI layer is formed by chemical reactions, i.e. nucleophilic attack.

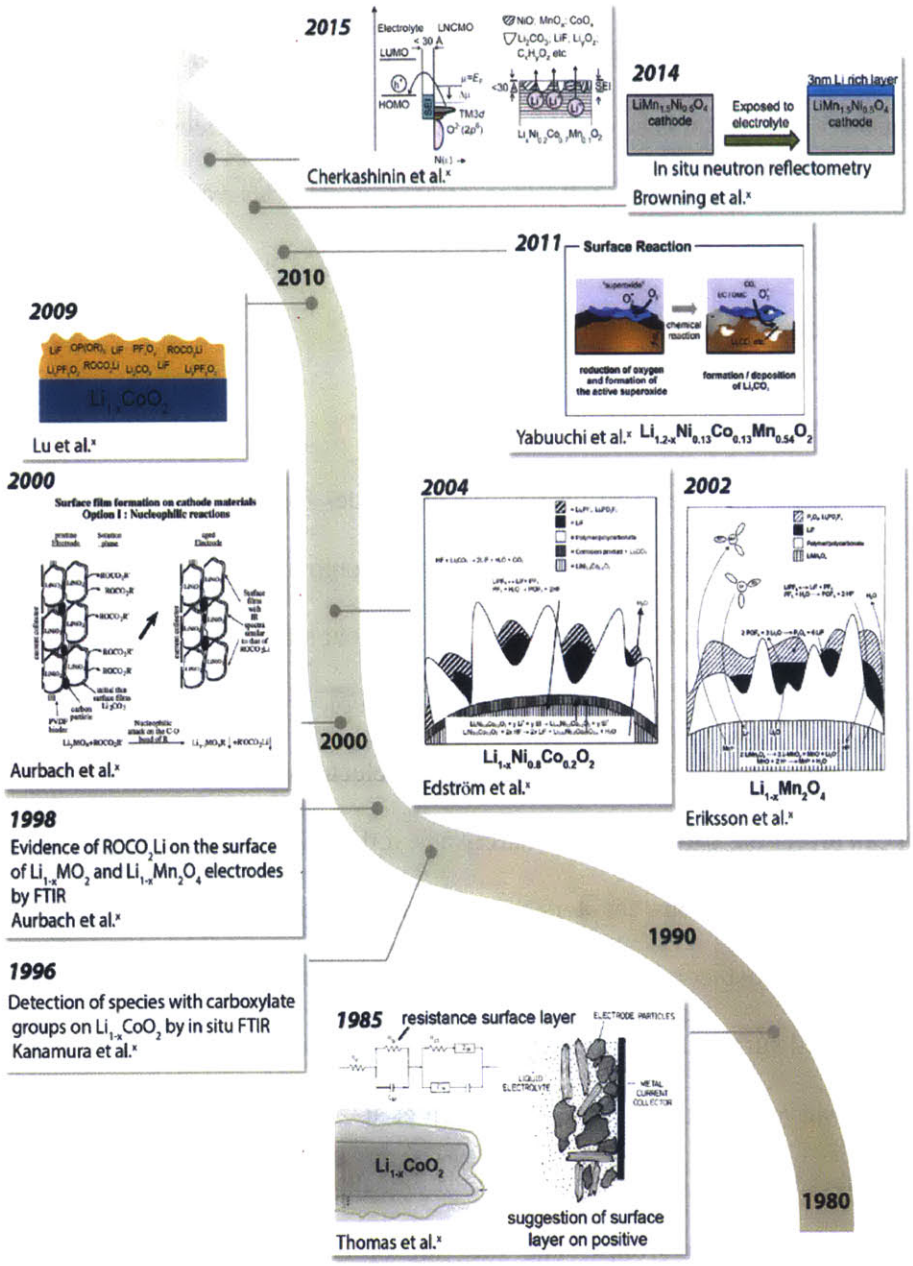

Figure 12. Evolution of EEI layer studies on positive electrodes: Firstly, Goodenough et al.[60] reported a surface layer on $Li_{1-x}CoO_2$. Carboxylates on $Li_{1-x}CoO_2$ and $ROCO_2Li$ on $Li_{1-x}MO_2$ and $Li_{1-x}Mn_2O_4$ electrodes are reported by Kanamura et al.[61] and Aurbach et al.[62,63] XPS measurements are done by Erikkson et al.[64], Edström et al.[65] and Lu et al.[66] Further systematic studies are necessary to fully understand the EEI layers on positive electrode.[29]

The presence of carboxylate groups (O-C=O) while cycling $Li_{1-x}CoO_2$ has been shown by Kanamura et al.[61]. They used in situ FTIR technique to see these carboxylate groups on the EEI layer of $LiCoO_2$. On the surface of $Li_{1-x}MO_2$ and $Li_{1-x}Mn_2O_4$ electrodes, the presence of semicarbonates ($ROCO_2Li$) is found by Aurbach et al[62.63]. The formation of semicarbonates is due to the nucleophilic reactions of the surface on the electrode with the electrolyte. EEI layer models of cycled oxide electrode composites are further developed from XPS studies including Erikkson et al.[64], Edström et al.[65] and Lu et al.[66]

A new idea has been proposed by Yabuuchi et al.[67] that is the reduction of superoxide from O_2 release from $0.5Li_{2-x}MnO_3 \bullet 0.5Li_{1-x}Co_{0.33}Ni_{0.33}Mn_{0.33}O_2$. After this reduction process, superoxide can attack to electrolyte to form Li_2CO_3. Also, in situ techniques have helped to understand EEI layer on the positive electrode as well. For instance the techniques such as neutron reflectrometry and synchrotron XPS and XAS is used for EEI layer. Browning et al.[68] used in situ neutron reflectometry to reveal the EEI layers on $Li_{1-x}Mn_{1.5}Ni_{0.5}O_4$ thin films are ~3 nm in thickness and predominated by fluorides and P-O-containing species. Cherkashinin et al.[69] employ in situ synchrotron XPS and XAS to show EEI layers on cycled $Li_{1-x}Ni_{0.2}Co_{0.7}Mn_{0.1}O_2$ thin films that consists of lithium oxides, fluorides and carbonates.

2.3.1 Chemical Reactions

Nucleophilic attack means the ability of the oxygen ion to donate a pair of electrons to form a new chemical bond with a solvent molecule. This is also known as nucleophilicity or Lewis basicity of the oxygen. As electronegativity on metal oxide surfaces increases, nucleophilicity increases as well. This could also be interpreted as the greater the covalency of M-O bonds, increased nucleophilicity that metal oxide surfaces have. From this information, we can hypothesize that nucleophilicity of oxygen atoms in $LiMO_2$ increases from early transition metals to late transition metals. As an example, nucleophilicity of oxygen in $LiNiO_2$ is better than $LiCoO_2$.[29]

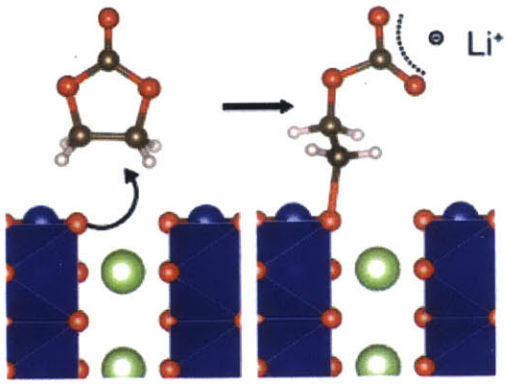

Figure 13. Nucleophilic attack of an EC molecule: Ring opening of carbonates as a result of nucleophilic attack. Nucleophilic attack is the ability of the oxygen ion to donate a pair of electrons to form a new chemical bond. Oxygen anionic redox of high-capacity positive electrodes can be explained by nucleophilic of electrolytes. [29]

Aforementioned, the nucleophilic attack is critical to understand the electrolyte decomposition on the positive electrode. This attack usually leads to ring opening (that can be seen in Figure 13) of cyclic carbonates that result in decomposition of electrolyte to semicarbonates and Li alkoxides (ROLi).[70,29]

It is mostly hypothesized that LiF is not formed by electrochemical reactions but chemical reaction. There are a couple of proposed reactions. These are listed below:

$$LiPF_6 \rightarrow LiF + PF_5$$

$$LiPF_6 + Li_2CO_3 \rightarrow 3LiF + POF_3 + CO_2$$

$$PF_5 + Li_2CO_3 \rightarrow 2LiF + POF_3 + CO_2$$

$$Li_2CO_3 + HF \rightarrow 2LiF + CO_2 + H_2O$$

It is always important to keep in mind these reactions since as it is mentioned earlier; there is no thermodynamic driving force for electrolyte decomposition, so chemical reactions are important factors for our analysis.

2.3.2 Electrochemical Reactions

For high potentials, we might expect to have electrochemical reactions since the Fermi level of the positive electrode may be below the HOMO of the electrolyte and this might result in electrolyte oxidation. However, there is no strong indication of electrochemical reactions on the positive electrode.

To understand these reactions better, Density Functional Theory (DFT) calculations were done by different groups to understand which electrochemical reactions might be possible on the positive electrode.

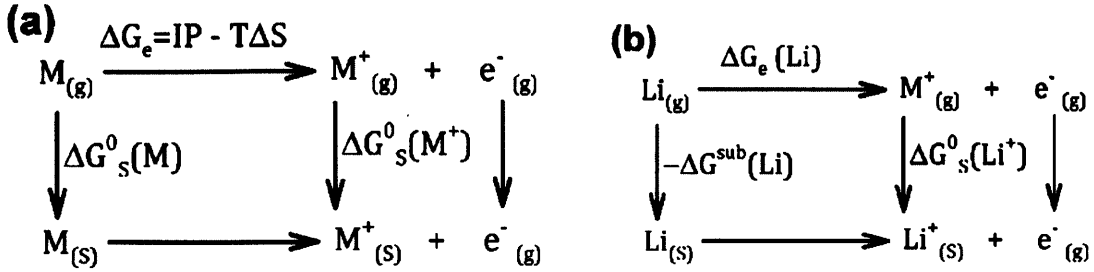

Figure 14. Gibbs Free Energy calculations for the reaction $M \rightarrow M^{+} + e^{-}$: $M_{(g)}$ denotes gas phase, $M_{(s)}$ stands for solvated molecule and IP denotes ionization potential. These calculations are done in order to find which reactions are favorable for electrode/electrolyte interface.[71]

For instance, Borodin et al.[43-45,71] made some calculations for different electrochemical reactions to check the stability of the electrolyte against positive electrodes. In these DFT calculations, they test different scenarios and they look if these reactions are favorable or not. The summary of these calculations can be seen in Figure 14. If Gibbs free energy is less than 0, it means that the reaction is spontaneous (or favorable). After these calculations, a few reactions have been proposed:

$$PF_6^- + (CH_2O)_2C{=}O \rightarrow CH_2CHOH + CO_2 + PF_5 + HF$$

or

$$PF_6^- + (CH_2O)_2C{=}O \rightarrow CH_3CHO + CO_2 + PF_5 + HF$$

$$HF + Li_2CO_3 \rightarrow 2LiF + CO_2 + H_2O$$

Still, more theoretical studies should be done on this topic, since the effect of electrochemistry is quite puzzling.

2.3.3 Anionic redox of layer oxides

One of the important parameters for surface reactivity is oxygen anionic redox and it is not well understood. When the redox energy levels of transition metal ions pin or fall

below the top of oxygen p band, there is a thermodynamic driving force for oxygen redox in addition to redox of transition metals. The oxidation of O^{2-} to O^{-} can proceed by forming ligand hole in the O p band, which can lead to the formation of peroxide anions O_2^{2-} on the surface. These peroxide anions on the surface can react further to form molecular oxygen.[27-28, 72-73]

For anionic redox of $LiCoO_2$, Tarascon et al. and Goodenough et al. made two important hypotheses. According to Tarascon et al., once lithium is extracted from $LiCoO_2$, layered CoO_2 forms that mean oxidation of Co from Co^{3+} to Co^{4+}. Co^{3+} is leveled around sp antibonding level, whereas Co^{4+} is the d level falling to these sp antibonding level and O^{2-} species will not form from this which can be seen in Figure 15. But it should be also realized; there will be small amount of cobalt to form $Li_xCo_{1-y}O_2$. As a result, formation of peroxo-like species with these reactions below is suggested by Tarascon et al.[72]

Oxygen oxidation: $4yO^{2-} \rightarrow 2y(O_2)^{2-} + 4ye^{-}$

Overall reaction: $LiCoO_2 \rightarrow Li_xCo_{1-y}O_2$

$$Li_xCo_{1-y}O_2 \rightarrow Co_{1-y}O_{2-4y}^{2-}(O_2)_{2y}^{2-}$$

Goodenough and Kim et al. suggested that when the $LiCoO_2$ is charged to higher potentials, Co 3d band will start to go down and at some point, this d band will pin to O 2p band and get fall below the O 2p band. This results in peroxide formation at the surface and these peroxides will form oxygen gas[73]:

$$2(O_2)^{2-} \rightarrow 2O^{2-} + O_{2(g)} \uparrow$$

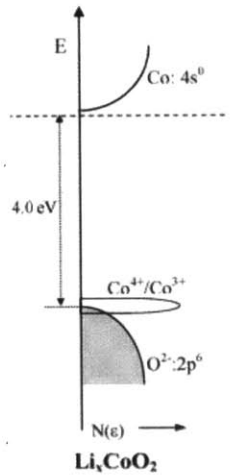

Figure 15. Schematic of oxygen anionic redox during charging of $Li_{1-x}CoO_2$ due to the overlap of the Fermi level with the O *p* band.[73]

There are two oxygen redox reactions on the chemistry of EEI layers that we need look into. First one is the $O^{2-}/O_2^{-}/O_2^{2-}$ on the surface attacks carbonate solvents and solvated ions at high voltages (Figure 16). The presence of superoxo/peroxo on the surface at high potentials might have reactivity with the electrolyte. One likelihood is the effect of nucleophilicity to the electrolyte. Second one is superoxide (O_2-) attacks carbonate solvents and PVDF (at voltages lower than 3 V_{Li}). O_2 release on charge reduced to superoxide on discharge, which reacts with carbonate solvents and PVDF. The release of O_2 on charge further reduced to superoxide on discharge. Superoxide attacks carbonates solvents to form Li_2CO_3 for example, as seen in Li-air.

For this thesis purposes, we will focus on the first one because in our experiments, we only charge our positive electrodes to different voltages to see the effect of first charging to electrolyte. [67]

2.4 Open Question

Many open questions remain about oxygen anionic redox. There are still ambiguities concerning the change of oxidation state of Ru ions during delithiation to $Li_{2-x}RuO_3$[27-28]. Additionally, it is not understood why reversible oxygen redox is possible in second row transition metal oxides, while irreversible oxygen gas evolution is observed in most of the first row transition metal oxides. However, as it is known, second row transition metals such as ruthenium is non-abundant and expensive, because of this reason there is a need to study abundant materials for lithium ion batteries.

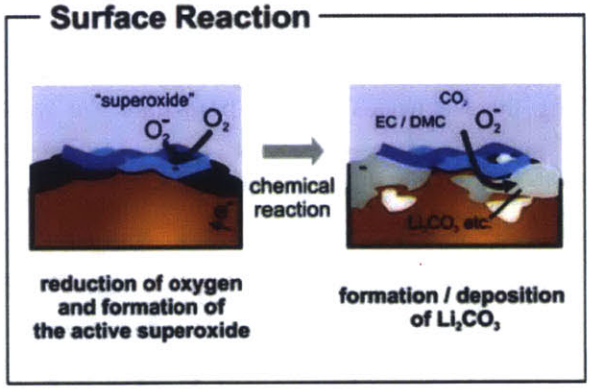

Figure 16. Surface reaction of oxygen on the surface of $0.5Li_2MnO_3$-$0.5LiCo_{1/3}Ni_{1/3}Mn_{1/3}O_2$ ($Li_{1.2}Co_{0.13}Ni_{0.13}Mn_{0.54}O_2$) cathode material and formation of superoxide that might lead to form Li_2CO_3 by chemical reactions.[67]

Moreover, $O^{2-}/O_2^-/O_2^{2-}$ on the surface attacks carbonate solvents and solvated ions at high voltages (Figure 16). These highly reactive species such as O_2, superoxide or O_2^{n-} can lead to electrolyte decomposition and impedance growth upon cycling. It is not still know how stable are these oxygen species ($O^{2-}/O_2^-/O_2^{2-}$) on the surface of the positive electrode and how do they have an influence on the formation of EEI layer. One idea might be the presence of superoxo/peroxo on the surface at high potentials might have reactivity with

the electrolyte. The other question might be can nucleophilic attack have an influence on this reaction with electrolyte. Because of these questions, further studies are needed to understand these different behaviors of oxygen anionic redox.

2.5 Hypothesis and Research Approach

In order to understand electrode/electrolyte interface on the positive electrode together the influence of oxygen anionic redox to this interface, two important spectroscopy techniques are used (Figure 17). First one is X-Ray Photoelectron Spectroscopy (XPS). With X-Ray photoelectron spectroscopy, we want to see the formation of layer by electrolyte decomposition by charging positive electrodes to different potentials. Especially by charging the electrodes to high potentials, we want to see the effect of oxygen anionic redox to the surface of the positive electrode.

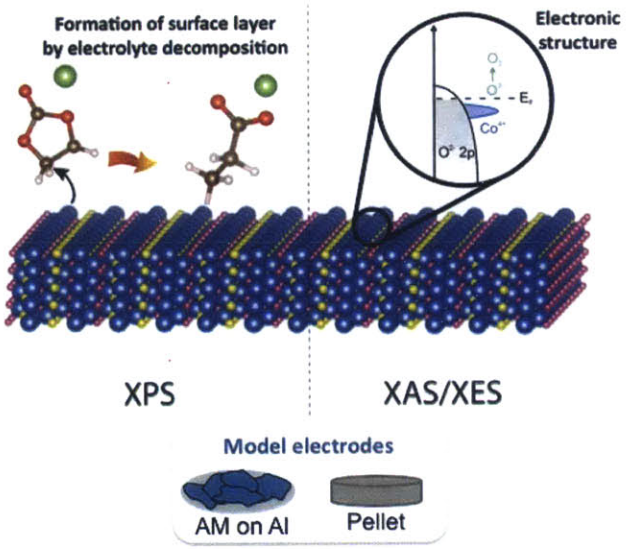

Figure 17. Our research approach for understanding EEI layers on positive electrodes: XPS is used to see the formation of surface layer by electrolyte decomposition by charging these electrodes to different potentials. XAS/XES are used to understand the electronic structure and oxygen anionic redox on different cathode materials. For these measurements, model electrodes are used rather than composite electrodes. Courtesy of Magali Gauthier.

Second important techniques are X-ray Absorption and Emission Spectroscopy. With these techniques, whole electronic structure of a material can be learned. The idea is to find electronic structures of different positive electrodes and to see how these electronic structures changes as different potentials are applied to these electrodes. These measurements will give us information about the partial density of states of the positive electrodes during charging. The electronic structure will be correlated with the formation of the species such as O_2 or peroxo-like species and their influence on the electrode/electrolyte interface.

After doing XPS and XAS/XES measurements we came up with a hypothesis that relates the oxygen anionic redox with electrode/electrolyte interface on the positive electrode. Our hypothesis is increasing the number of d electrons (from Mn to Co and Ni) or decreasing the Li content (thus increasing the metal oxidation state) enhances the M-O bond covalency and activates the lattice oxygen promoting the electrolyte decomposition.

3 Experimental Procedures

To have a better understanding on EEI layer on positive electrodes, several techniques have been used such as X-Ray Photoelectron Spectroscopy (XPS), X-ray diffraction (XRD), atomic force microscopy (AFM), scanning tunneling microscopy (STM) and Fourier transform infrared spectroscopy (FTIR). In this work, three principal techniques were used: X-Ray Photoelectron Spectroscopy (XPS), X-Ray Absorption Spectroscopy (XAS) and X-Ray Emission Spectroscopy (XES). These measurements were done with model electrodes with no carbon and no binder.

3.1 Model electrodes

For the studies of EEI on positive electrodes, usually composite electrodes are used. Composite electrodes have active material, carbon additives and binders. Although, in composite electrodes, only 8-10% is carbon additives although it represents most of the surface and may govern the EEI on positive electrodes. To avoid any effects from carbon additives or binders on the EEI layer, in this study EEI layer is examined on 100% active materials.[74-77]

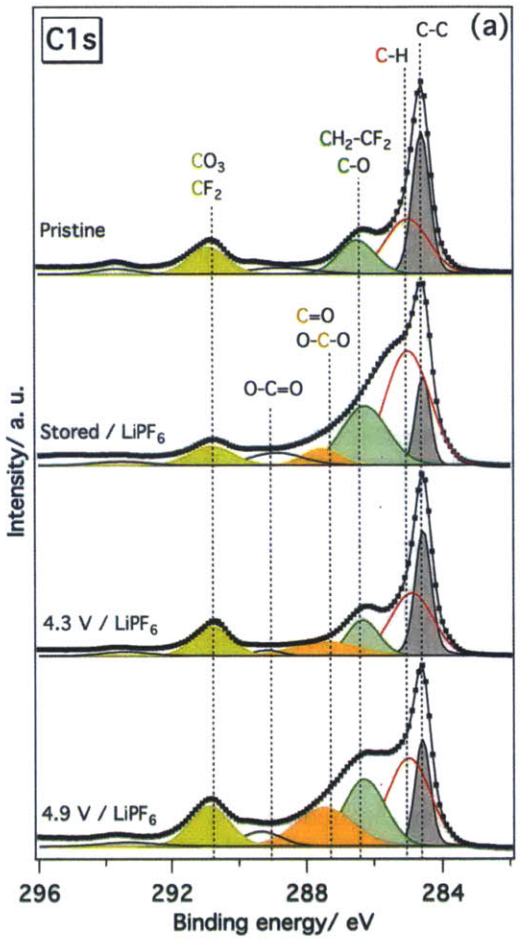

Figure 18. XPS spectra of the C1s photoemission lines of pristine, stored in the electrolyte and charged/discharged carbon black electrodes using $LiPF_6$ in EC:DEC electrolyte. Photon energy of 430 eV is used for these measurements. [77]

Figure 18 shows carbon black electrodes in $LiPF_6$ EC: DEC. Similar species such as ether C-O carboxylate and carbonates found for carbon and also composite positive electrodes at high voltages. Furthermore, PVDF in the composite electrodes makes challenging to study salt and solvent decomposition.[77]

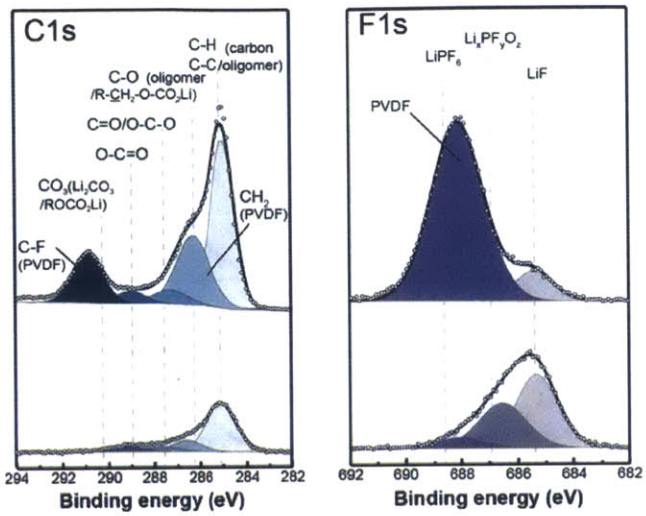

Figure 19. XPS spectra of the C1s and F1s spectra for a $LiCoO_2$ composite electrode (top) and a carbon-free, binder-free $LiCoO_2$ electrode (bottom) at $4.4V_{Li}$. The difference between these XPS spectra shows the importance of using model electrodes to understand EEI layer on positive electrodes.

C1s spectra for composite demonstrate two peaks for PVDF binder which can be seen in Figure 19. These two peaks are around 286.3 and 290.9 eV, which assigned to CH_2 and CF_2 bonds respectively. CF_2 bond overlaps with carbonate at C1s peak. This misleads the reading of the C1s by attributing to Li_2CO_3 on the surface of the positive electrodes. Similarly, for F1s spectra, PVDF peak overlaps with $LiPF_6$ salt peak, but with carbon-free, binder-free electrodes, formation of $Li_xPF_yO_z$ can be seen clearly from these XPS spectra.[78-80]

Three approaches are used to have 100% active materials (Figure 20). First one is the powder deposited on aluminum discs. These carbon-free, binder-free electrodes were prepared by mixing active materials with N-methyl-2-pyrrolidone (NMP) in a 1:100 mass ratio. After it is sonicated for 5 min, the ink was deposited on ½ inch diameter aluminum discs and dried at 100 °C. Afterward, they were pressed under 8T and they were put in a

vacuumed and dried at 120°C overnight. These electrodes were mostly used in XPS measurements.

Second model electrodes were pellets. 300 mg of active electrode is pressed under 8T and sintered at 900 °C. Subsequently, they were also dried and vacuumed overnight. These electrodes were mostly used in XAS/XES measurements.

Figure 20. Model electrodes with 100% active material: Powder on aluminum discs (for XPS measurements), pellets (for XAS/XES measurements) and thin films, respectively. Courtesy of Magali Gauthier.

For thin films, Pulsed Laser Deposition technique is used to get thin films of these active materials. Pulsed Laser Deposition is a method that uses high-power pulsed laser. This laser is focused inside the chamber and it targets the substrate to be deposit the active material. These electrodes will be mostly used in XPS measurements and future in-situ measurements.

3.2 Synthesis of Lithium Transition Metal Oxides

The synthesis of lithium transition metal oxides is mostly done by solid-state synthesis except for $LiNi_{1/3}Mn_{1/3}Co_{1/3}O_2$ (coprecipitation method). The solid-state method (Figure 21) is done by mixing the starting materials in a stoichiometric ratio and by grinding them at least thirty minutes in order to have a homogeneous mixture of these starting

materials. Afterwards, pellets were done from these mixtures and these pellets are heated to high temperatures.

Figure 21. Schematic of solid-state synthesis for lithium transition metal oxides. This method has been used for most synthesis of lithium transition metal oxides rather than $LiNi_{1/3}Mn_{1/3}Co_{1/3}O_2$. For solid-state synthesis, the starting materials are mixed in a stoichiometric ratio and grinded at least thirty minutes to get a homogeneous mixture. A pellet is done from this homogeneous mixture and annealed to high temperatures. Courtesy of Magali Gauthier and Thomas Carney.

$LiCoO_2$ was prepared from solid-state reaction of Li_2CO_3 (Alfa Aesar Puratronic) and Co_3O_4 in a stoichiometric ratio with intermediate grinding. They were annealed at 600 °C for 12h and 900 °C for 24h in air. Heating and cooling rates were at 2 °C min^{-1}. $Co(NO_3)_2*6H_2O$ (Alfa Aesar) is used to maintain the Co_3O_4 precursor . It was synthesized by heating $Co(NO_3)_2*6H_2O$ (Alfa Aesar) at respectively 70, 120 and 450 °C for 3, 3, and 12h. The XRD profile is shown in Figure 22.

$LiNi_{1/3}Mn_{1/3}Co_{1/3}O_2$ was synthesized from LiOH. H_2O (Alfa Aesar) and a hydroxide of nickel, manganese and cobalt by using coprecipitation method. They were mixed in a stoichiometric ratio and they were heated in air at 480 °C for 3h and 900 °C for 3h. The synthesis of these compounds has been checked by XRD, which is shown in Figure 23.

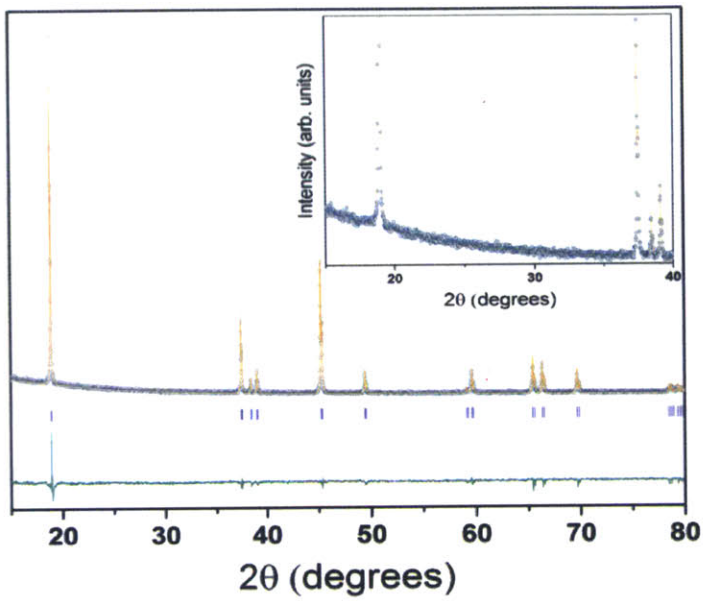

Figure 22. XRD profiles of as-synthesized powders of $LiCoO_2$. The XRD conditions are follows: Bragg Brentano, Fixed Slit (1/4°) AS Slit: (1/2°), Mask: 10 mm Ni filter, Soller Slit: 0.04 RAD, Powder packed in well, Time per step: 75 seconds, Step Size: 0.02. Courtesy of Magali Gauthier and Thomas Carney.

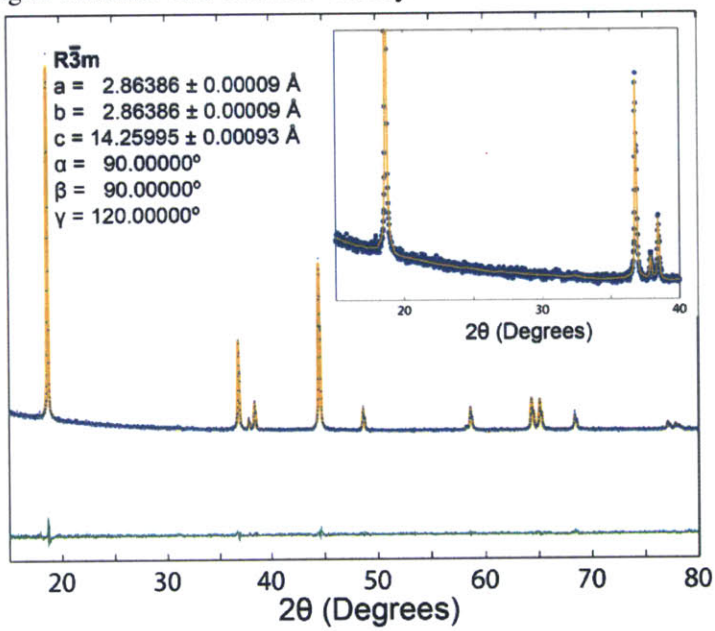

Figure 23. XRD profiles of as-synthesized powders of $LiNi_{1/3}Mn_{1/3}Co_{1/3}O_2$. The XRD conditions are follows: Bragg Brentano, Fixed Slit (1/4°) AS Slit: (1/2°), Mask: 10 mm Ni filter, Soller Slit: 0.04 RAD, Powder packed in well, Time per step: 75 seconds, Step Size: 0.02. Courtesy of Magali Gauthier and Thomas Carney.

Li_2MO_3 particles (M = Ru, Ir and Mn), were synthesized by mixing RuO_2, IrO_2 or $MnCO_3$ with Li_2CO_3 in stoichiometric amount with 10% excess of Li_2CO_3 to compensate for lithium evaporation at high temperature. The powders were mixed and ground together for 30 min and pressed into pellets. Pellets were annealed in air at 800 °C for 6h, 900 °C for 12h, and finally at 1100 °C for 12h with intermediate grinding, using heating and cooling rates of 2 °C/min. After synthesis, part of the powder was ball milled with one-millimeter diameter zirconia balls using planetary ball milling (Pulverisette 6, Fritsch Inc.) at 500 rpm for 12 hours reversing every 30 minutes intermitted by 15 minutes cooling pauses. The XRD profiles of $Li_2Ru_{0.5}Mn_{0.5}O_3$ and Li_2RuO_3 can be see in Figures 24 and 25.

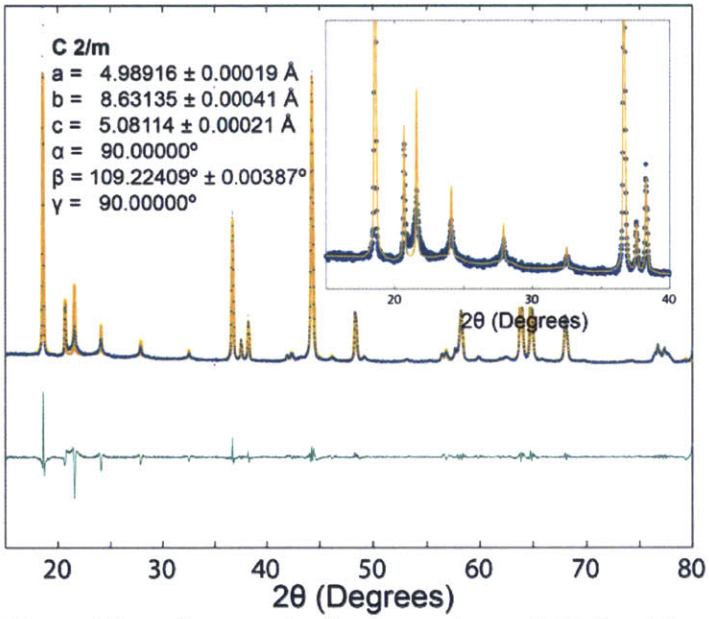

Figure 24. XRD profiles of as-synthesized powders of $Li_2Ru_{0.5}Mn_{0.5}O_3$. The XRD conditions are follows: Bragg Brentano, Fixed Slit (1/4°) AS Slit: (1/2°), Mask: 10 mm Ni filter, Soller Slit: 0.04 RAD, Powder packed in well, Time per step: 75 seconds, Step Size: 0.02. Courtesy of Magali Gauthier and Thomas Carney.

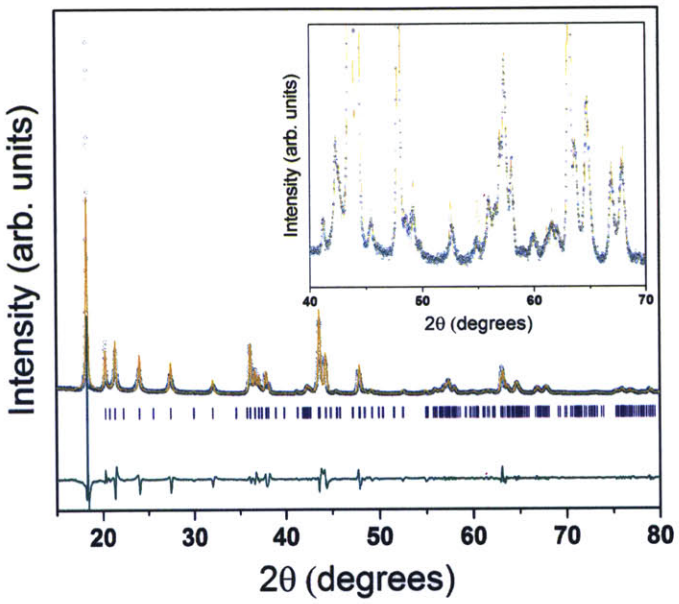

Figure 25. XRD profiles of as-synthesized powders of Li_2RuO_3. The XRD conditions are follows: Bragg Brentano, Fixed Slit (1/4°) AS Slit: (1/2°), Mask: 10 mm Ni filter, Soller Slit: 0.04 RAD, Powder packed in well, Time per step: 75 seconds, Step Size: 0.02. Courtesy of Magali Gauthier and Thomas Carney.

3.3 X-Ray Photoelectron Spectroscopy

X-Ray Photoelectron Spectroscopy uses an effect called photoelectric effect. When certain materials exposed to light, they eject electrons, but they eject electrons only when light's frequency is above a certain threshold frequency (Figure 26). After this threshold frequency, electrons are ejected from the material. If above than threshold frequency light is exposed to the material, the energy of the electrons increases as well.[81]

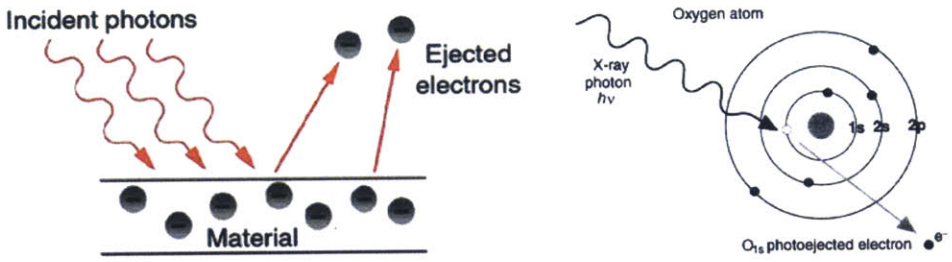

Figure 26. The photoelectric effect is used at X-Ray Photoelectron Spectroscopy. The photoelectron effect is phenomenon of emission of electrons when light shines upon material.[81]

This spectroscopy technique sends X-rays to the material and that ejects the electrons from different core level. For instance, if you remove an electron from O1s level, then your spectra is O1s spectra. After X-rays are sent to the material by an energy hv, the electrons will be ejected from their core levels. The energy hv should be equal to the summation of the binding energy of the electrons, the work function of the material and the kinetic energy of the ejected electron (Figure 27). In terms of equation, this relation becomes:

$$h\nu = BE + KE + \emptyset$$

where hv is the energy of the X-ray photon, BE is the binding energy of the electron, KE is the kinetic energy of the electron and $\emptyset$ is the work function of the material.[82]

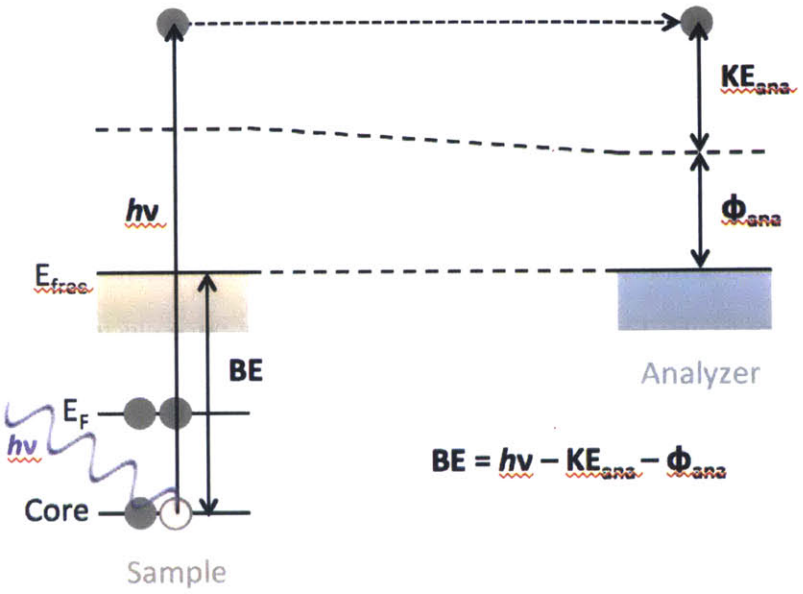

Figure 27. Schematic of X-Ray Photoelectron Spectroscopy: The binding energy of the electron is equal to the energy of the photon minus kinetic energy of the ejected electron and work function of the material. Courtesy of Kelsey Stoerzinger, Marcel Risch, Wesley Hong [82]

With X-Ray photoelectron spectroscopy, we want to see the formation of layer by electrolyte decomposition. There are some advantages by using this product. The biggest advantage is the depth of the profile is around 5-10 nm, so it means that by using XPS, EEI can be seen. Also, it gives information on chemical bonds and it can probe all the elements. Some of the drawbacks are there is no direct information on the exact chemistry of the products, although there is a piece of knowledge on different bonds and from that, different products can be deduced.

Powders on aluminum disc are used for these XPS measurements. These electrodes were cycled in 1M $LiPF_6$ in EC: EMC 3:7 with C/100 rate. Since there is no carbon or binder in these electrodes, we wanted to make sure there is enough time for Li^+ and electron diffusion, because of this a low rate for these charging. After charging galvanostatically with C/100 rate, the potential is held for 5 hours. After charging, the cells were

disassembled in the glovebox and electrodes were rinsed with 50 μL of EMC twice (this corresponds to approximately 15 drops). These electrodes were dried in vacuum at room temperature in the antechamber for 3 hours. Transfer vessel is used for XPS chamber without exposure to air. To ensure reproducibility, at least three electrodes were cycled and measured at XPS.

3.4 X-Ray Absorption and Emission Spectroscopy

X-Ray Absorption Spectroscopy sends an X-Ray photon to the material to excite the electron from core level to conduction band (Figure 29). Since different core level electrons can be excited, different names were given for different core-level excitation. For instance, if 1s electrons are excited, this is called K-edge and for 2s it is L1. Figure 28 illustrates different edges for different core levels.[83]

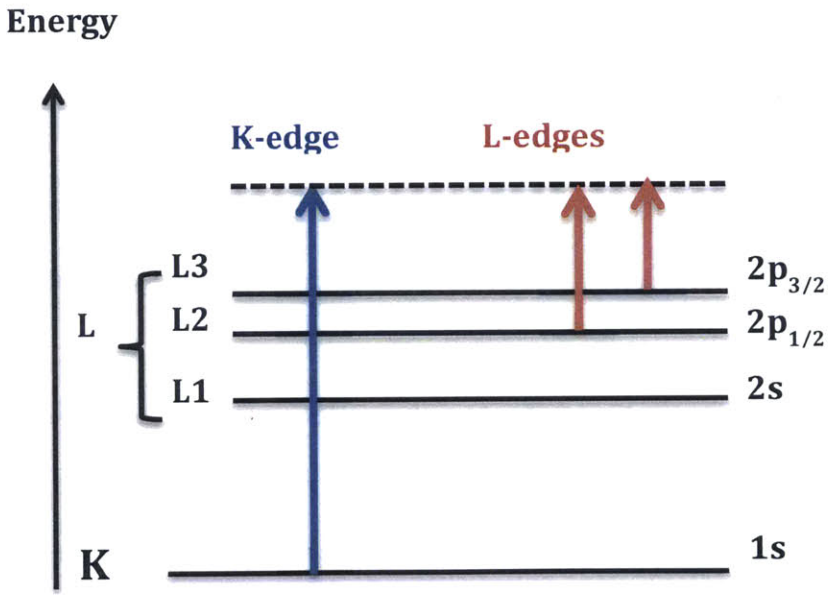

Figure 28. Different edge descriptions for X-Ray Absorption Spectroscopy. These edges were defined by the different core-level excitation, since different core levels can be excited to do XAS measurements. Courtesy of Kelsey Stoerzinger, Marcel Risch, Wesley Hong.

X-Ray Emission Spectroscopy, valence electrons fills the core hole and energy is emitted from the material (Figure 29). In order to get valence electrons, firstly electrons are excited by sending X-Ray photons just like XAS and then, these valence electrons returns back to their core hole.[84]

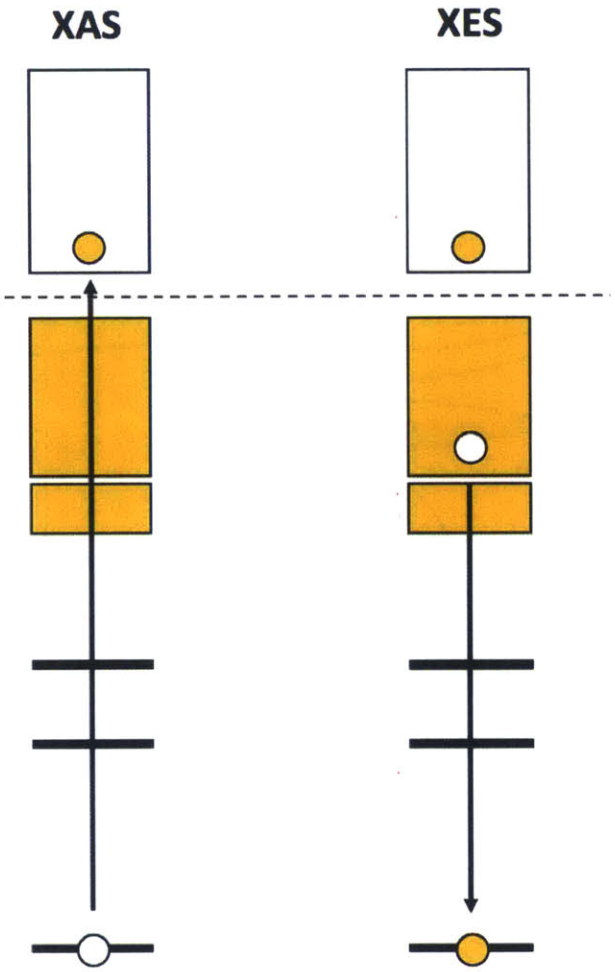

Figure 29. Working Principles of X-Ray Absorption Spectroscopy and X-Ray Emission Spectroscopy: X-Ray Absorption Spectroscopy sends an X-Ray photon to the material to excite the electron from core level to conduction band. X-Ray Emission Spectroscopy, valence electrons fills the core hole and energy is emitted from the material. Courtesy of Kelsey Stoerzinger, Marcel Risch, Wesley Hong.

With X-Ray Absorption and Emission Spectroscopy, we want to see the electronic structure of the positive electrodes. From the discussion above, it is clear that XAS and XES are complimentary of each other. By using both XAS and XES, the whole electronic structure can be learned.

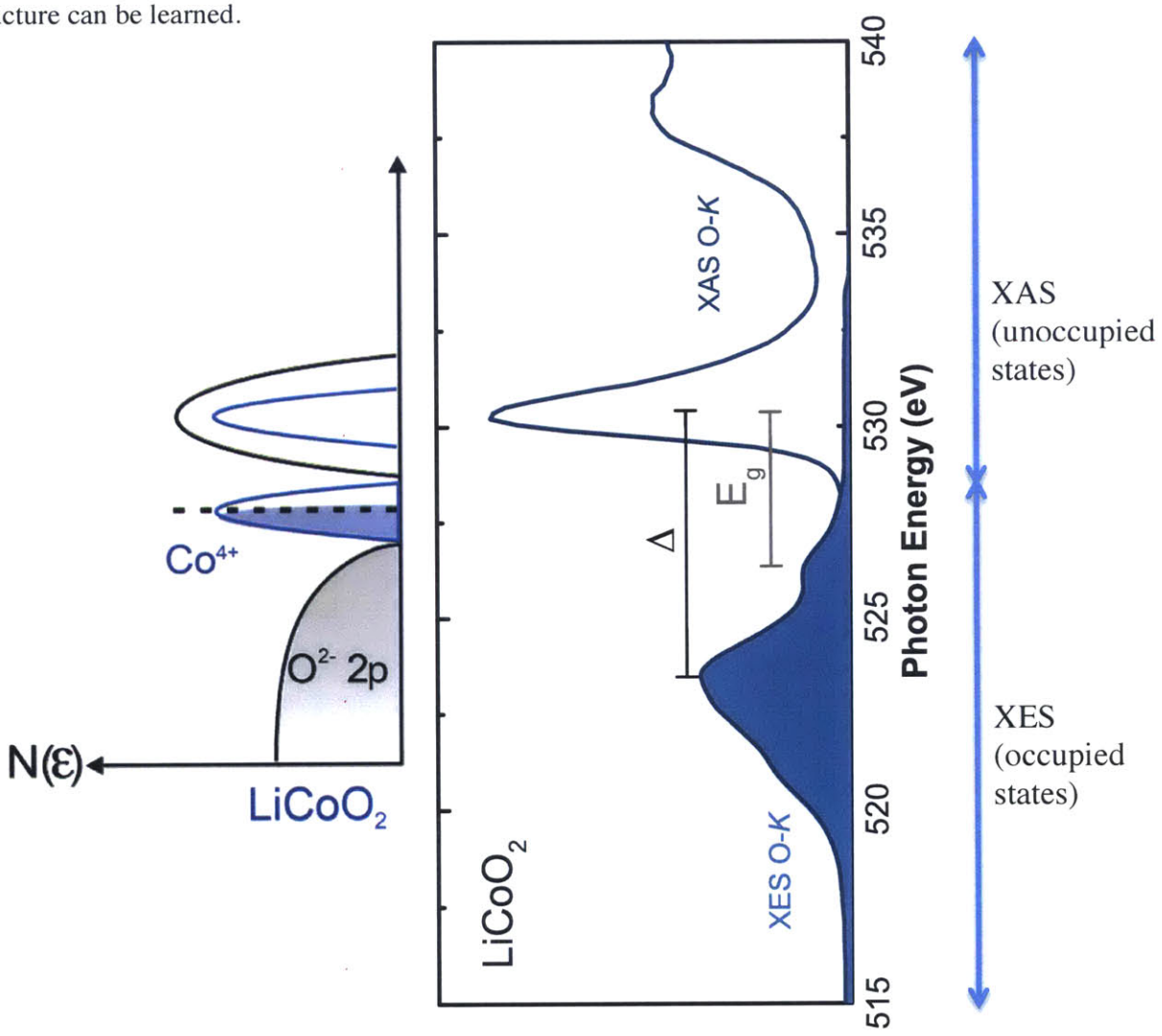

Figure 30. Schematic of proposed electronic structure of the pristine $LiCoO_2$ and the XAS/XES measurements that are collected at ALS. XAS and XES give information about unoccupied and occupied states of the electronic structure. These measurements are done with Magali Gauthier and Wesley Hong.

XAS gives us information about unoccupied states of the electronic structure since photons excite the electrons to the valence band that is the unoccupied states of the electronic structures. The occupied states of electronic structure can be learned from XES measurements where the valence electrons are emitted to core level (Figure 30). With these measurements, the idea is to find electronic structures of different positive electrodes and to see how these electronic structures changes as different potentials are applied to these electrodes.

Pellets were used for these measurements. These electrodes are cycled in 1 M $LiPF_6$ EC : EMC 3:7 electrolyte and C/100 rate is used for charging. Cells disassembled in the glovebox and they were rinsed 30 minutes in EMC. They were transfer to ALS in aluminum sealed bags and they were not exposed to air. Samples are stored at ALS glovebox and mounted on the holder in the glovebox. They were transferred to the chamber using aluminum bags or transfer kits. Both TEY (surface) and TFY (bulk) were measured at beamline 6 or 8. XES measurements acquired at BL 8. Also XPS measurements are done at MIT.

4 Results and Discussion

4.1 XPS Results

XPS measurements were done to investigate the EEI layers on these different positive electrodes for lithium ion batteries. To avoid any effect on carbon and binder, 100 % active materials are used as our electrodes. These electrodes were charged galvanostatically to different desired potentials in 1M $LiPF_6$ in a 3:7 ethylene carbonate (EC): ethylmethylcarbonate (EMC) at a C/100 rate. Although the C/100 rate is slow, since there were no carbon and binder on positive electrodes, we wanted to allow good diffusion of Li and electrons. After disassembling in the glovebox, electrodes were gently rinsed with EMC and they were transferred with transfer vessel to XPS. Here with these data, we show that different positive electrodes show different reactivity towards the electrolyte.

All data is calibrated with the C-C bond at 285 eV. Analysis area is 200 x 200 μm. Core peaks analyzed using a nonlinear Shirley-type background and fitting method is 70% Gaussian and 30% Lorentzian. For Mn, Co and Ni 2p, for fitting, we should use asymmetric peaks.

4.1.1 $LiCoO_2$ and $LiNi_{1/3}Mn_{1/3}Co_{1/3}O_2$

There are four peaks that can be fitted for C1s spectra. These four peaks are at 285, ~286.3, 287.6 and 288.8 eV. The first peak is adventitious carbon or C-H bond. The second peak is attributed to C-O bonds and third peak is related to C=O/O-C-O bonds. The last peak corresponds to O=C-O (a carbon bound to two oxygen atoms).[76-77] As it is

seen from Figure 31, there is no carbonate peak (CO_3:around 290 eV) in these XPS data.[78-79] This carbonate peak is usually observed on pristine positive electrode materials. O1s spectra have also four peaks. First one is oxygen in the lattice, which is around 529.5 eV. The second peak is attributed to ROLi species (~531 eV).[80-81]The third peak corresponds to 3 different contributions. These are oxygen on the surface, carbonate and O-C=O bonds.[82-83] Last one is the O-C=O which is related to single bond between a carbon and an oxygen as in esters (~533.4 eV).[77]

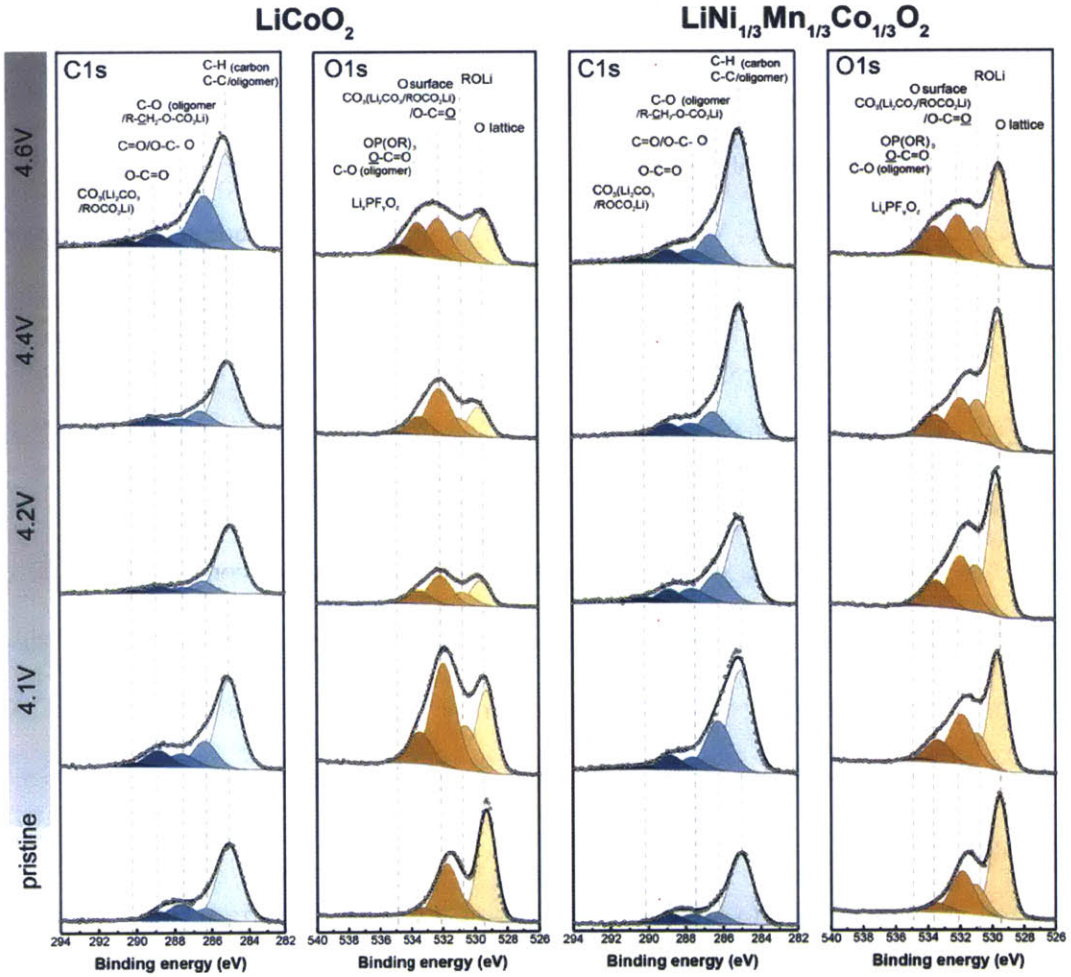

Figure 31. XPS spectra of the C1s and O1s photoemission lines for $LiCoO_2$ and $LiNi_{1/3}Mn_{1/3}Co_{1/3}O_2$ for the pristine carbon-free, binder-free electrodes and after charging to 4.1, 4.2, 4.4 and 4.6 V_{Li}. These measurements are done with Magali Gauthier.

From the first look for these two different positive electrode materials, we can see that EEI layers on $LiCoO_2$ are strongly dependent on the potential. However, that is not the case for $LiNi_{1/3}Mn_{1/3}Co_{1/3}O_2$. Changes for NMC 111 is minimal compared to $LiCoO_2$.

At 4.1 VLi, there is an increase of C-O peaks at C1s spectra (286.3 eV) and O1s spectra (533.4 eV). This increase can be related to the formation of polyethers or semicarbonated $ROCO_2Li$.[84] Also at this voltage, at O1s spectra, a new peak appears around 534.8 eV, which is usually attributed to the formation of lithiated fluorophosphates ($Li_xPF_yO_z$). This formation can be seen at F1s and P2p spectra as well (Figure 32). At this potential, F1s shows the growth of both fluorophosphated and LiF, which are both formed by decomposition of $LiPF_6$ salt.[85]

For $LiCoO_2$, at 4.2 and 4.4 V_{Li}, C1s peaks other than adventitious carbon peak decreased. This also corresponds to the intensity decrease of O1s spectra as well, which means that there is a formation of a surface layer that does not have or small amount of C and O species. At these potentials, F1s spectra show us that there is an increase of LiF[86] and fluorophosphates components, which suggests reactivity with salt.

For $LiNi_{1/3}Mn_{1/3}Co_{1/3}O_2$, LiF and phosphate content are almost constant for different potentials. LiF is considered as a material that is generally formed by chemical reactions. However, the results from these two different materials show that, especially for $LiCoO_2$, LiF formation should be influenced by other factors, not just proton availability due to electrolyte oxidation.

Charging both samples to high voltages such as 4.6 V_{Li}, EEI surface films completely modifies. We can see that from C1s and O1s, since both carbonated and oxygenated

species are increased from 4.4 V_{Li} to 4.6 V_{Li} and LiF content is decreased for $LiCoO_2$. Li1s spectra elucidates that there are no lithiated compounds.

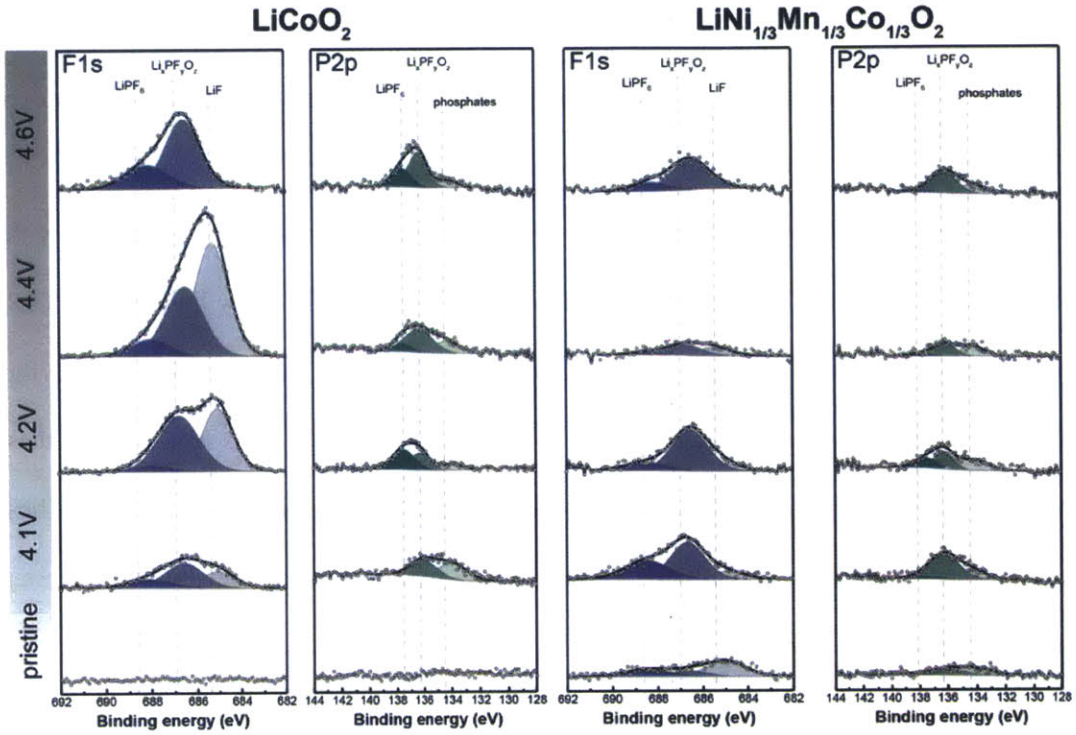

Figure 32. XPS spectra of the F1s and P2p photoemission lines for $LiCoO_2$ and $LiNi_{1/3}Mn_{1/3}Co_{1/3}O_2$ for the carbon-free, binder-free pristine electrodes and after charging to 4.1, 4.2, 4.4 and 4.6 V_{Li}. These measurements are done with Magali Gauthier.

For the disappearance of LiF at 4.4 V_{Li}, we proposed a few different hypotheses. Firstly, LiF domains[87] may be formed and we cannot see these domains from XPS. However, at O1s spectra, the peak for oxygen lattice of the materials (~529.3 eV) can be still seen, which suggests that EEI layer thickness is actually smaller than the penetration depth of XPS (~5-10 nm). Second hypothesis is the breakdown of EEI layer and dissolution of the EEI species. This suggestion is usually proposed on $LiCoO_2$ composite electrodes at high potentials. This may be due to mechanical stress and/or lattice volume change of the

material during delithiation. After this breakdown, new EEI surface layers may be formed at these high voltages.

There is also another aspect that should be considered rather than electrolyte oxidation. When these positive electrodes are charged to high voltages, molecular oxygen or peroxo-like species can be formed. In this case, an investigation at electronic states with respect to the Fermi level is required. For high potentials, Fermi level may fall below the top of the O *2p* band. The removal of lithium ions is compensated by holes in the O *2p* band where lattice O^{2-} are partially oxidized to O^{-}, leading to the formation of O_2^{2-} that finally disproportionate to create O_2 gas.[27-28,72-73] Since NMC 111 has Mn and Ni, these materials may be pushes up the Fermi level, which means less oxygen release. These oxygen species can react with the electrolyte at high potentials and because of this, oxygen species at 4.6 V_{Li} increases as well.

To summarize, if $LiCoO_2$ with $LiNi_{1/3}Mn_{1/3}Co_{1/3}O_2$ are compared, $LiCoO_2$ has more reactivity with the $LiPF_6$ salt to form LiF and phosphates. Up to 4.4 V_{Li}, $LiCoO_2$ EEI film composition is affected by voltage, however, for $LiNi_{1/3}Mn_{1/3}Co_{1/3}O_2$ it seems that the results are very comparable. But for both cases, when the samples charged to 4.6 V_{Li}, there is a strong modification of these EEI layers. Specifically, there is an increase of oxygen based-species, which may be result of the oxidation of the electrolyte.

4.1.2 Li_2RuO_3 and $Li_2Ru_{0.5}Mn_{0.5}O_3$

Similar XPS measurement has been done on Li_2RuO_3 and $Li_2Ru_{0.5}Mn_{0.5}O_3$. As it is explained before Li_2MO_3 compounds, especially Li_2RuO_3 compounds family, there is reversible oxygen anionic redox, which forms peroxo-like species rather than oxygen gas

release. For these compounds, five different voltages were measured: 3.6 V_{Li}, 3.8 V_{Li}, 4.2 V_{Li}, 4.4 V_{Li} and 4.6 V_{Li} and C1s, O1s, F1s, P2p, Mn2p (only for $Li_2Ru_{0.5}Mn_{0.5}O_3$) spectra were collected.

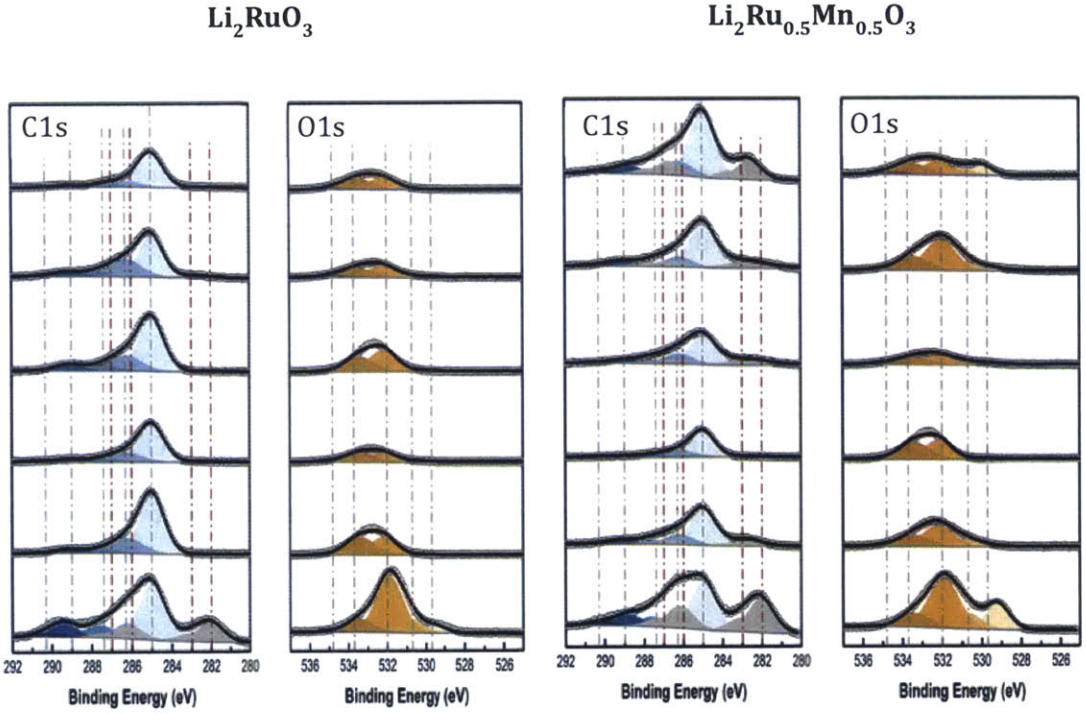

Figure 33. XPS spectra of the C1s and O1s photoemission lines for Li_2RuO_3 and $Li_2Ru_{0.5}Mn_{0.5}O_3$ for the carbon-free, binder-free pristine electrodes and after charging to 3.6, 3.8, 4.2, 4.4 and 4.6 V_{Li}. For C1s spectra, red lines indicate the Ru peaks and gray lines indicate the C species. These measurements are done with Magali Gauthier.

The pristine Li_2RuO_3, C1s spectra indicate both carbonated species and Ru peaks which can be seen in Figure 33. The binding energy of Ru is close to C peaks so Ru peaks should be added to the deconvolution parameters at C1s spectra. There are four Ru peaks that should be considered: Ru $3d_{5/2}$ split peak and its satellite peak; Ru $3d_{3/2}$ split peak and its satellite peak.[27-28] It is hard to see carbon peaks for O-C-O and C-O[84-85], which are around 287.6 eV and 286.3 eV because of the Ru 3d peaks. For O1s spectra, the highest

peak is surface oxygen peak around 532 eV and other than this peak; there is oxygen lattice around 529.8 eV, ROLi peak around 530.3 eV and C-O (oligomer/ O-C=O) peak around 533.8 eV.[86-88]

Once the electrode is charged to 3.6 V_{Li}, Ru peaks disappear from C1s spectra. Also, high binding energy carbon species cannot be seen from at C1s spectra. All these suggest the formation EEI film on this positive electrode. This also can be seen in O1s spectra as well. The intensity of surface oxygen peak (~532 eV) decreases from pristine to 3.6 V_{Li} and ROLi and oxygen lattice disappear from O1s spectra. These behaviors also suggest the surface film formation.

From 3.6 V_{Li} till 4.6 V_{Li}, C1s and O1s spectra seem similar. Two peaks are appearing at C1s spectra, which are C-H peak or adventitious carbon peak and C-O peak. The intensity of these two peaks seems similar. For O1s spectra, there are two peaks developing: Oxygen surface peak (~532 eV) and C-O (oligomer/ O-C=O) peak (~533.8 eV). Their intensities are actually quite low. These imply that there is a surface film on positive electrode and it seems that this film is quite stable at different potentials. Also, this surface film is not formed by carbon or oxygen species because the XPS intensity of these species is quite low.

F1s spectra in Figure 34 indicate that LiF mostly forms this surface film. LiF content is quite higher than $Li_xPF_yO_x$ and $LiPF_6$ and LiF[93] content substantially changes at differential potentials. One possibility for this stable surface film on Li_2RuO_3 is that there is a large amount of LiF, which covers the positive electrode, so that the intensity of C1s and O1s spectra decreases because of this LiF coverage. The intensity of P2p spectra is quite low, so it is safe to assume that there are large amounts of LiF on this surface film.

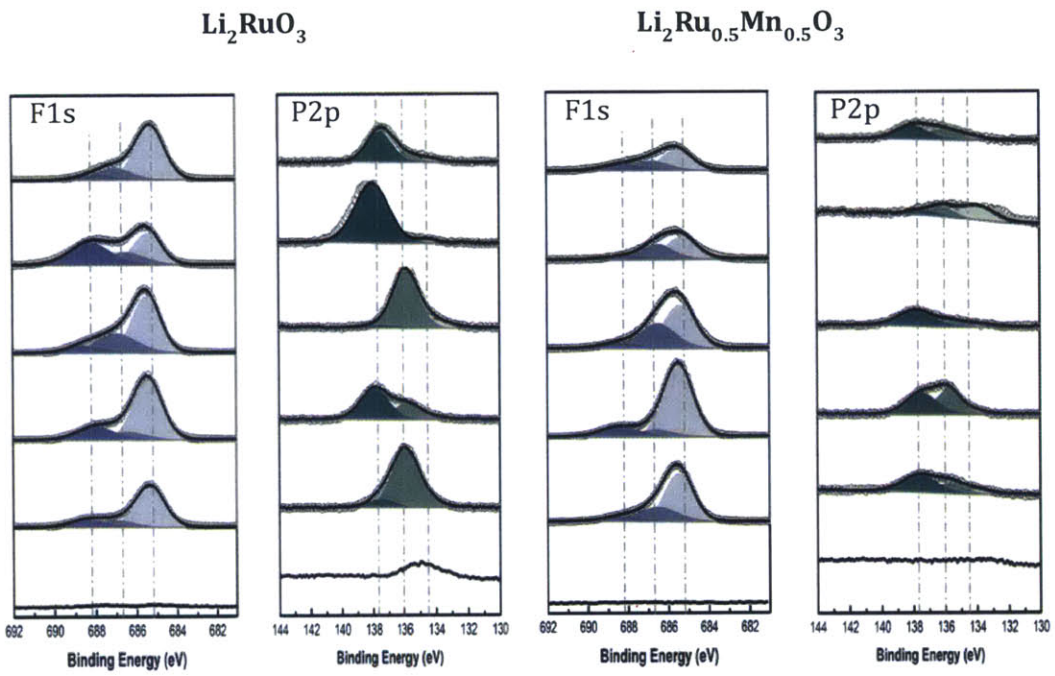

Figure 34. XPS spectra of the F1s and P2p photoemission lines for Li_2RuO_3 and $Li_2Ru_{0.5}Mn_{0.5}O_3$ for the carbon-free, binder-free pristine electrodes and after charging to 3.6, 3.8, 4.2, 4.4 and 4.6 $V_{Li.}$ These measurements are done with Magali Gauthier.

For pristine $Li_2Ru_{0.5}Mn_{0.5}O_3$ material, the four Ru peaks can be seen at C1s spectra that have higher intensity than the intensity of Ru peaks for Li_2RuO_3. Similarly, at O1s spectra, oxygen lattice peak has higher intensity than Li_2RuO_3 oxygen lattice intensity. Similar to Li_2RuO_3, the highest intensity peak at O1s spectra is oxygen surface peak, which is around 532 eV.

When $Li_2Ru_{0.5}Mn_{0.5}O_3$ charged to 3.6 V, the intensity of Ru peaks decreases but it does not vanish like Li_2RuO_3. Similarly, at O1s spectra, oxygen lattice peak disappears, which imply a formation of EEI film. Unlike Li_2RuO_3, there are three peaks at O1s spectra rather than two peaks. Just like Li_2RuO_3, there is peak around 532 eV, which corresponds

to surface oxygen and the intensity of these peaks are decreased. There is another peak at 533.8 eV C-O and oligomers. Additional these two peaks, $Li_2Ru_{0.5}Mn_{0.5}O_3$ has a peak around 530 eV (ROLi peak).

At potentials 3.8 V, there is no Ru peak at C1s and ROLi peak at O1s disappears as well. This may correspond to thicker EEI layer than 3.6 V. The Ru peaks start to appear at 4.2 V and their intensity increases as potential goes from 4.2 V to 4.6 V. At 4.6 V, the oxygen lattice can be seen at O1s spectra. The thickness of the EEI layer decreases from 4.2 V to 4.6 V. Furthermore, these results match with F1s spectra. From 3.6 V to 3.8 V, the amount of LiF increases and at 4.2 V, LiF amount starts to decrease. Once LiF amount decreases, Ru peaks can be seen in C1s spectra.

To summarize, it appears that the amount of LiF in these two compounds dominates the EEI layer. As LiF amount increases, the intensity of C- and O- peaks start to decrease and Ru peaks appear when LiF amount decreases.

4.1.3 Discussion

Aforesaid, for XPS measurements at least two to four samples were done for each potential to check the reproducibility. In this section, first the reproducibility of these samples will be shortly discussed. Then, XPS measurements will be compared with each other, namely comparison between $LiCoO_2$, $LiNi_{1/3}Mn_{1/3}Co_{1/3}O_2$, Li_2RuO_3 and $Li_2Ru_{0.5}Mn_{0.5}O_3$.

All XPS measurements for the carbon-free, binder-free $LiCoO_2$ electrodes are in Appendix A. For 4.1 V_{Li}, two electrodes show similar trend for almost all spectra and first electrode has less $LiPF_6$. The LiF content of these electrodes is quite similar (4% and 6%) and because of this, it does not change the trend in Figure 35. Also first electrode

was cycled in the new glovebox and we found the results more trustable in the new glovebox. For the case of 4.2 V_{Li}, the electrode with $Li_{0.47}CoO_2$ has been chosen since the C1s and O1s are the mean of the others electrodes in terms of intensity. Also, the again if we look at the LiF content of all four samples, the intensity of LiF peaks are quite similar. Another reproducibility check for the carbon-free, binder-free pristine $LiCoO_2$ electrodes that charged to 4.4 V_{Li} has been shown in Appendix A. Here, it can be said that the reproducibility of the XPS measurements are better than the 4.1 and 4.2 V_{Li} cases, especially if we remove the contribution of the salt in some electrodes in the F1s spectra. Also, it should be worth mention that the amount of the amount of LiF is quite well reproducible and the O1s spectra also really reproducible. At 4.6 V_{Li}, the electrodes with $Li_{0.33}CoO_2$ content and $Li_{0.24}CoO_2$ content illustrates the similar kind of trend. Especially if we look at the trends of absence of LiF and presence of a lot of oxygen species, these electrodes are reasonably comparable.

For the carbon-free, binder-free pristine $LiNi_{1/3}Mn_{1/3}Co_{1/3}O_2$ electrodes, eight different spectra have been shown in Appendix B. These spectra display that for 4.1 V_{Li}, the same trends can be seen for electrodes with $Li_{0.53}NMCO_2$, and $Li_{0.51}NMCO_2$ except for the amount of fluorophosphates. However, the intensities of F1s spectra are actually small compared to $LiCoO_2$. So, the actual change between these F1s spectra is actually insignificant. Only two sample were done for 4.2 V_{Li}, 4.4 V_{Li} and 4.6 V_{Li}, since the reproducibility of these samples are quite well and their delithiation content is similar for both samples.

For the case of Li_2RuO_3 (Appendix C), two complications were encountered. For one is the $LiPF_6$ content in F1s is spectra. For some samples such as 3.6 V_{Li}, C1s and O1s

spectra were similar in the contents of carbon and oxygen species however, F1s and P2p showed a large amount of $LiPF_6$. For these cases, the sample with small amount $LiPF_6$ is chosen for further analysis. Second one was the trend of P2p peaks for each potential was usually different. However, the intensities of P2p spectra are actually small compared to $LiMO_2$ materials. Because of this reason, we can say that the XPS data for Li_2RuO_3.
Last XPS measurements were done for $Li_2Ru_{0.5}Mn_{0.5}O_3$, which can be seen in Appendix D. The difficulty with these XPS spectra is the differences between P2p spectra. But similar to Li_2RuO_3, the intensity of P2p peaks are small compared to C1s, F1s and O1s and because of this, the change in P2p spectra is inconsequential.

In this work, XPS measurements were done on two different compound families: $LiMO_2$ and Li_2MO_3. As it is mentioned in previous chapters, they have different electrochemical and oxygen anionic redox behavior. Content of different species can be seen at Figure 35. If we compare $LiCoO_2$ with $LiNi_{1/3}Mn_{1/3}Co_{1/3}O_2$, $LiCoO_2$ has more reactivity with the $LiPF_6$ salt to form LiF and phosphates. Up to 4.4 V_{Li}, $LiCoO_2$ EEI film composition is affected by voltage, however, for $LiNi_{1/3}Mn_{1/3}Co_{1/3}O_2$, it seems that the results are very comparable. But for both cases, when the samples charged to 4.6 V_{Li}, there is a strong modification of these EEI layers. Specifically, there is an increase of oxygen based-species, which may be result of the oxidation of the electrolyte.

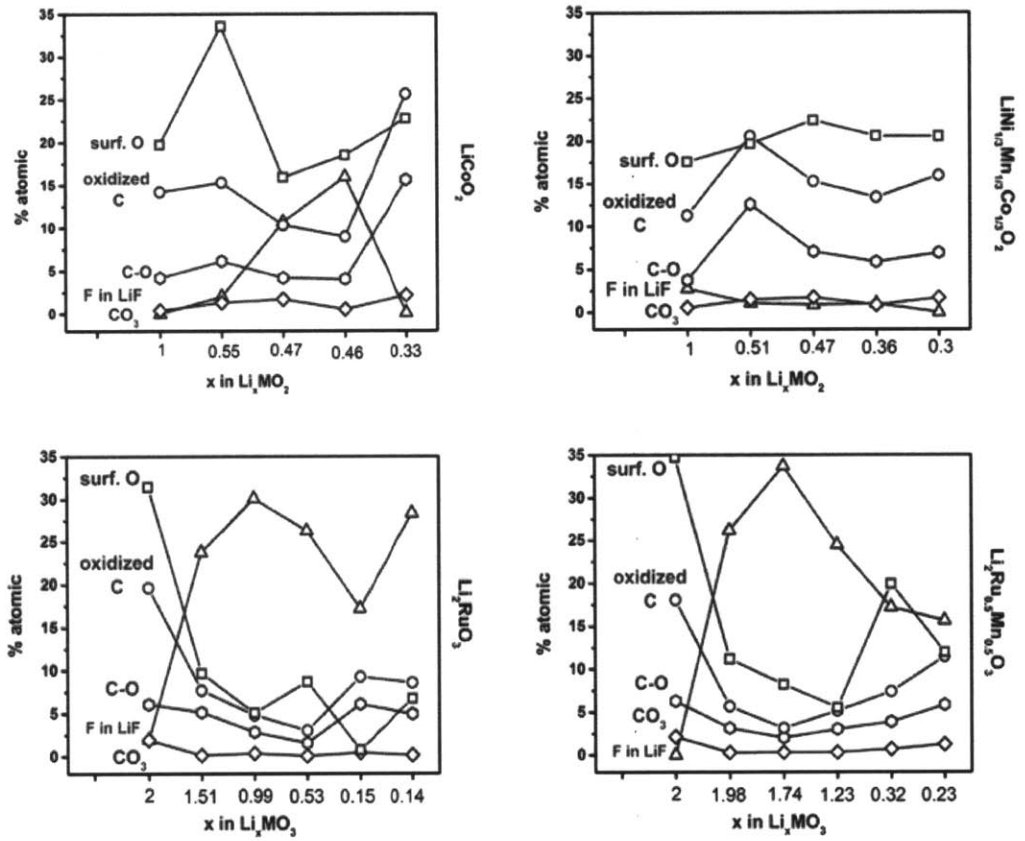

Figure 35. Atomic percentages from XPS spectra of $LiCoO_2$, $LiNi_{1/3}Mn_{1/3}Co_{1/3}O_2$, Li_2RuO_3 and $Li_2Ru_{0.5}Mn_{0.5}O_3$. Pristine and charged carbon-free, binder-free $LiCoO_2$ and $LiNi_{1/3}Mn_{1/3}Co_{1/3}O_2$ electrodes at 4.1 V_{Li}, 4.2 V_{Li}, 4.4 V_{Li} and 4.6 V_{Li}. Pristine and charged carbon-free, binder-free Li_2RuO_3 and $Li_2Ru_{0.5}Mn_{0.5}O_3$ electrodes at 3.6 V_{Li}, 3.8 V_{Li}, 4.2 V_{Li}, 4.4 V_{Li} and 4.6 V_{Li}.

When Li_2RuO_3 and $Li_2Ru_{0.5}Mn_{0.5}O_3$ are compared, they both have high reactivity with the $LiPF_6$ salt to form LiF. They definitely have more LiF content than $LiCoO_2$ and $LiNi_{1/3}Mn_{1/3}Co_{1/3}O_2$, which can be seen at Figure 30. Even the lowest amount of LiF for Li_2RuO_3 and LRMO (18%) is larger than the largest LiF content for $LiCoO_2$ (16%). Both for Li_2RuO_3 and LRMO, the largest LiF amount is at 3.8 V_{Li}. After charging to 4.2 V_{Li}, LiF content decreases, although the decrease of LiF content for LRMO is more severe

than Li_2RuO_3. Because of the large amount of LiF, the amounts of surface oxygen and oxidizes carbon species decrease right after charging to 3.6 V_{Li}.

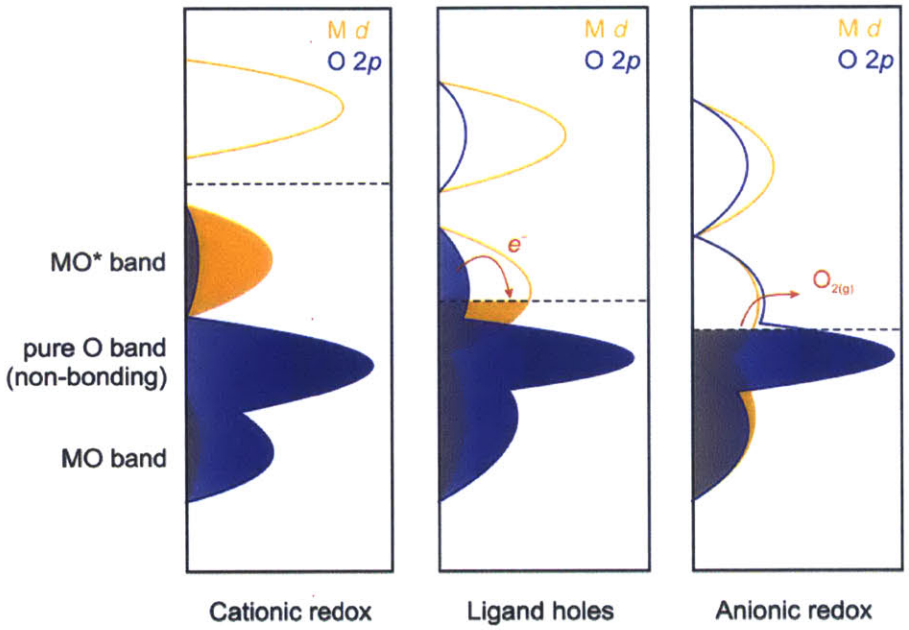

Figure 36. Cationic redox, ligand holes and oxygen anionic redox for lithium transition metal oxides between M d band and oxygen 2p band. The differences between XPS measurements of $LiMO_2$ and Li_2MO_3 can be explained with anionic redox. [95]

These results can be explained with oxygen anionic redox and oxygen and metal d band model (an example of anionic redox in Figure 36). After XPS analysis on different positive electrodes, our hypothesis is when d band electron number increases or when lithium content decreases, M-O covalency for given lithium content increases. This means the enhancement of oxygen redox and increasing decomposition of solvated ions and free electrons. In order to test this hypothesis, the electronic structure of these different positive electrodes should be checked which could be done by XAS/XES measurements.

4.2 XAS/XES Results

As it is explained in the previous chapter 3.3, in order to understand the electronic structure variations by applying different potentials, XAS and XES measurements were done at ALS in Lawrence Berkeley National Laboratory. For XAS measurements both TFY and TEY measurements were done where one of them probes the surface and the other one probes the bulk.

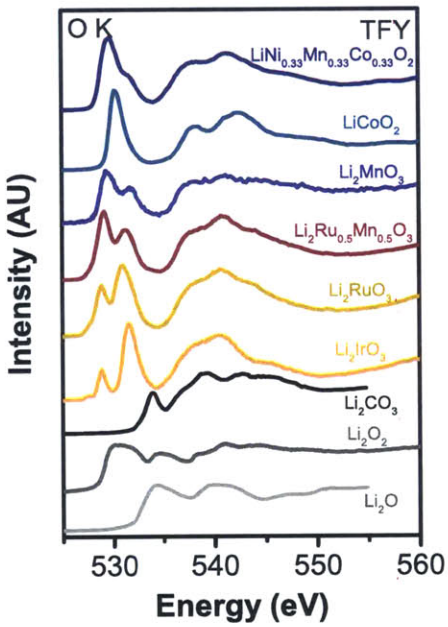

Figure 37. X-Ray Absorption Spectroscopy measurement results for different pristine positive electrode materials with reference materials Li_2CO_3, Li_2O_2 and Li_2O.[96-97] These measurements are done with Magali Gauthier and Wesley Hong.

Figure 37 shows XAS TFY results for different materials with reference materials Li_2CO_3, Li_2O_2 and Li_2O. Even looking at these pristine materials, the results can give us some insight into the differences between Li_2MO_3 and $LiMO_2$. When $LiMO_2$ is compared with Li_2MO_3, there is only one peak appearing for $LiMO_2$; however there are two peaks around 530 eV for Li_2MO_3. So the key question is why there are two peaks for Li_2MO_3

and only one peak $LiMO_2$. One answer could be the different interactions of O lattice with these M transition metals and lithium. Also if the data is compared with the reference materials, it can be seen that none of the peaks seem to match with Li_2O.

This difference between $LiMO_2$ and Li_2MO_3 can be explained with two hypotheses. First one is the exchange splitting in oxides. This was previously explained by de Groot et al., where these exchange effects split the t_2g and e_g into four and these are spin-up t_{2g}, spin down t_{2g}, spin up e_g and spin down e_g which can be seen in Figure 38.[98]

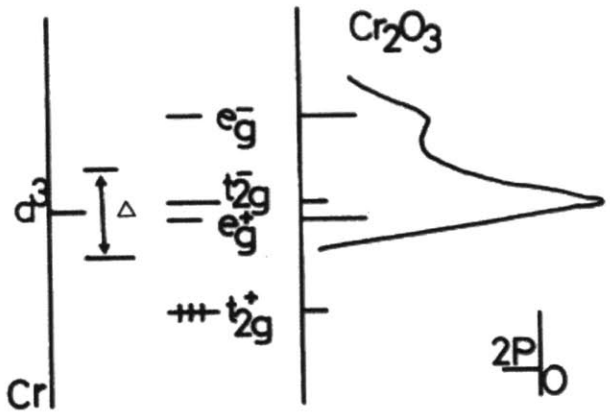

Figure 38. The exchange effect for two group bands t_{2g} and e_g which splits these bands into four: spin-up t_{2g}, spin down t_{2g}, spin up e_g and spin down e_g. This exchange splitting is proposed for oxides. [98]

Second hypothesis is the t_{2g} and e_g might be split for Li_2MO_3 compounds. The difference between Co^{3+} and Ru^{4+} tried to explained below:

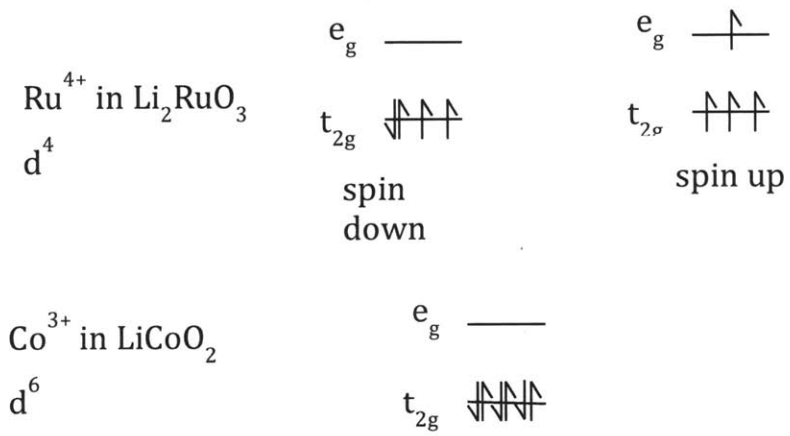

Tsai et al. mentioned this t_{2g} and e_g splitting in their work on RuO_2 and IrO_2 which can be seen in Figure 39:

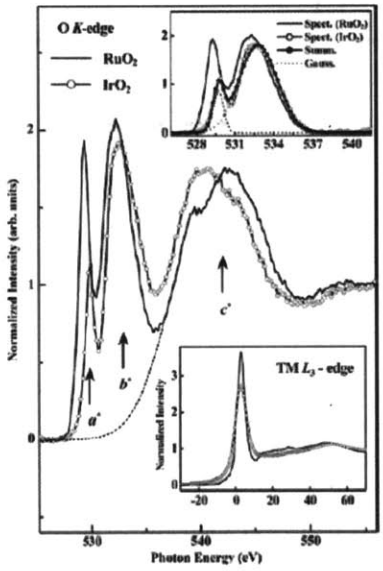

Figure 39. O K-edge XAS spectra for RuO_2 and IrO_2 nanorods, which shows t_{2g} and e_g splitting. Lower graph exhibits Ru and Ir L3 edge and upper graph shows the background corrected XANES spectra. [99]

The other option for these two peaks might be the Ru-Ru dimers in Li_2RuO_3 compounds, where first peak of the XAS spectrum might be due to the antibonding of Ru-Ru dimers. Nevertheless, this does not explain two peaks for Li_2IrO_3 spectra since Ir-Ir dimers are not observed for Li_2IrO_3.[100]

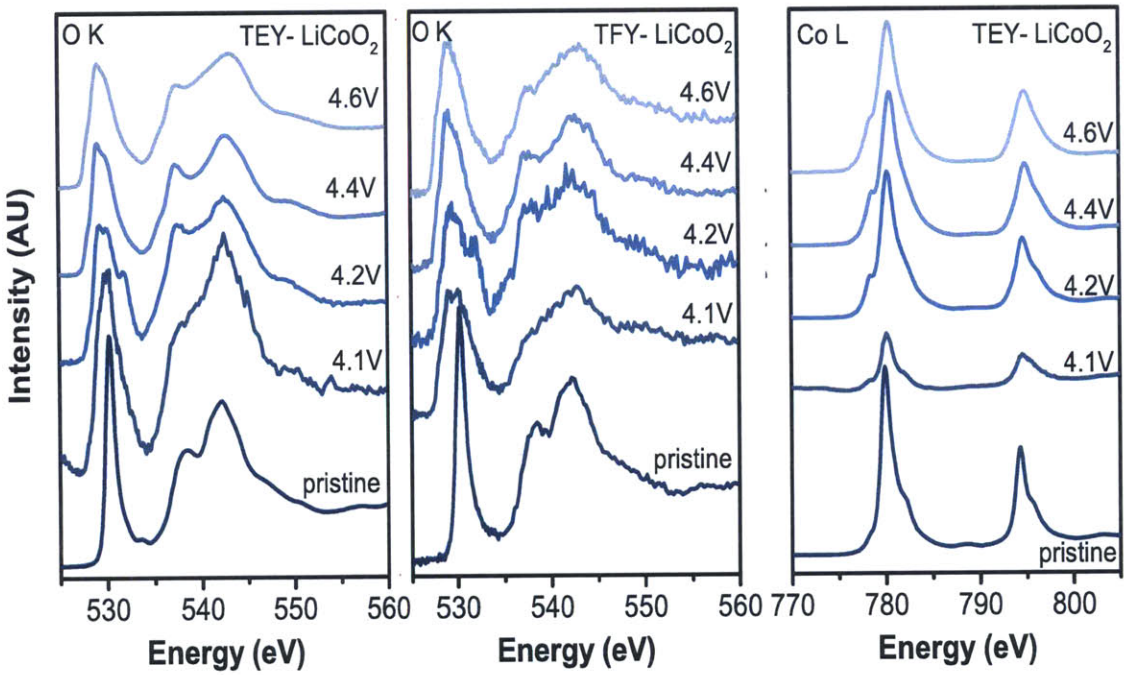

Figure 40. O K-edge (TEY and TFY) and Co L-edge XAS spectra for pristine and charged $LiCoO_2$ and electrodes at 4.1 V_{Li}, 4.2 V_{Li}, 4.4 V_{Li} and 4.6 V_{Li}. These measurements are done with Magali Gauthier and Wesley Hong.

Here is an example of charged samples of $LiCoO_2$ for both TFY and TEY measurements (Figure 40). As it is seen, as the sample is charged to higher potentials, the peaks start to broaden and peaks tend to shift to lower energies. Ensling et al.[101] have already seen this behavior where they see the change in the Co3d-O2p hybridizes states by these shifts and broadening of peaks. Co L spectra are not influenced upon charging. There is an increase of the low energy shoulder upon charge and shift of the main peak to the higher energy.

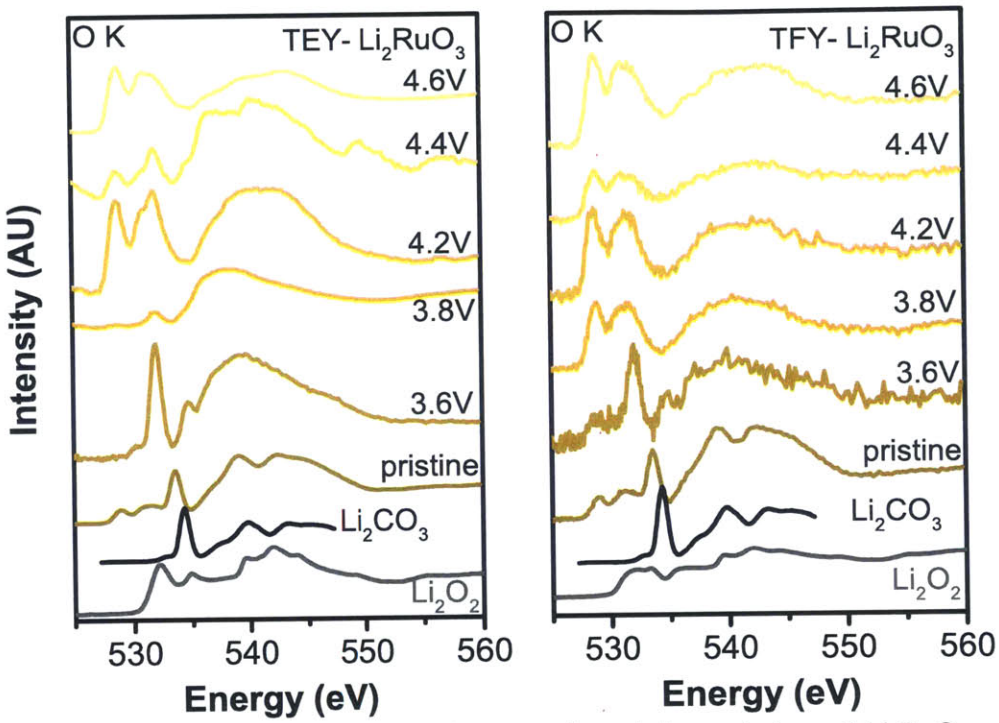

Figure 41. O K-edge (TEY and TFY) XAS spectra for pristine and charged Li_2RuO_3 and electrodes at 3.6 V_{Li}, 3.8 V_{Li}, 4.2 V_{Li}, 4.4 V_{Li} and 4.6 V_{Li}. These measurements are done with Magali Gauthier and Wesley Hong.

Another example for charged positive electrodes is shown in Figure 41. Here different Li_2RuO_3 positive electrodes are charged to five different potentials and we have observed some changes. Firstly, there is an increase of the t_{2g} peak intensity up to 3.8 V and t_{2g} and e_g peaks shifts in energy. Secondly, there is an increase of the first peak from 3.8 V to 4.6 V. Maybe this might suggest the oxidation of oxygen anion.

We tried to combine information from XAS, XES and XPS to further analyze the data. For these analyzes 2nd and 1st derivatives used to determine the features positions and errors of the XES spectra and XES and XPS aligned with the lowest feature. The difference between the XAS pre-edge and the antibonding feature in XES determine the band gap. The charge transfer is established by either the difference between XAS pre-

edge and non-bonding or XAS and Fermi level (For Li_2MO_3, to account for the metallic nature of these oxides). All samples aligned to the absolute energy scale relative to $LiCoO_2$ (work function 5eV). For these further analyzes, we started with pristine materials for different materials and we also collected XPS measurements for all the samples that we measured for XAS/XES.

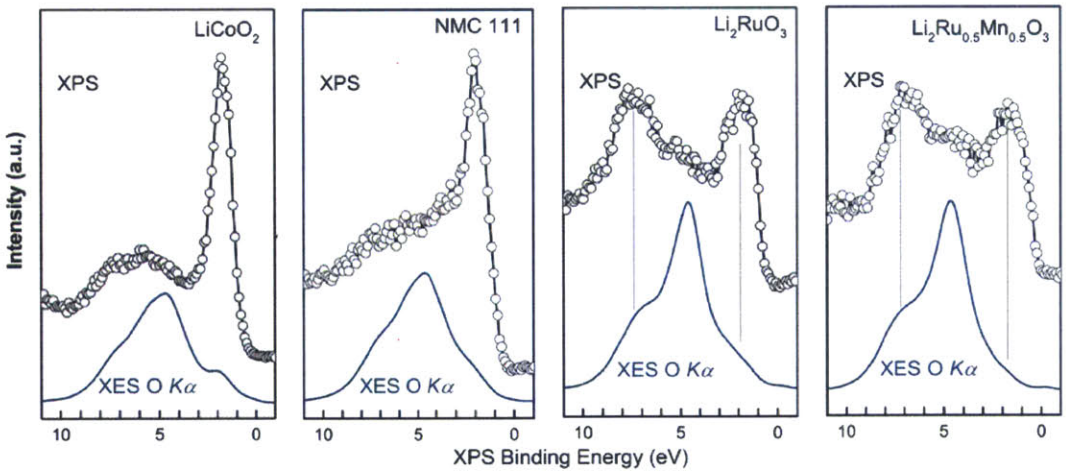

Figure 42. Alignment of XES spectra with XPS spectra for $LiCoO_2$, NMC 111, Li_2RuO_3 and $Li_2Ru_{0.5}Mn_{0.5}O_3$. Hybridization features should be used for these alignments. It aligns the lowest energy XPS valence band with lowest energy peak of the superposition.[102] These analyses are done with Magali Gauthier and Wesley Hong.

The alignment of XES spectra with XPS valence band measurements uses the hybridization features. It takes the superposition and then aligns the lowest energy peak of the superposition with the lowest energy XPS valence band feature. This gives us a strong method to obtain partial density of states. It should be mentioned that this kind of alignment relies on an assumed relation between the XES and XPS valence band energy scales. From the results of Figure 42, we can say that, Li_2MO_3 XPS valence bands are dominated by the TM (high cross-section of Ru, Ir).[102]

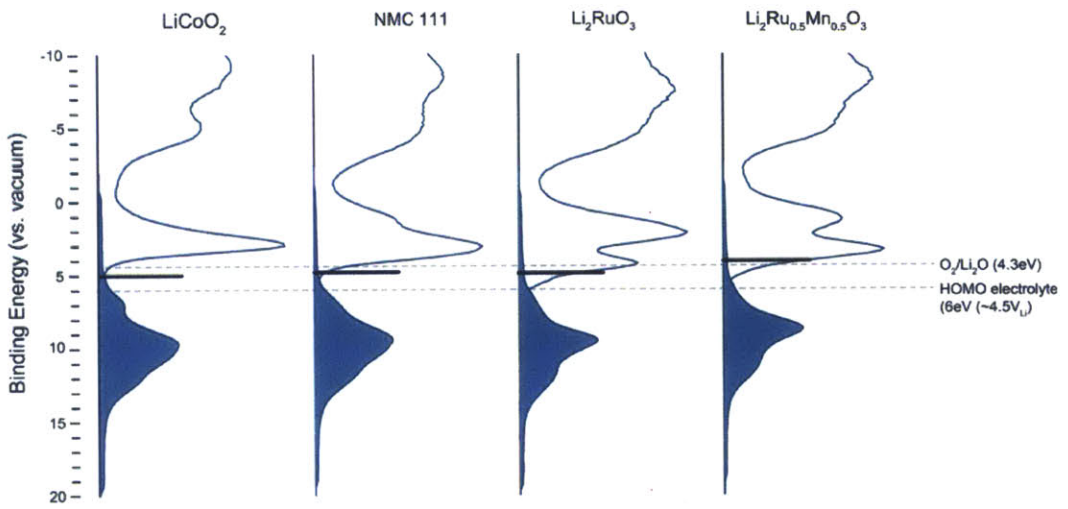

Figure 43. Experimentally determined band positions: Gray lines indicate HOMO of the electrolyte and redox level of O_2/Li_2O.[102] These analyses are done with Magali Gauthier and Wesley Hong.

There is still a need for further analysis with these XAS/XES data (see example in Figure 43). From these data, we believe that we can completely understand the electronic structure of the different positive electrode materials. This understanding may lead to the understanding of different oxygen anionic redox behavior for Li_2MO_3 and $LiMO_2$ and these behaviors' effects to the formation of different EEI layers.

5 Conclusions and Suggestions for Future Work

5.1 Conclusion

By using model electrodes, we showed the importance of using 100% active material while studying EEI layer on oxides positive electrodes. With this method, we avoid any misinterpretation from the presence of additives, since even the smallest amount of these additives has large surface area. We highlighted the different reactivity of $LiCoO_2$, $LiNi_{1/3}Mn_{1/3}Co_{1/3}O_2$, Li_2RuO_3 and $Li_2Ru_{0.5}Mn_{0.5}O_3$ where $LiNi_{1/3}Mn_{1/3}Co_{1/3}O_2$ is the least affected by the end-of-charge potential. At high cut-off potentials, different positive electrode materials display a rearrangement of the EEI layers that may be correlated with the poor performance of these materials at high potentials. Besides, XPS results illustrate different reactivity with $LiPF_6$ at different potentials suggest that may be the formation of LiF does not just happen by chemical reaction.

XAS/XES spectra measurements have been obtained on different cathode materials. These measurements provide information about partial density of state of the positive electrodes during charging. Even XAS/XES spectra of the various pristine materials show important differences in their electronic structure. One of the critical analyses couples these measurements with valence bands measured by XPS to align them on an absolute energy scale. At the end of this analysis, the electronic structure will be correlated with the formation of species such as O_2 or peroxo-like species and their possible influence on the electrode/electrolyte interface.

5.2 Suggestions for Future Work

Our work showed the importance of using different spectroscopy techniques to understand EEI layer better and we believe that it revealed certain aspects of EEI layer for different cathode materials. However, there is still need for more systematic study for these EEI layers.

Firstly, we showed the importance of using 100% active materials rather than composite electrodes. Because of this reason, different thin films can be prepared to study EEI layers. With thin films, different orientations of these positive electrodes can be studied by XPS to see each orientation's effect on the EEI layers.

Secondly, all of the work that has been done are ex-situ studies, meaning that the electrodes were charged, stopped, the positive electrodes were removed from the cell and the measurements were done. In order to have a better understanding of EEI layer, in situ studies should be done. For these studies, firstly in situ cells should be designed for different measurements, specifically in situ Raman cell and in situ FTIR cell. After having these cells, we can perform in situ measurement with Raman and FTIR on different carbon-free, binder-free electrodes such as $LiCoO_2$, NMC, Li_2RuO_3. Raman and FTIR will give information on chemical species on EEI layer and EQCM will provide information on the mass changes on the surface of the electrode. After all these measurements, we can develop design principles for interface/surface chemistry and structure between electrolytes and positive electrodes.

APPENDIX A: Reproducibility check for $LiCoO_2$ at 4.1V_{Li}, 4.2 V_{Li}, 4.4 V_{Li} and 4.6 V_{Li}

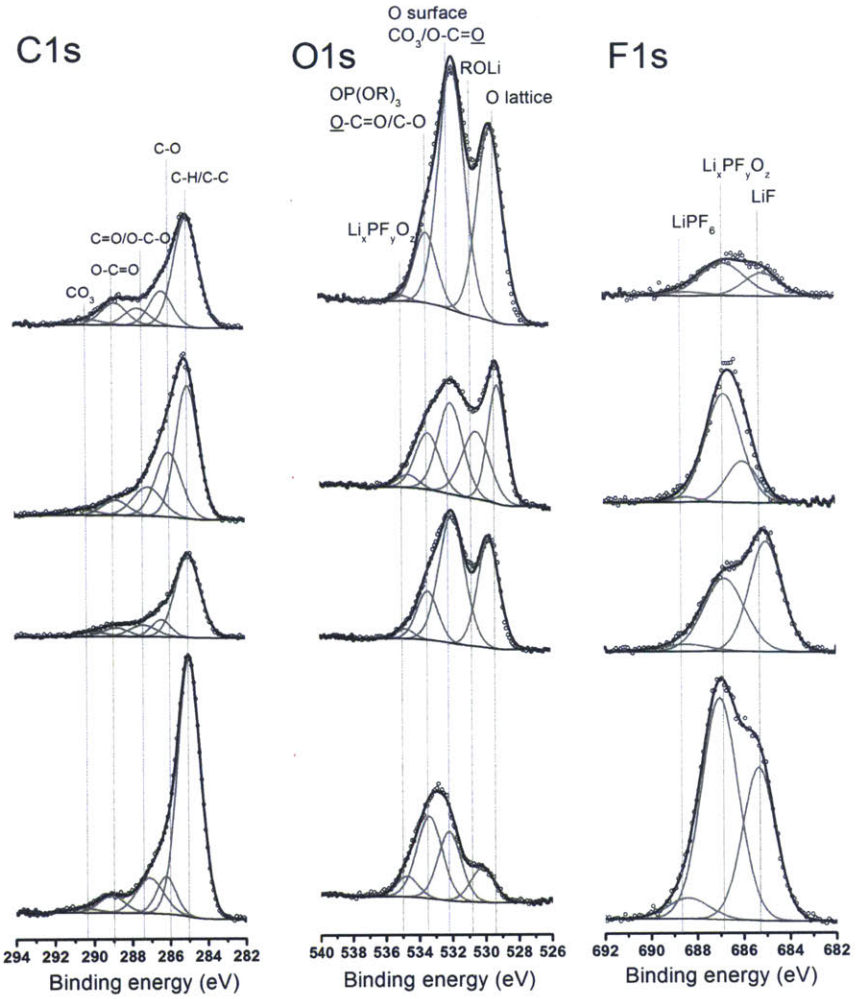

XPS spectra of the C1s, O1s and F1s photoemission lines for the carbon-free, binder-free pristine $LiCoO_2$ electrodes and after charging to 4.1 V_{Li}. The delithiation amounts of these samples are $Li_{0.58}CoO_2$, $Li_{0.56}CoO_2$, $Li_{0.55}CoO_2$, $Li_{0.55}CoO_2$, respectively. For analysis sample with $Li_{0.55}CoO_2$ content has been chosen for further analysis.

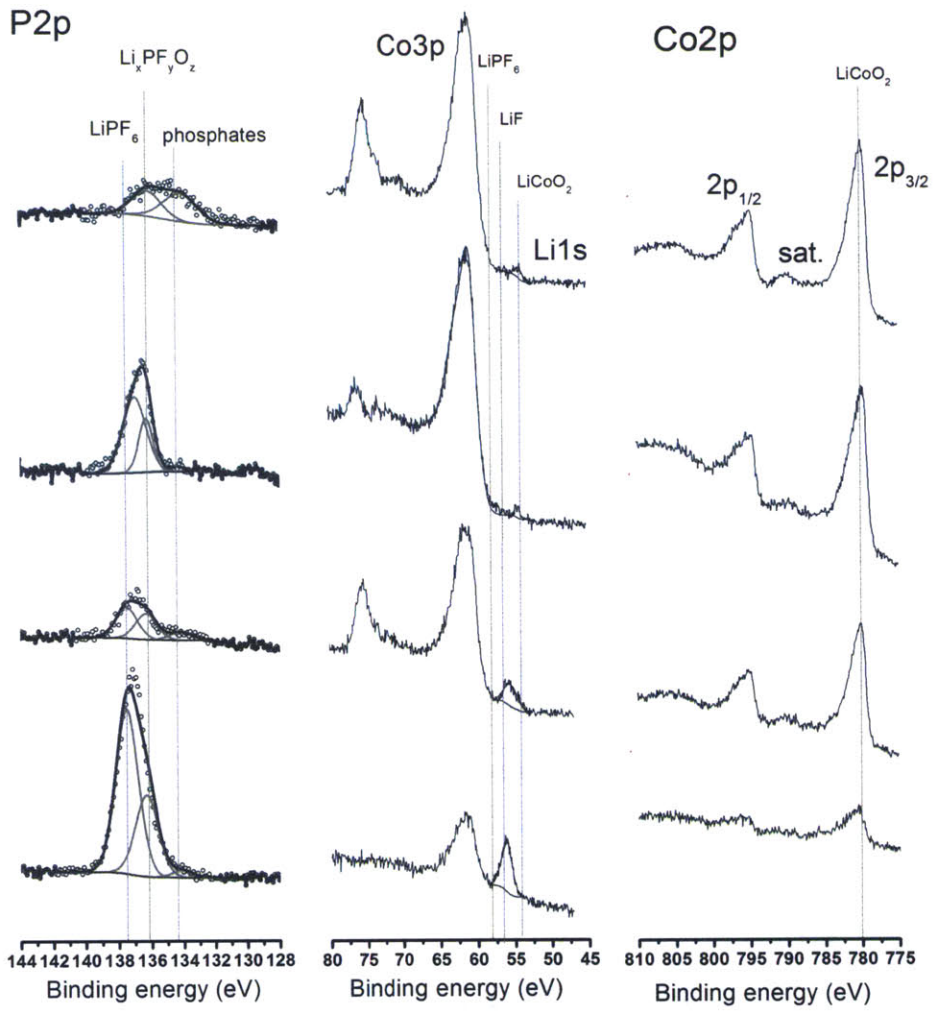

XPS spectra of the P2p, Co3p and Co2p photoemission lines for the carbon-free, binder-free pristine $LiCoO_2$ electrodes and after charging to 4.1 V_{Li}. The delithiation amounts of these samples are $Li_{0.58}CoO_2$, $Li_{0.56}CoO_2$, $Li_{0.55}CoO_2$, $Li_{0.55}CoO_2$, respectively. For analysis sample with $Li_{0.55}CoO_2$ content has been chosen for further analysis.

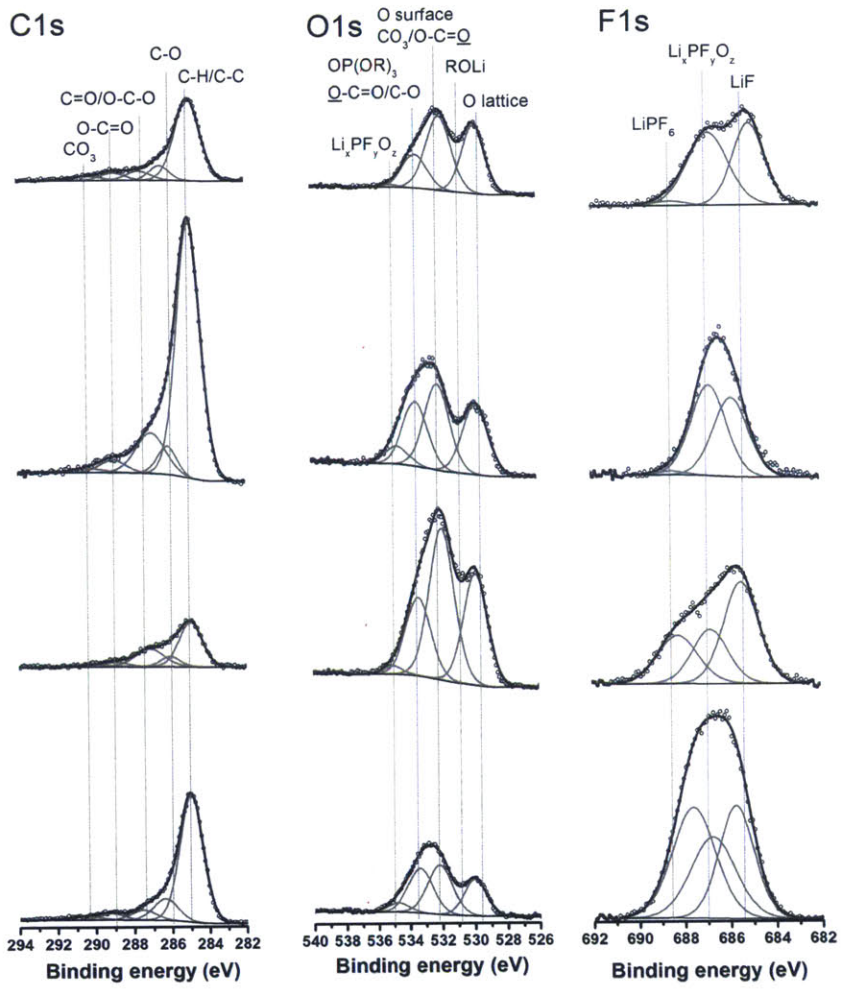

XPS spectra of the C1s, O1s and F1s photoemission lines for the carbon-free, binder-free pristine $LiCoO_2$ electrodes and after charging to 4.2 V_{Li}. The delithiation amounts of these samples are $Li_{0.59}CoO_2$, $Li_{0.55}CoO_2$, $Li_{0.36}CoO_2$, $Li_{0.47}CoO_2$, respectively. For analysis sample with $Li_{0.47}CoO_2$ content has been chosen for further analysis.

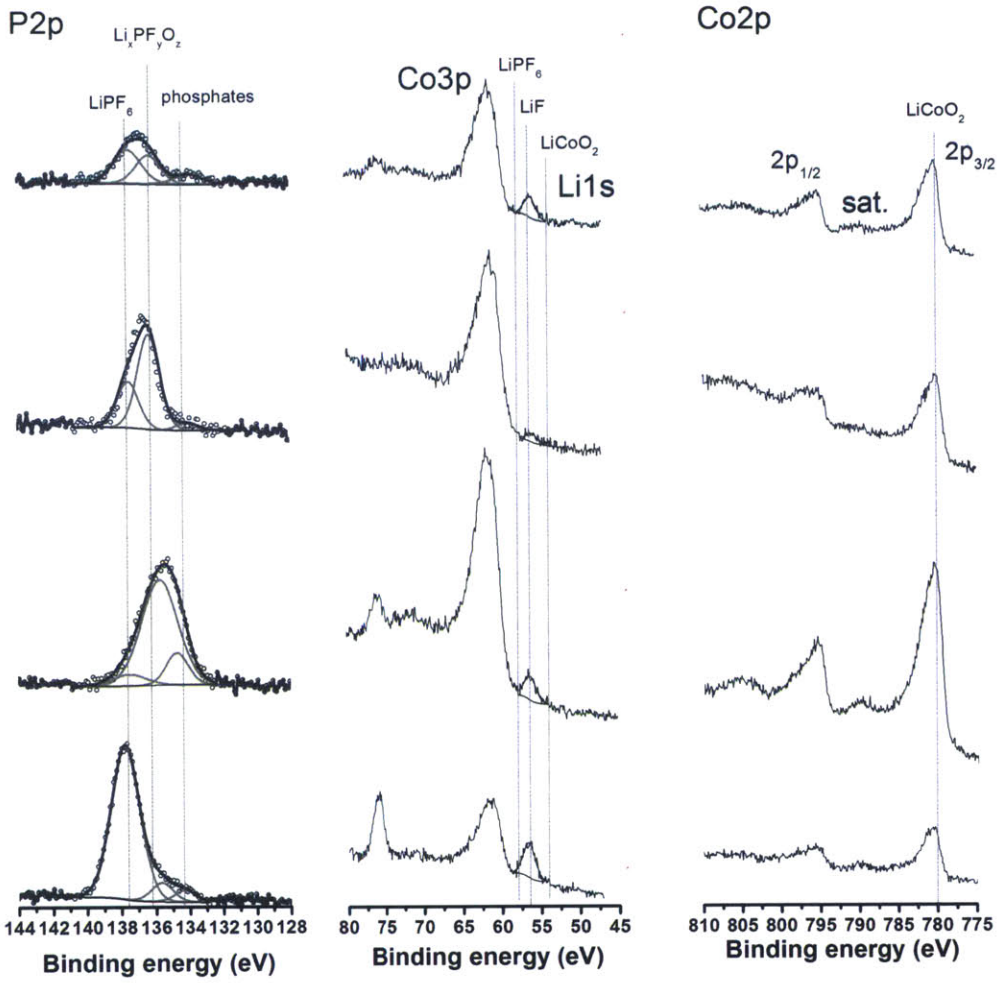

XPS spectra of the P2p, Co2p and Co3p photoemission lines for the carbon-free, binder-free pristine $LiCoO_2$ electrodes and after charging to 4.2 V_{Li}. The delithiation amounts of these samples are $Li_{0.59}CoO_2$, $Li_{0.55}CoO_2$, $Li_{0.36}CoO_2$, $Li_{0.47}CoO_2$, respectively (from down to up). For analysis sample with $Li_{0.47}CoO_2$ content has been chosen for further analysis.

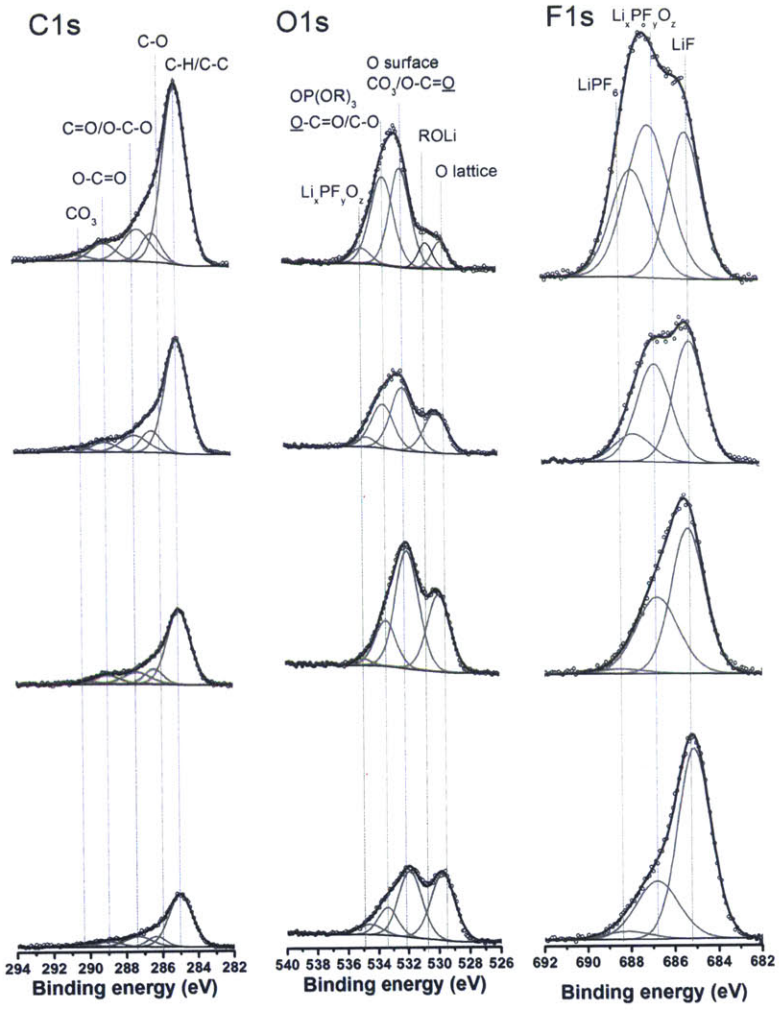

XPS spectra of the C1s, O1s and F1s photoemission lines for the carbon-free, binder-free pristine $LiCoO_2$ electrodes and after charging to 4.4 V_{Li}. The delithiation amounts of these samples are $Li_{0.37}CoO_2$, $Li_{0.46}CoO_2$, $Li_{0.39}CoO_2$, $Li_{0.42}CoO_2$, respectively. For analysis sample with $Li_{0.46}CoO_2$ content has been chosen for further analysis.

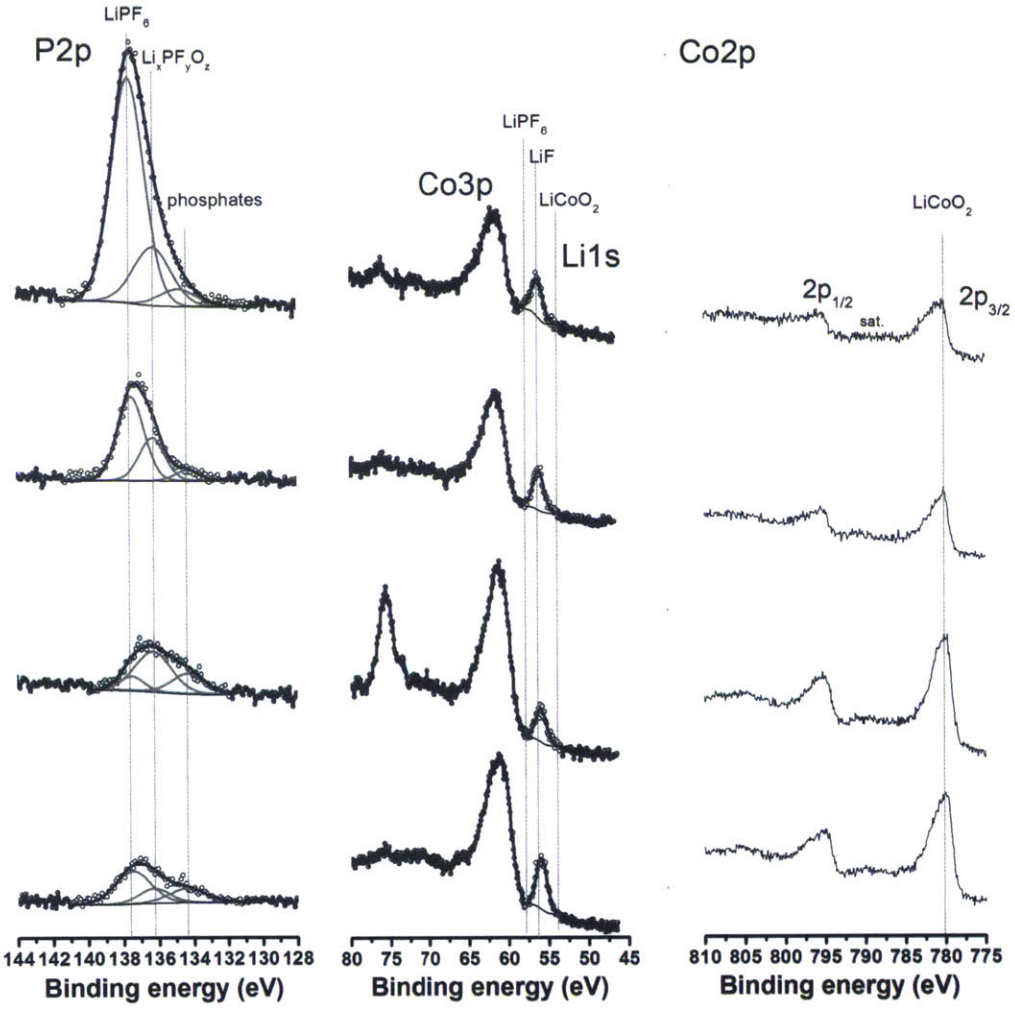

XPS spectra of the P2p, Co2p and Co3p photoemission lines for the carbon-free, binder-free pristine $LiCoO_2$ electrodes and after charging to 4.4 V_{Li}. The delithiation amounts of these samples are $Li_{0.37}CoO_2$, $Li_{0.46}CoO_2$, $Li_{0.39}CoO_2$, $Li_{0.42}CoO_2$, respectively. For analysis sample with $Li_{0.46}CoO_2$ content has been chosen for further analysis.

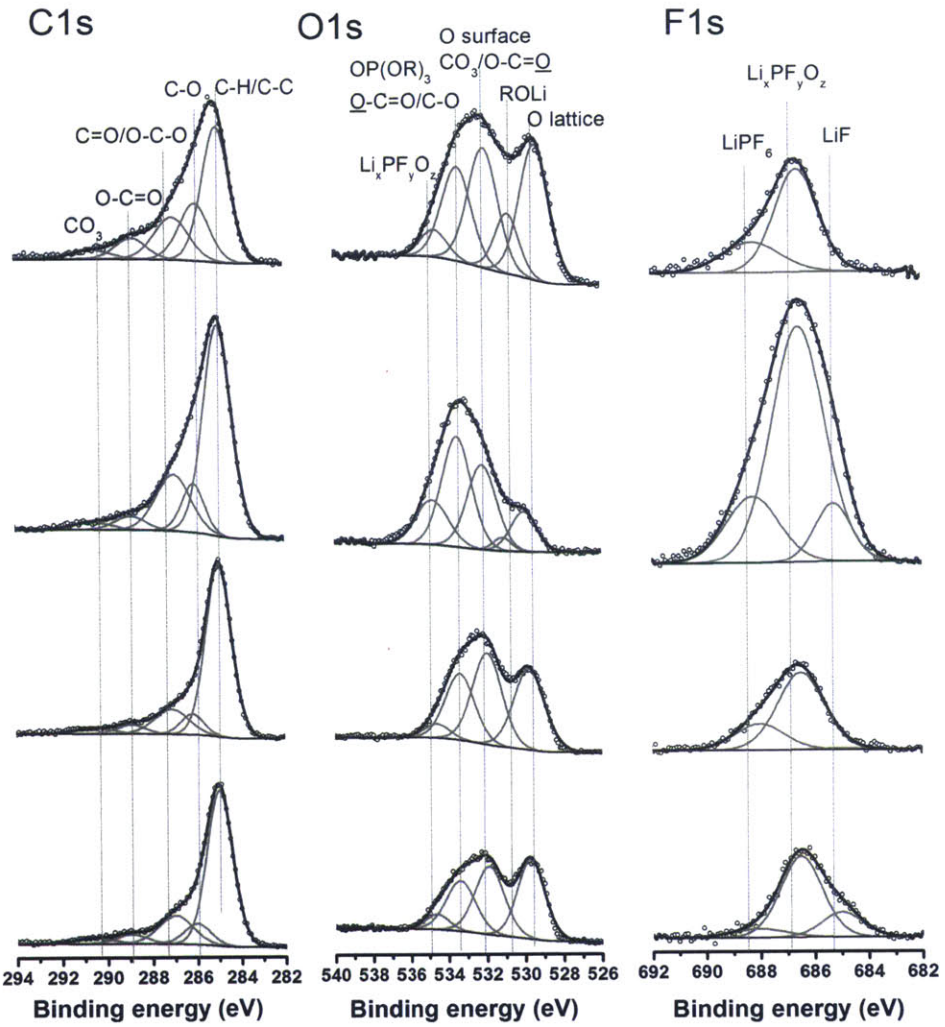

XPS spectra of the C1s, O1s and F1s photoemission lines for the carbon-free, binder-free pristine $LiCoO_2$ electrodes and after charging to 4.6 V_{Li}. The delithiation amounts of these samples are $Li_{0.19}CoO_2$, $Li_{0.24}CoO_2$, $Li_{0.08}CoO_2$, $Li_{0.33}CoO_2$, respectively. For analysis sample with $Li_{0.33}CoO_2$ content has been chosen for further analysis.

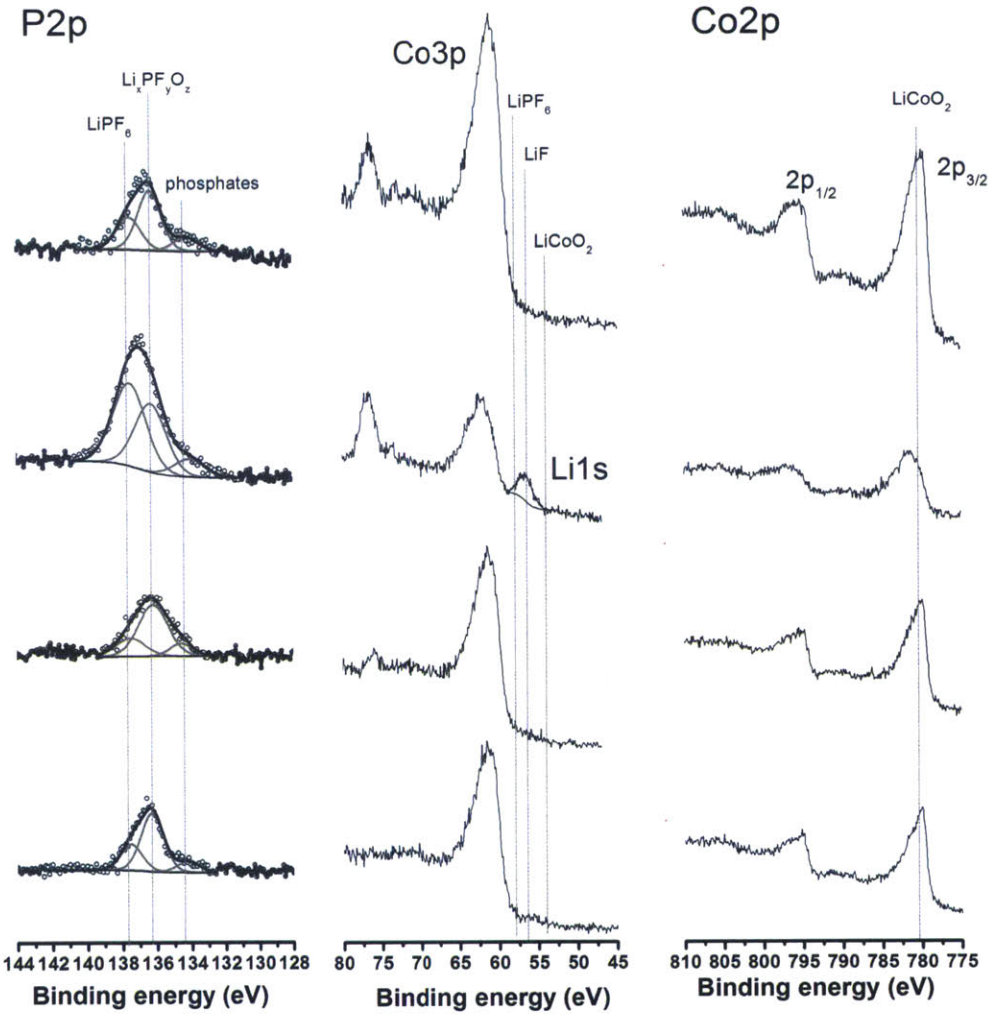

XPS spectra of the P2p, Co2p and Co3p photoemission lines for the carbon-free, binder-free pristine $LiCoO_2$ electrodes and after charging to 4.6 V_{Li}. The delithiation amounts of these samples are $Li_{0.19}CoO_2$, $Li_{0.24}CoO_2$, $Li_{0.08}CoO_2$, $Li_{0.33}CoO_2$, respectively. For analysis sample with $Li_{0.33}CoO_2$ content has been chosen for further analysis.

APPENDIX B: Reproducibility check for $LiNi_{1/3}Mn_{1/3}Co_{1/3}O_2$ at 4.1V_{Li}, 4.2 V_{Li}, 4.4 V_{Li} and 4.6 V_{Li}

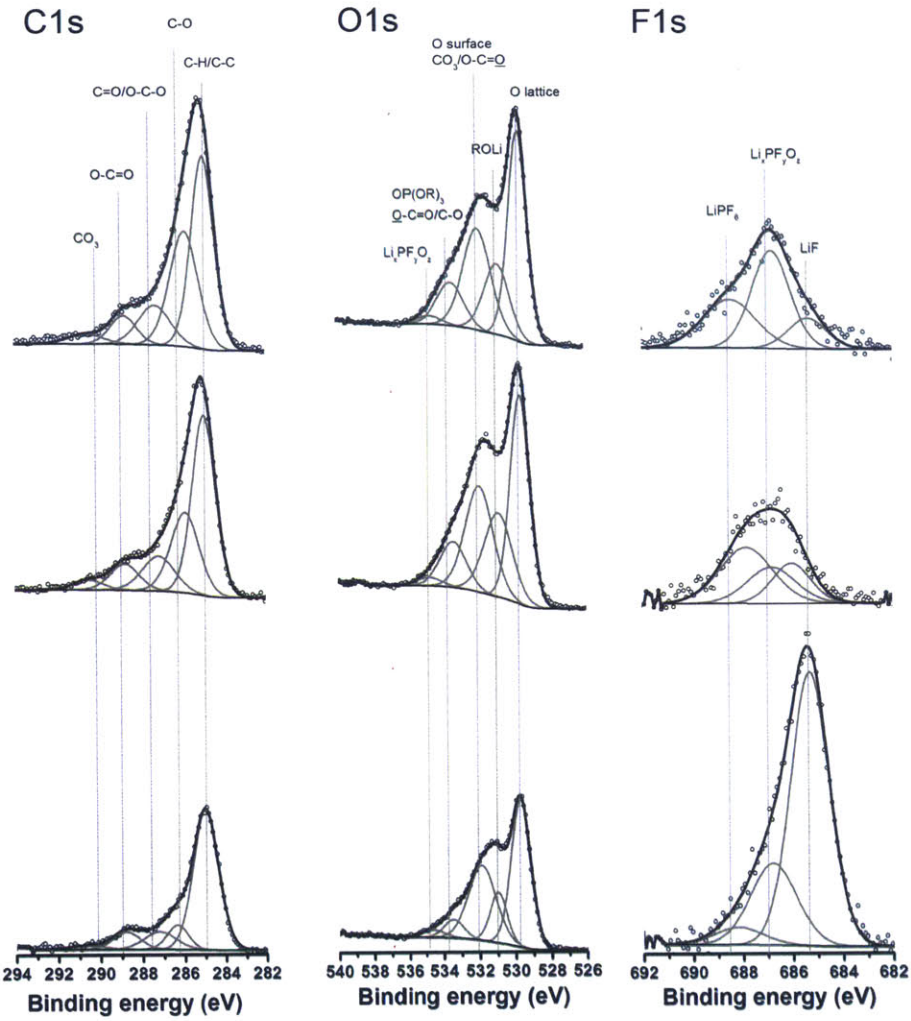

XPS spectra of the C1s, O1s and F1s photoemission lines for the carbon-free, binder-free pristine $LiNi_{1/3}Mn_{1/3}Co_{1/3}O_2$ electrodes and after charging to 4.1 V_{Li}. The lithium amounts of these samples are $Li_{0.58}NMCO_2$, $Li_{0.53}NMCO_2$, and $Li_{0.51}NMCO_2$ respectively. For analysis sample with $Li_{0.51}NMCO_2$ content has been chosen for further analysis.

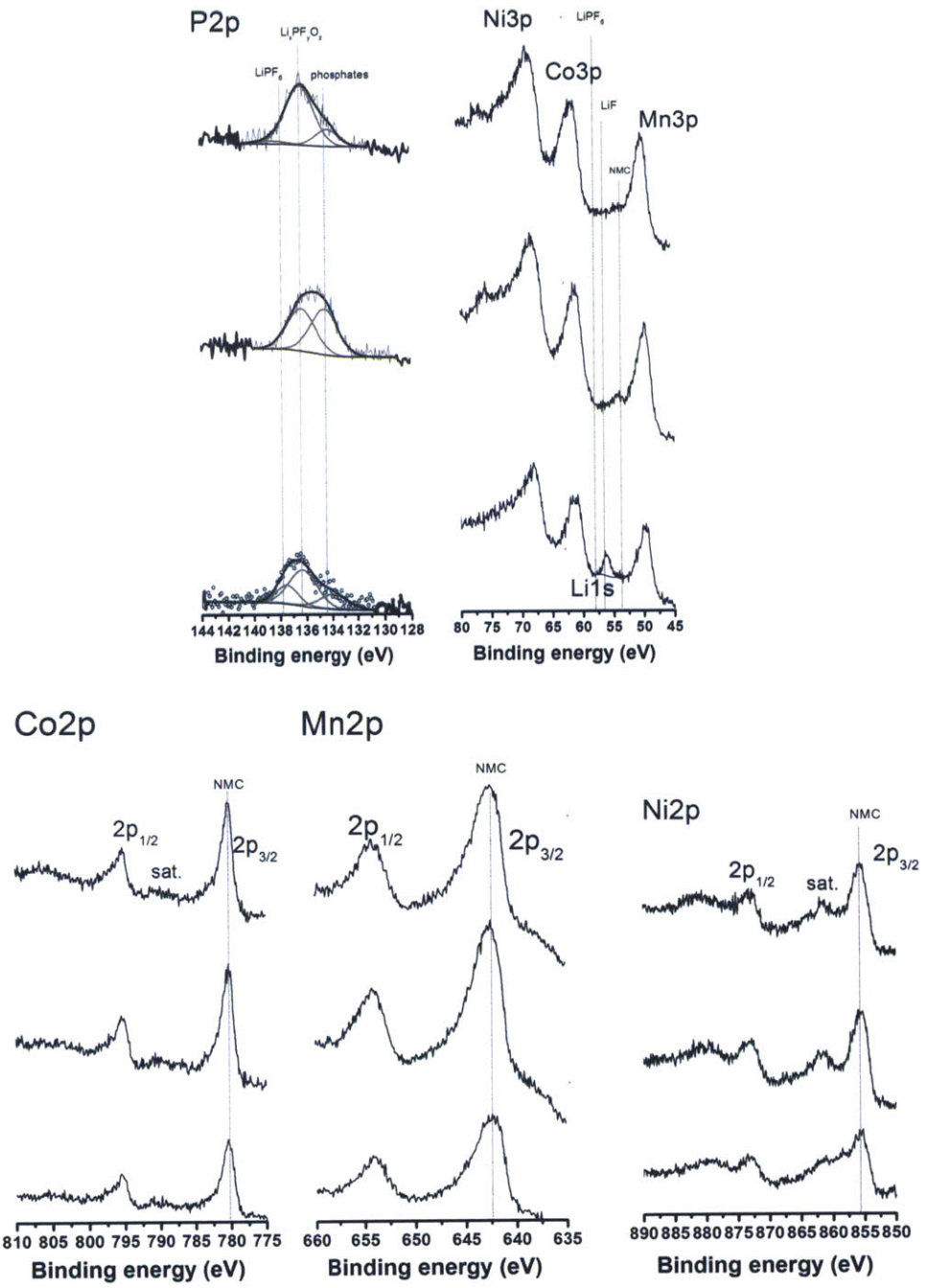

XPS spectra of the P2p, Co3p, Co2p, Mn2p, Ni2p photoemission lines for the carbon-free, binder-free pristine $LiNi_{1/3}Mn_{1/3}Co_{1/3}O_2$ electrodes and after charging to 4.1 V_{Li}. The lithium amounts of these samples are $Li_{0.58}NMCO_2$, $Li_{0.53}NMCO_2$, and $Li_{0.51}NMCO_2$ respectively. For analysis sample with $Li_{0.51}NMCO_2$ content has been chosen for further analysis

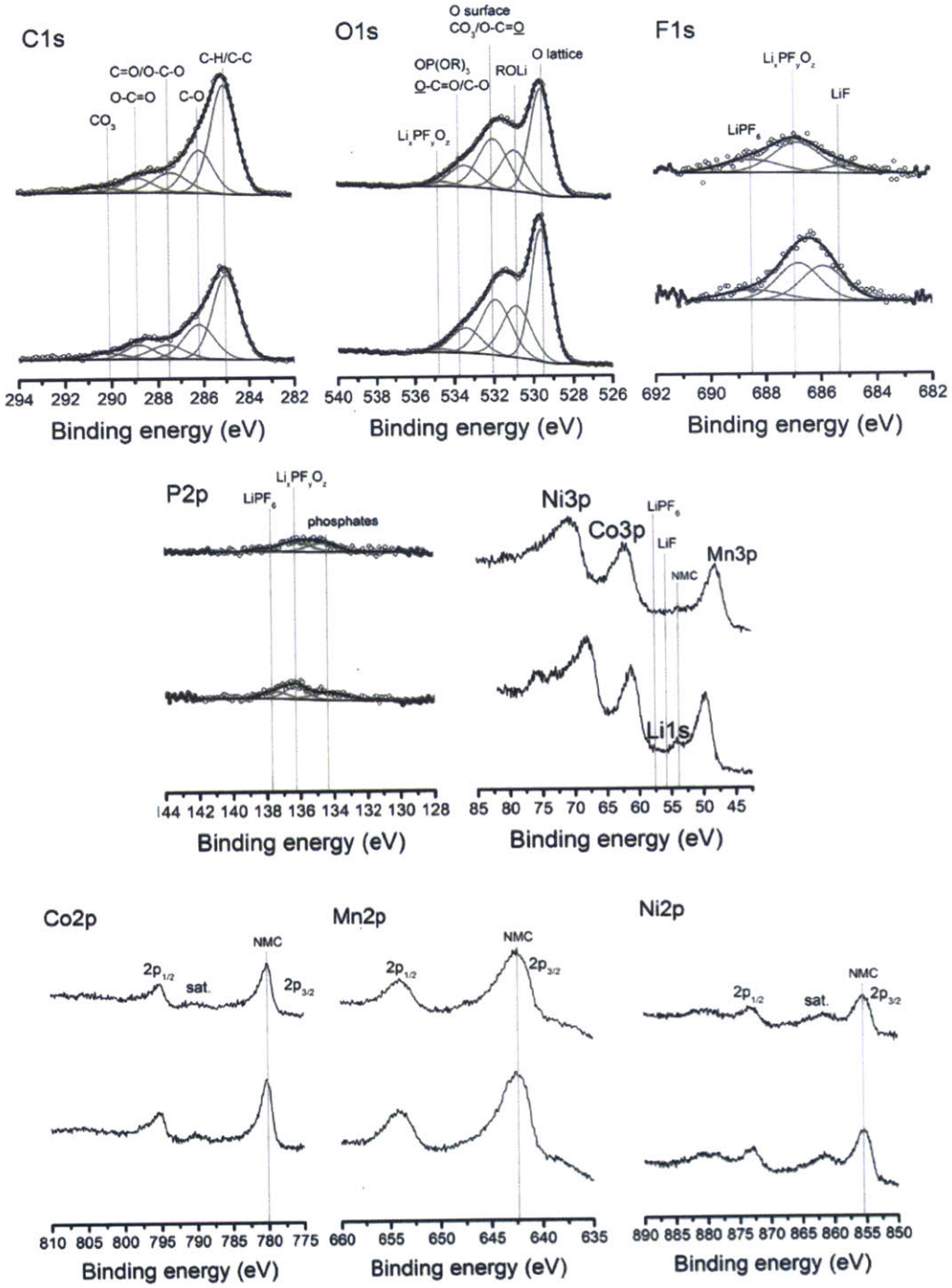

XPS spectra of the C1s, O1s, F1s, P2p, Co3p, Co2p, Mn2p and Ni2p photoemission lines for the carbon-free, binder-free pristine $LiNi_{1/3}Mn_{1/3}Co_{1/3}O_2$ electrodes and after charging to 4.2 V_{Li}. The lithium amounts of these samples are $Li_{0.47}NMCO_2$ and $Li_{0.45}NMCO_2$ respectively. For analysis sample with $Li_{0.45}NMCO_2$ content has been chosen for further analy

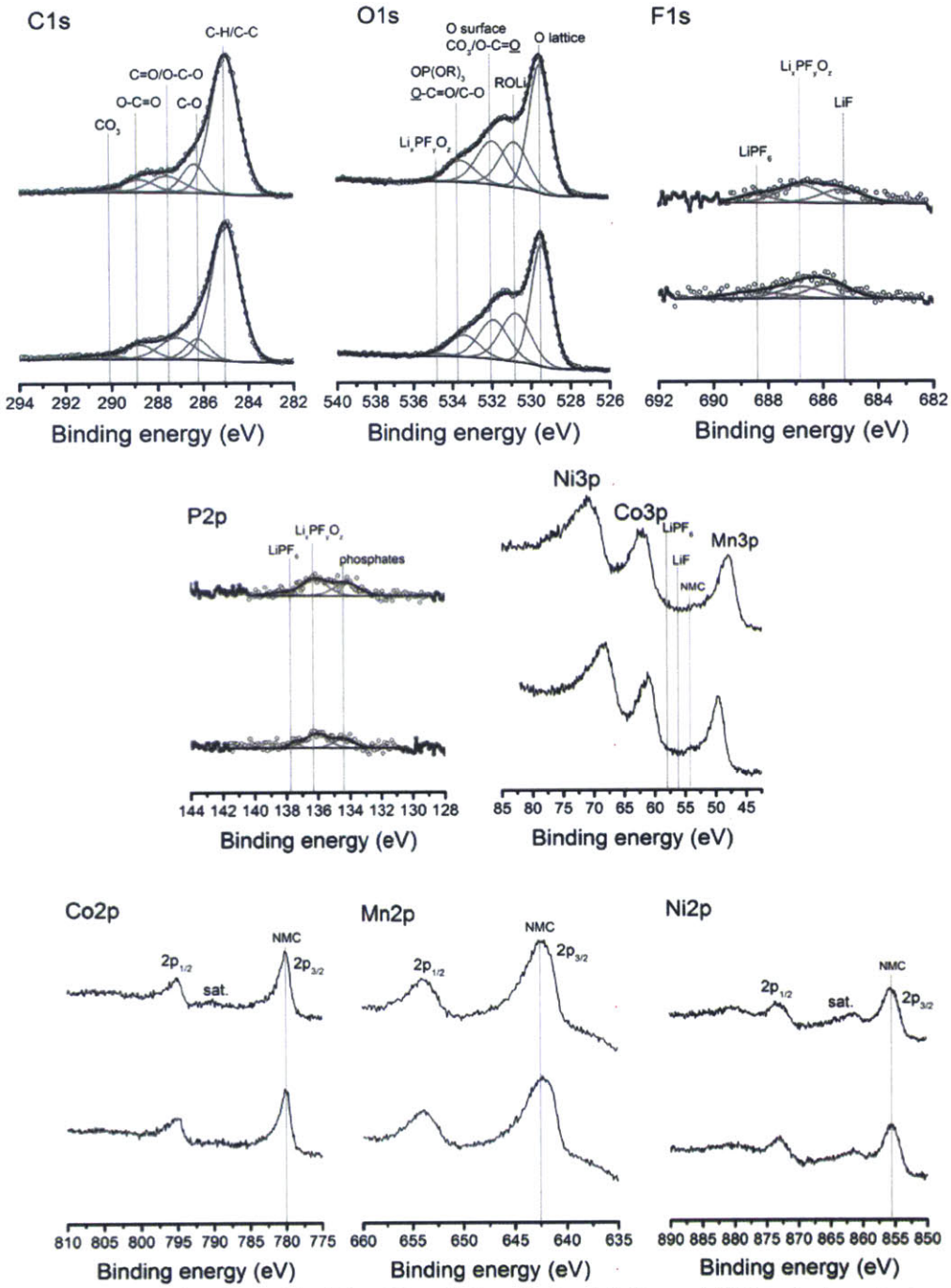

XPS spectra of the C1s, O1s, F1s, P2p, Co3p, Co2p, Mn2p and Ni2p photoemission lines for the carbon-free, binder-free pristine $LiNi_{1/3}Mn_{1/3}Co_{1/3}O_2$ electrodes and after charging to 4.4 V_{Li}. The lithium amounts of these samples are $Li_{0.35}NMCO_2$ and $Li_{0.38}NMCO_2$ respectively. For analysis sample with $Li_{0.35}NMCO_2$ content has been chosen for further analysis.

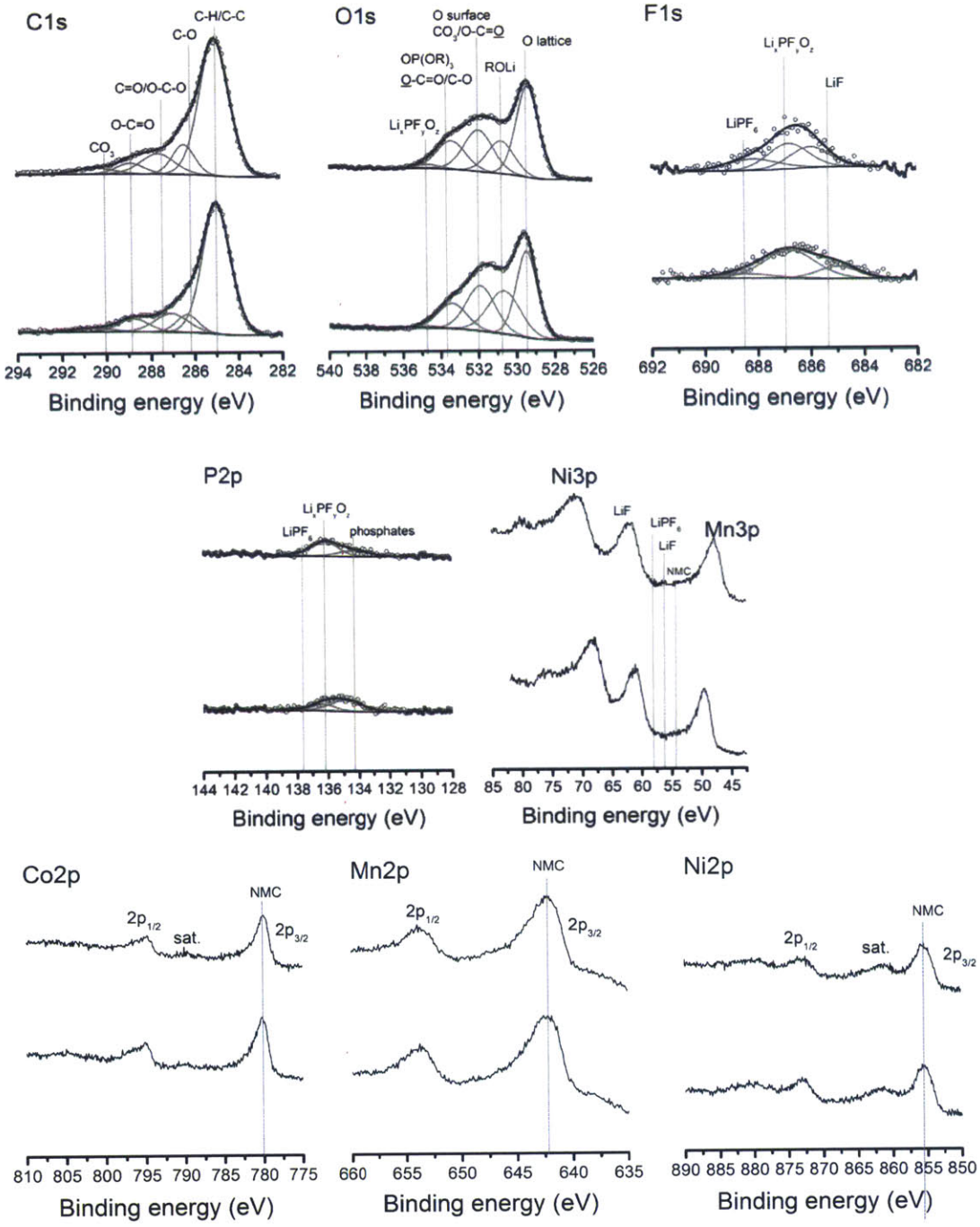

XPS spectra of the C1s, O1s, F1s, P2p, Co3p, Co2p, Mn2p and Ni2p photoemission lines for the carbon-free, binder-free pristine $LiNi_{1/3}Mn_{1/3}Co_{1/3}O_2$ electrodes and after charging to 4.6 V_{Li}. The lithium amounts of these samples are $Li_{0.30}NMCO_2$ and $Li_{0.31}NMCO_2$ respectively. For analysis sample with $Li_{0.31}NMCO_2$ content has been chosen for further analysis.

APPENDIX C: Reproducibility check for Li_2RuO_3 at 3.6 V_{Li}, 3.8 V_{Li}, 4.2 V_{Li}, 4.4 V_{Li} and 4.6 V_{Li}

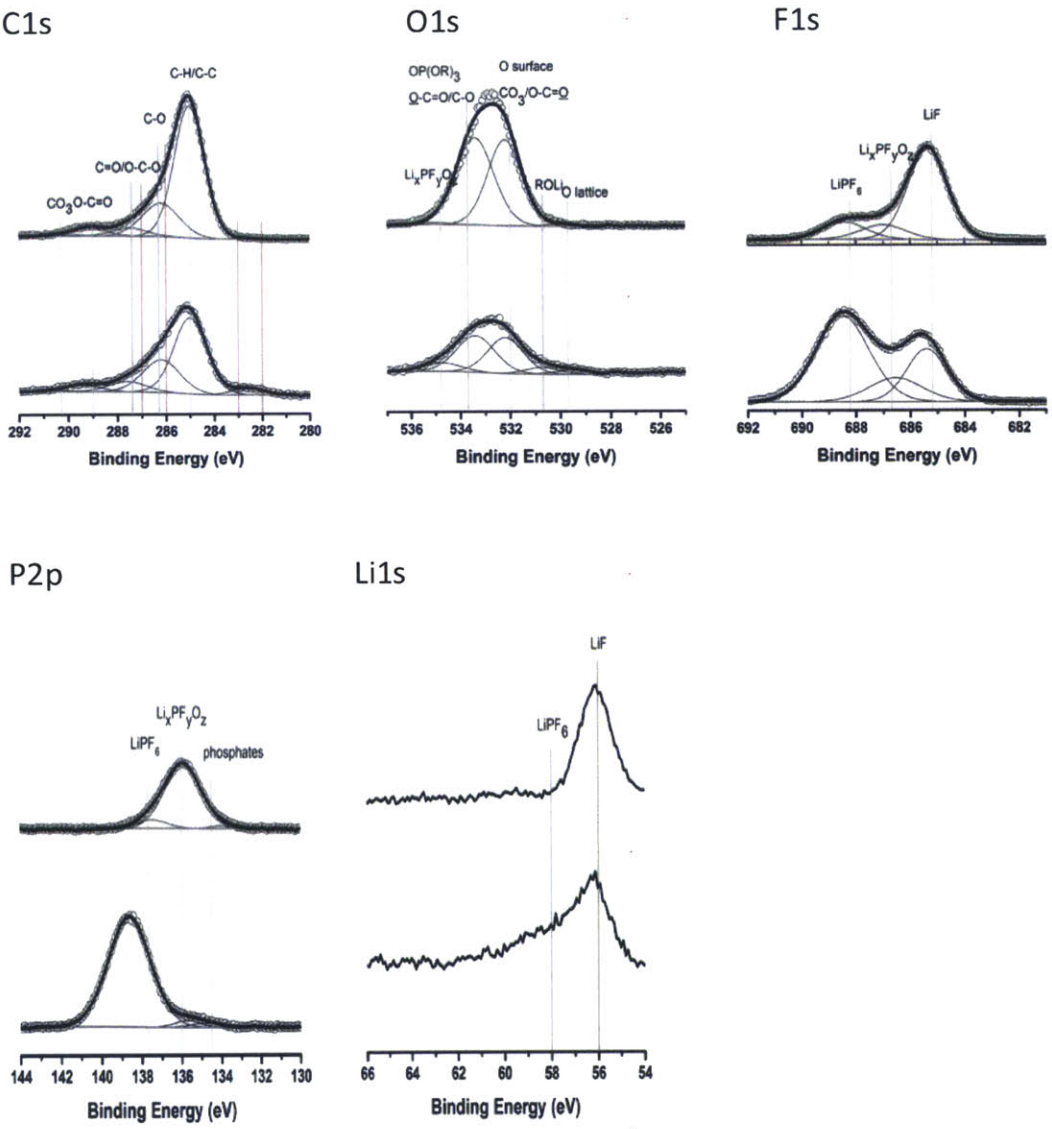

XPS spectra of the C1s, O1s, F1s, P2p and Li1s photoemission lines for the carbon-free, binder-free pristine Li_2RuO_3 electrodes and after charging to 3.6 V_{Li}. For C1s spectra, red lines indicate the Ru peaks and gray lines indicate the C species.

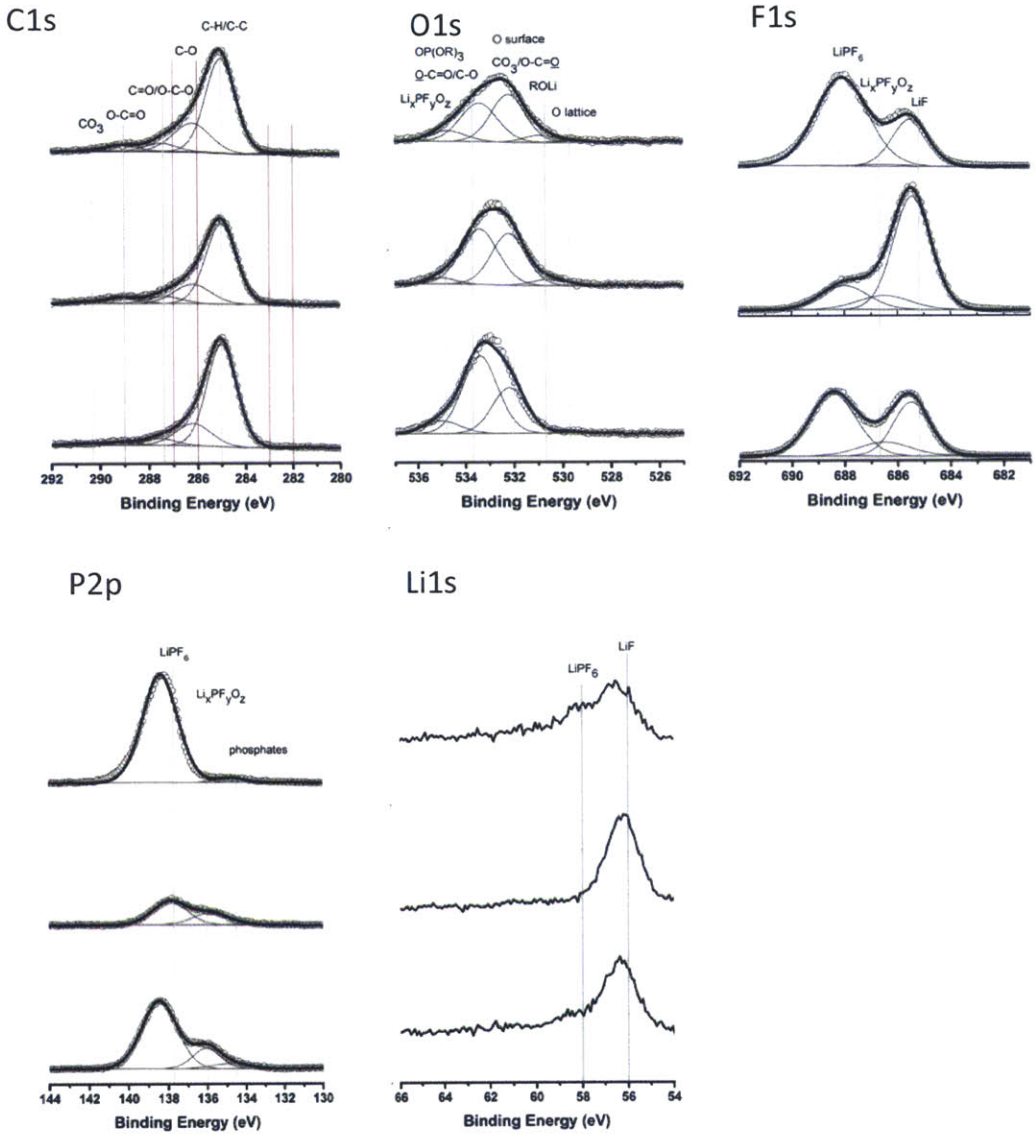

XPS spectra of the C1s, O1s, F1s, P2p and Li1s photoemission lines for the carbon-free, binder-free pristine Li_2RuO_3 electrodes and after charging to 3.8 V_{Li}. For C1s spectra, red lines indicate the Ru peaks and gray lines indicate the C species.

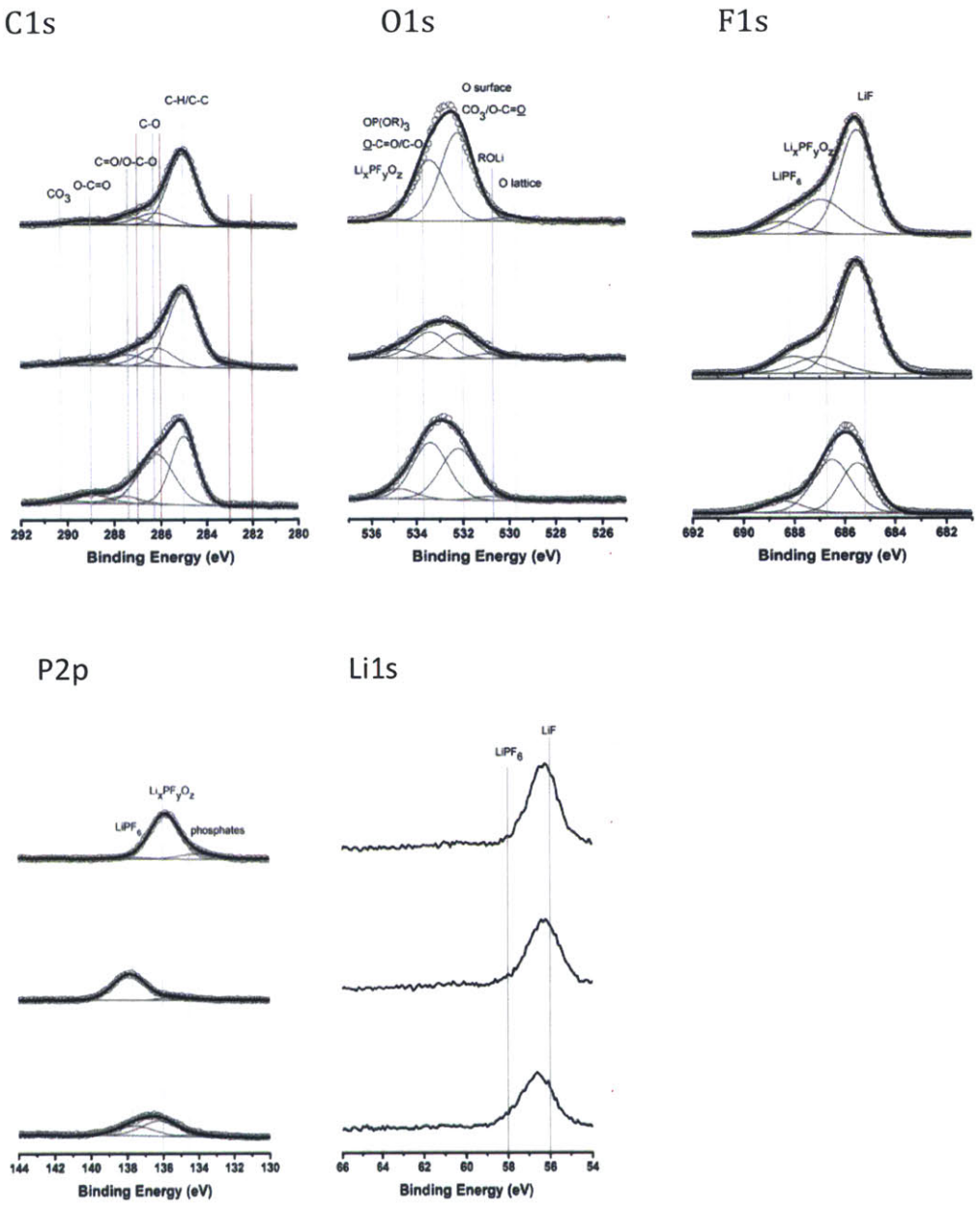

XPS spectra of the C1s, O1s, F1s, P2p and Li1s photoemission lines for the carbon-free, binder-free pristine Li_2RuO_3 electrodes and after charging to 4.2 V_{Li}. For C1s spectra, red lines indicate the Ru peaks and gray lines indicate the C species.

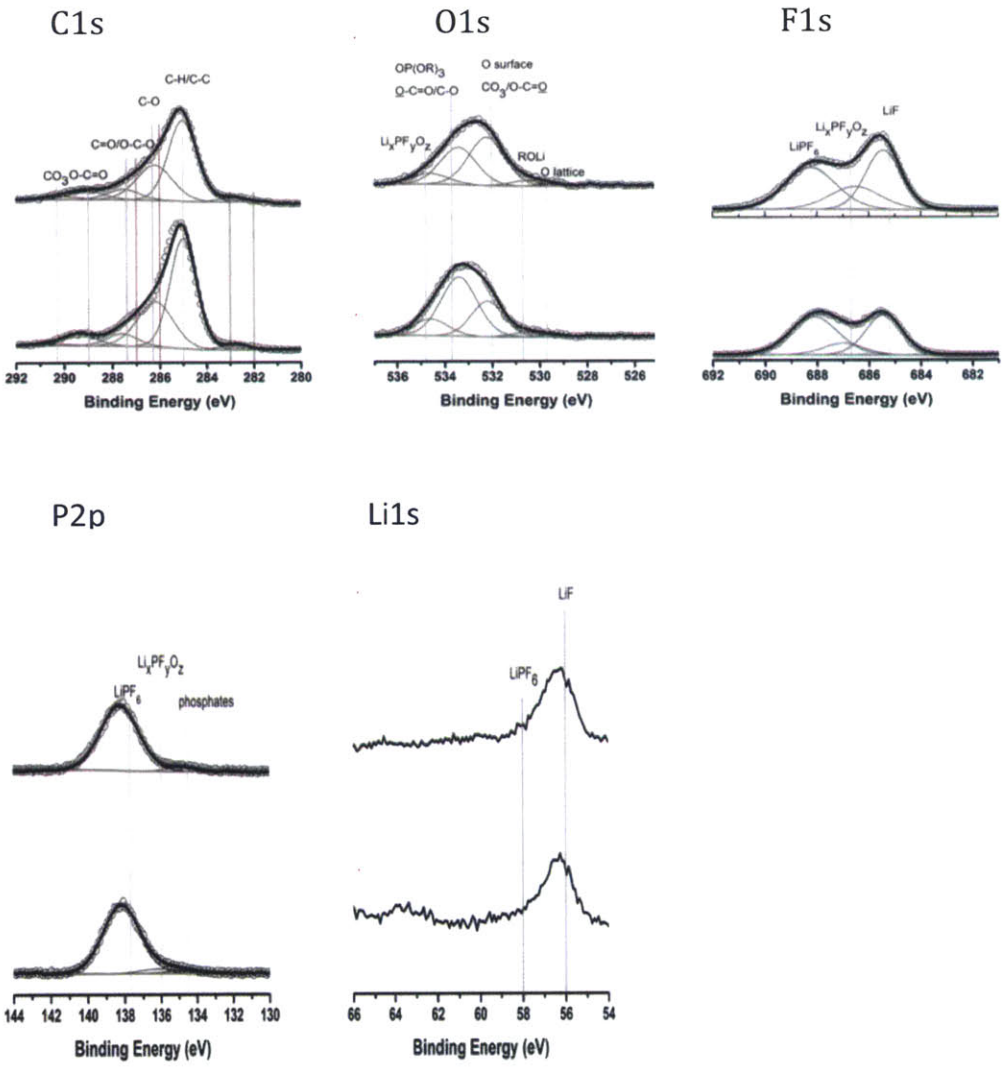

XPS spectra of the C1s, O1s, F1s, P2p and Li1s photoemission lines for the carbon-free, binder-free pristine Li_2RuO_3 electrodes and after charging to 4.4 V_{Li}. For C1s spectra, red lines indicate the Ru peaks and gray lines indicate the C species.

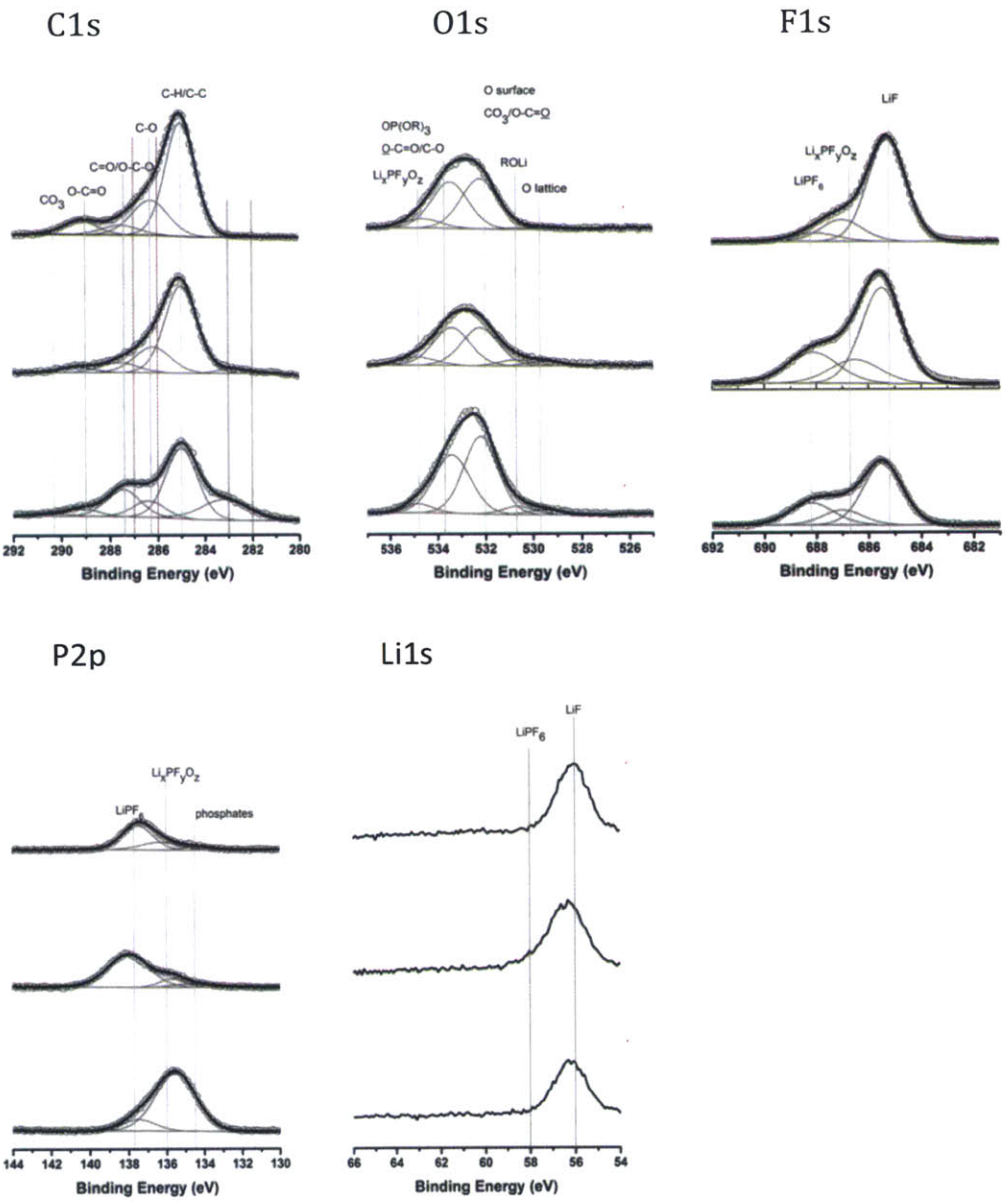

XPS spectra of the C1s, O1s, F1s, P2p and Li1s photoemission lines for the carbon-free, binder-free pristine Li_2RuO_3 electrodes and after charging to 4.6 V_{Li}. For C1s spectra, red lines indicate the Ru peaks and gray lines indicate the C species.

APPENDIX D: Reproducibility check for $Li_2Ru_{0.5}Mn_{0.5}O_3$ at 3.6 V_{Li}, 3.8 V_{Li}, 4.2 V_{Li}, 4.4 V_{Li} and 4.6 V_{Li}

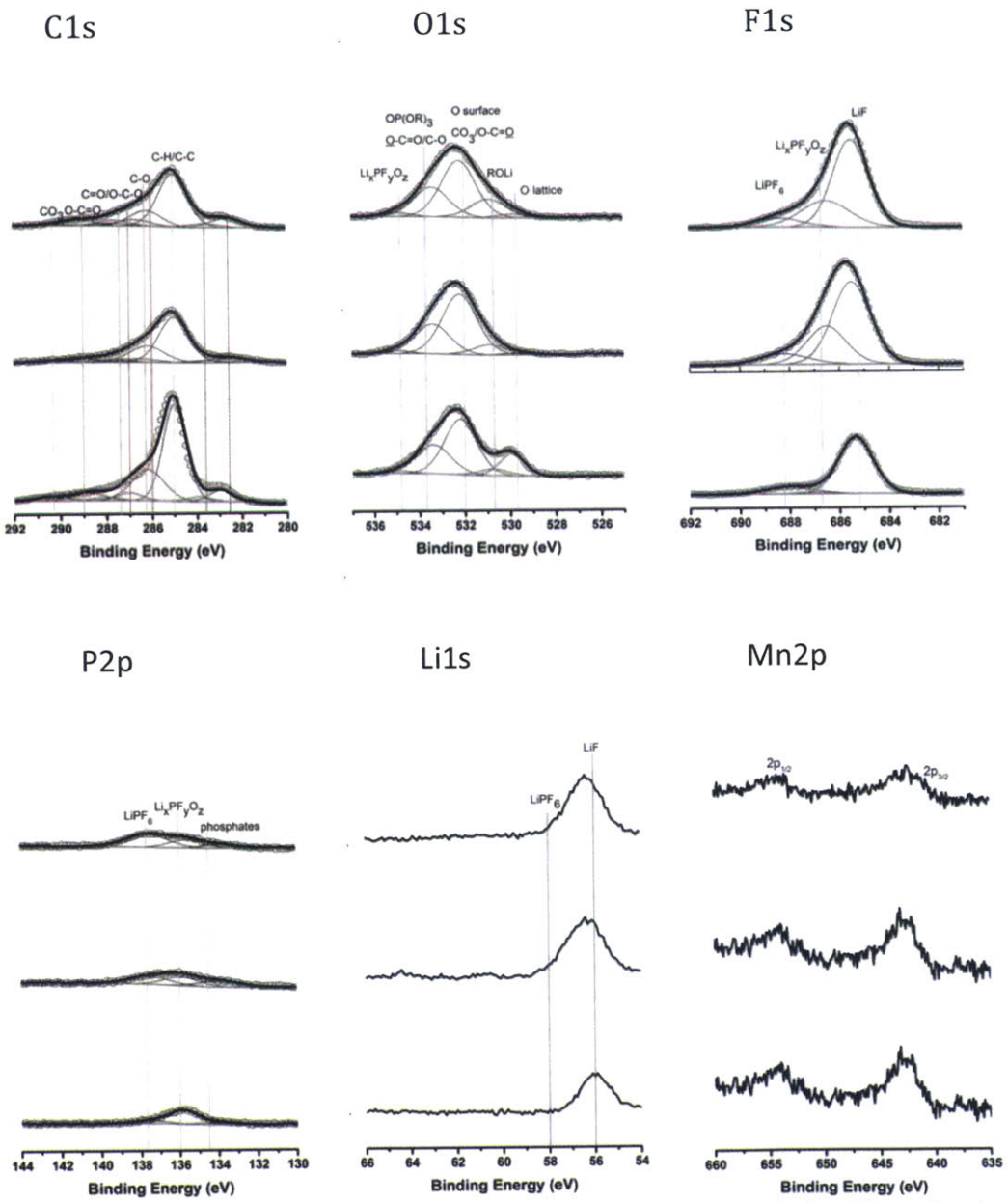

XPS spectra of the C1s, O1s, F1s, P2p, Li1s and Mn2p photoemission lines for the carbon-free, binder-free pristine $Li_2Ru_{0.5}Mn_{0.5}O_3$ electrodes and after charging to 3.6 V_{Li}. For C1s spectra, red lines indicate the Ru peaks and gray lines indicate the C species.

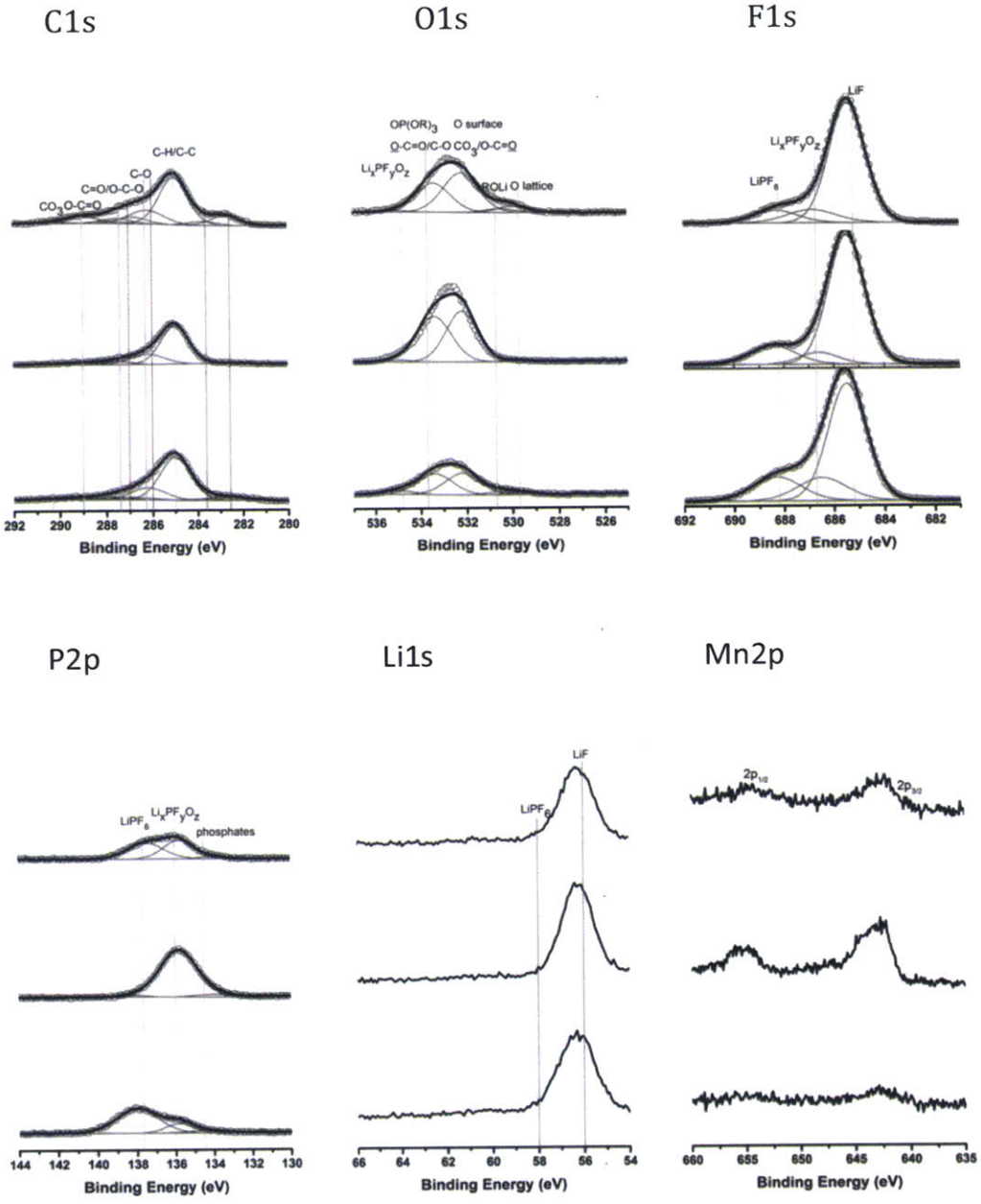

XPS spectra of the C1s, O1s, F1s, P2p, Li1s and Mn2p photoemission lines for the carbon-free, binder-free pristine $Li_2Ru_{0.5}Mn_{0.5}O_3$ electrodes and after charging to 3.8 V_{Li}. For C1s spectra, red lines indicate the Ru peaks and gray lines indicate the C species.

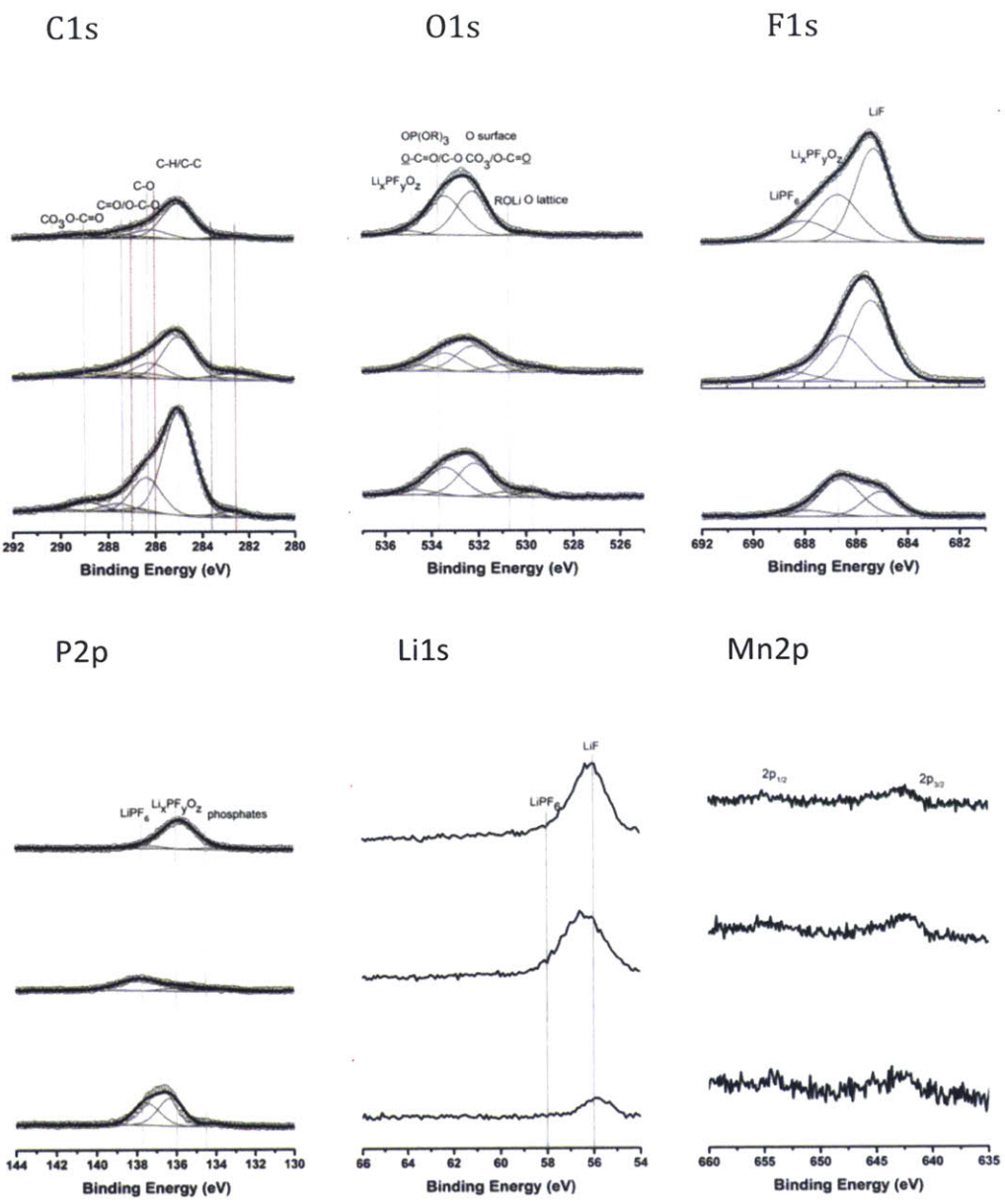

XPS spectra of the C1s, O1s, F1s, P2p, Li1s and Mn2p photoemission lines for the carbon-free, binder-free pristine $Li_2Ru_{0.5}Mn_{0.5}O_3$ electrodes and after charging to 4.2 V_{Li}. For C1s spectra, red lines indicate the Ru peaks and gray lines indicate the C species.

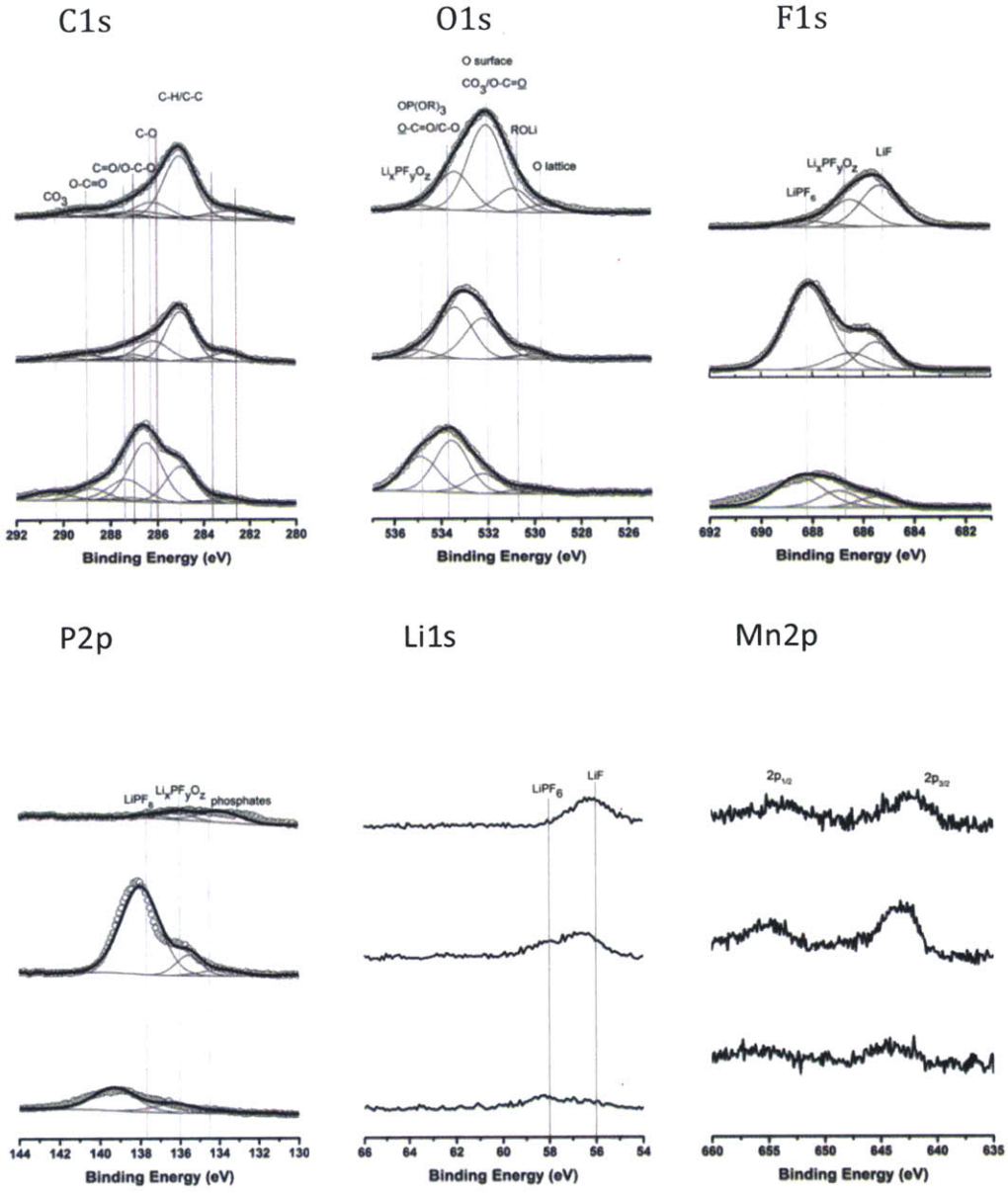

XPS spectra of the C1s, O1s, F1s, P2p, Li1s and Mn2p photoemission lines for the carbon-free, binder-free pristine $Li_2Ru_{0.5}Mn_{0.5}O_3$ electrodes and after charging to 4.4 V_{Li}. For C1s spectra, red lines indicate the Ru peaks and gray lines indicate the C species.

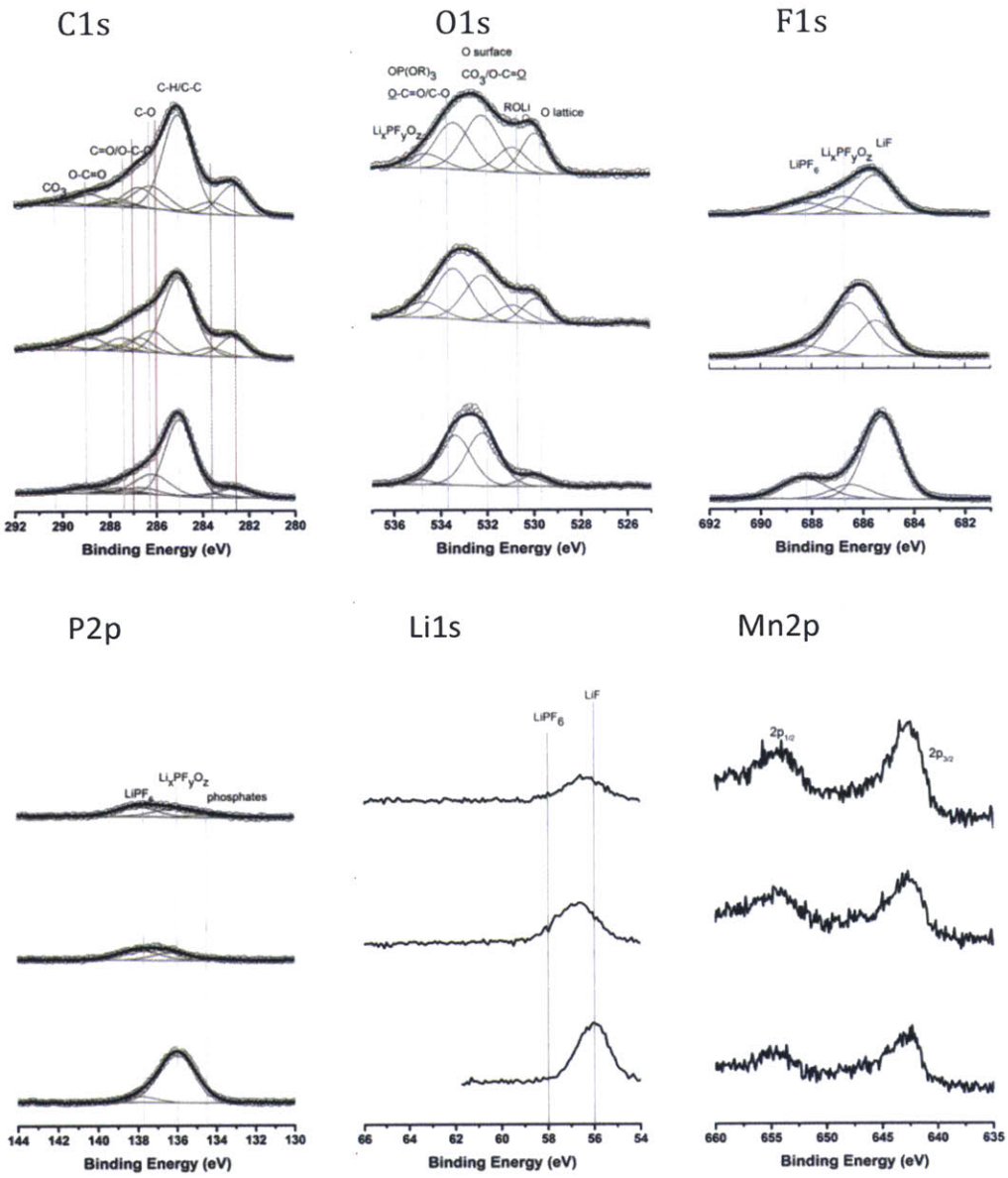

XPS spectra of the C1s, O1s, F1s, P2p, Li1s and Mn2p photoemission lines for the carbon-free, binder-free pristine $Li_2Ru_{0.5}Mn_{0.5}O_3$ electrodes and after charging to 4.6 V_{Li}. For C1s spectra, red lines indicate the Ru peaks and gray lines indicate the C species.

APPENDIX E: Deconvolution Parameters and Quantification for $LiCoO_2$, $LiNi_{1/3}Mn_{1/3}Co_{1/3}O_2$, Li_2RuO_3 and $Li_2Ru_{0.5}Mn_{0.5}O_3$

C1s	CH_x	C-O	C=O/O-C-O	O=C-O	CO_3
Position range	285	286.2-286.5	287.3-287.6	288.8-289.4	290.2-290.6
Width range	1.2-1.6	1.5-1.8	1.5-1.8	1.46-1.6	1.7-2

O1s	O lattice	ROLi	Osurf/CO3/O-C=O	C-O/ O-C=O/OP(OR)3	LixPFyOz
Position range	depends on the material	530.5-530.9	531.9-532.2	533.4-533.9	534.6-535
Width range	1.3-1.6	1.5-1.8	1.6-1.8	1.3-1.8	1.4-1.8

F1s	LiF	LixPFyOz	LiPF6
Position range	685-685.5	686.5-687	688.5-688
Width range	1.6-1.8	1.8-2.3	1.8-2.3

P2p	phosphates	LixPFyOz	LiPF6
Position range	134.8-133.9	135.5-136.3	137.5-138
Width range	1.5-2.5	1.5-2.5	1.5-2.5

RSF values for quantification

F1s	1	Co2p	3.529
O1s	0.733	Mn2p	2.688
C1s	0.314	Ni2p	3.702
P2p	0.525	Co2p 3/2	2.3526
Li1s	0.028	Mn2p 3/2	1.792
		Ni2p 3/2	2.468

For Ru3d

difference main to sat	1eV	same width	Isat/Imain=0.4
spin orbit splitting	4.1eV	I3/2=0.6666*I5/2	

LCO		Pristine			4.1V			4.2V			4.4V			4.6V		
Peak	Species	BE (eV)	FWHM (eV)	At%	BE (eV)	FWHM (eV)	At%	BE (eV)	FWHM (eV)	At%	BE (eV)	FWHM (eV)	At%	BE (eV)	FWHM (eV)	At%
C1s	C-C/C-H	285	1.6	26.5	285	1.5	20.6	285	1.6	24.9	285	1.5	17.8	285	1.5	23.2
	C-O	286.3	1.5	4.2	286.3	1.5	6.1	286.5	1.5	4.2	286.5	1.5	4.0	286.2	1.8	15.6
	C=O/O-C-O	287.6	1.8	6.6	287.6	1.8	3.8	287.6	1.5	2.1	287.6	1.8	2.3	287.5	1.8	4.3
	O=C-O	288.8	1.5	3.0	288.8	1.6	4.1	288.8	1.6	2.3	289.0	1.6	2.1	288.8	1.6	3.5
	CO3	290.6	1.7	0.4	290.2	2.0	1.3	290.3	2.0	1.7	290.2	1.7	0.5	290.6	2	2.2
O1s	O lattice	529.3	1.3	21.1	529.3	1.4	11.8	529.6	1.4	5.6	529.7	1.5	5.4	529.3	1.6	8.6
	ROLi	530.9	1.5	4.7	530.6	1.8	8.3	530.8	1.8	3.8	530.9	1.8	4.0	530.8	1.8	6.0
	Osurf/CO3/O-C=O	531.7	1.7	13.0	531.9	1.8	19.3	532.1	1.7	8.0	532.1	1.8	10.3	532.1	1.8	8.1
	C-O/O-C=O/OP(OR)3	533.3	1.7	2.0	533.4	1.8	5.9	533.4	1.8	3.8	533.4	1.7	3.8	533.4	1.8	6.8
	LixPFyOz	/	/	/	535.0	1.5	0.1	534.7	1.8	0.4	534.8	1.4	0.5	534.6	1.7	1.9
F1s	LiF	/	/	/	685.0	1.8	2.0	685.0	1.6	10.7	685.3	1.8	16.0	685.0	1.8	0.1
	LixPFyOz	/	/	/	686.5	2.0	3.4	686.7	2.1	12.3	686.5	2.0	11.1	686.6	1.8	9.1
	LiPF6	/	/	/	688.0	2.3	1.3	688.0	2.1	1.4	688.0	2.0	2.7	688.1	2.3	4.0
P2p	phosphate	/	/	/	133.9	2.5	0.8	133.9	1.9	0.3	134.3	2.2	0.6	134.1	1.7	0.3
	LixPFyOz	/	/	/	136.0	2.3	0.7	136.3	1.7	0.8	136.3	2.4	1.3	136.3	1.6	1.2
	LiPF6	/	/	/	/	/	/	137.5	1.9	1.2	137.5	1.6	0.3	137.5	1.7	0.6
Li1s	LiCoO2 (54)	54.0	1	11.9	54.0	1.3	4.3	/	/	/	/	/	/	/	/	/
	Li2CO3 (55.5) LiF (56eV)	/	/	/	/	/	/	55.8	1.7	13.3	55.9	1.6	14.5	/	/	/
Co2p	LiCoO2	779.6	1.3	6.6	779.9	1.7	6.2	780.2	1.8	3.2	780.1	1.8	2.8	780.0	1.9	4.5
	satellite	789.5	2.4		789.7	2.3		789.6	4.6		789.8	3.5		789.8	2.6	

NMC		Pristine			4.1V			4.2V			4.4V			4.6V		
Peak	Species	BE (eV)	FWHM (eV)	At%	BE (eV)	FWHM (eV)	At%	BE (eV)	FWHM (eV)	At%	BE (eV)	FWHM (eV)	At%	BE (eV)	FWHM (eV)	At%
C1s	C-C/C-H	285	1.5	21.5	285	1.5	23.9	285	1.5	17.0	285	1.5	31.0	285	1.6	33.2
	C-O	286.4	1.5	3.7	286.2	1.6	12.6	286.2	1.6	7.1	286.4	1.5	5.9	286.5	1.5	6.9
	C=O/O-C-O	287.6	1.7	3.5	287.6	1.5	3.0	287.6	1.8	3.6	287.6	1.8	3.7	287.6	1.8	3.9
	O=C-O	288.8	1.6	3.5	288.8	1.5	3.5	288.8	1.5	2.8	288.8	1.5	3.0	288.8	1.6	3.4
	CO3	290.6	1.7	0.6	290.6	2.0	1.5	290.3	2.0	1.7	290.6	2.0	0.8	290.6	2.0	1.7
O1s	O lattice	529.5	1.3	21.1	529.7	1.3	15.3	529.6	1.3	16.7	529.5	1.3	17.8	529.4	1.4	14.0
	ROLi	531.0	1.5	6.1	531.0	1.5	5.3	531.0	1.8	8.0	530.8	1.8	8.2	530.8	1.6	5.9
	Osurf/CO3/O-C=O	531.8	1.6	9.3	531.9	1.8	9.5	531.9	1.8	9.4	531.9	1.8	8.1	532.0	1.8	8.3
	C-O/O-C=O/OP(OR)3	533.4	1.7	2.0	533.4	1.8	4.2	533.4	1.8	4.6	533.4	1.8	4.3	533.4	1.8	5.7
	LixPFyOz	535.0	1.4	0.1	534.6	1.8	0.7	534.8	1.4	0.4	/	/	/	534.7	1.5	0.6
F1s	LiF	685.0	2.0	2.8	685.0	2.0	1.1	685.1	1.8	0.9	685.4	1.8	1.0	685.4	1.8	0.3
	LixPFyOz	686.6	1.8	0.9	686.7	1.8	4.6	686.5	1.8	5.0	686.7	1.8	1.3	686.5	1.9	4.0
	LiPF6	688.5	2.3	1.5	688.5	2.3	3.0	688.5	2.3	1.2	688.3	1.8	0.4	688.3	2.0	1.2
P2p	phosphate	133.9	2.5	0.4	134.3	2.2	0.4	134.3	2.5	0.5	134.2	1.9	0.4	134.2	2.5	0.4
	LixPFyOz	136.0	2.5	0.4	136.3	2.4	1.2	136.3	1.6	0.5	136.2	1.9	0.5	136.1	2.1	0.9
	LiPF6	138.0	2.5	0.1	137.5	2.5	0.1	137.5	1.9	0.3	138	2.5	0.1	138.0	2.5	0.1
Li1s	NMC	54.4	1.3	11.3	/	/	/	54.1	1.7	8.4	54.1	0.5	1	/	/	/
	Li2CO3/LiF	/	/	/	/	/	/	/	/	/	/	/	/	/	/	/
Co2p	NMC	779.9	1.3	2.5	780.2	1.4	2.1	780.2	1.5	2.8	780.0	1.4	2.8	779.9	1.5	2.0
	satellite	789.7	3.0		790.1	2.7		790.0	2.4		790.2	3.5		789.9	2.1	
Ni2p	NMC	854.6	1.8	4.3	855,4	2.3	3.8	855.2	2.2	4.2	855.2	2.2	4.3	855.1	2.2	3.2
	satellite	861.2	4.0		861.4	3.3		861.3	2.9		861.5	3.0		861.2	2.6	
Mn2p	NCM	641.9	2.3	4.4	642.3	2.4	4.3	642.3	2.3	4.9	642.2	2.3	5.4	642.0	2.4	4.3

LRO		Pristine			3.6 V			3.8 V			4.2V			4.4V			4.6V		
Peak	Species	BE (eV)	FWHM (eV)	At%	BE (eV)	FWHM (eV)	At%	BE (eV)	FWHM (eV)	At%	BE (eV)	FWHM (eV)	At%	BE (eV)	FWHM (eV)	At%	BE (eV)	FWHM (eV)	At%
C1s	C-C/C-H	285	1.6	24.08	285	1.5	16.42	285	1.5	9.66	285	1.5	8.58	285	1.4	11.43	285	1.5	14.06
	C-O	286.2	1.5	6.08	286.2	1.8	5.15	286.2	1.8	2.84	286.2	1.8	1.57	286.2	1.8	6.07	286.2	1.8	4.92
	C=O/O-C-O	287.6	1.8	5.81	287.5	1.7	1.16	287.4	1.5	0.81	287.3	1.6	0.86	287.6	1.5	1.36	287.3	1.8	1.65
	O=C-O	289.4	1.6	5.82	289.2	1.6	1.24	289.0	1.6	0.81	289.2	1.6	0.52	289.1	1.6	1.41	289.1	1.6	1.86
	CO3	290.2	1.7	1.92	290.6	2.0	0.15	290.6	2.0	0.36	290.2	2.0	0.06	290.3	1.7	0.43	290.2	1.7	0.15
O1s	O lattice	529.5	1.5	2.59	530.0	1.3	0.10	529.5	1.6	0.03	530	1.3	0.13	529.5	1.3	0.11	529.6	1.6	0.13
	ROLi	530.9	1.5	3.77	530.5	1.5	0	530.5	1.7	0.27	530.5	1.5	0	530.5	1.5	0.36	530.5	1.5	0
	Osurf/CO3/O-C=O	531.9	1.7	23.47	532.2	1.6	4.66	532.2	1.6	2.11	532.2	1.7	5.28	532.2	1.8	3.36	532.2	1.8	3.35
	C-O/O-C=O/OP(OR)3	533.5	1.4	3.64	533.4	1.7	4.86	533.4	1.8	2.47	533.4	1.6	3.22	533.4	1.8	2.66	533.4	1.7	2.66
	LixPFyOz	534.7	1.4	0.57	535.0	1.4	0.18	535.0	1.4	0.21	535	1.4	0.22	534.6	1.8	0.74	534.6	1.7	0.73
F1s	LiF	685.0	1.8	1.98	685.3	1.7	23.75	685.4	1.7	30.1	685.5	1.6	26.31	685.4	1.6	17.23	685.2	1.7	28.38
	LixPFyOz	687.0	1.8	0.64	686.9	2.0	4.34	686.5	2.3	5.19	686.9	2.3	12.48	686.5	2.3	9.47	687	1.9	6.66
	LiPF6	688.0	2.1	1.59	688.4	1.9	5.11	688.0	2.1	8.06	688.5	1.9	3.77	688.2	2.3	17.37	688	2.0	2.72
P2p	phosphate	134.1	2.5	0.90	133.9	1.5	0.08	133.9	1.8	0.052	134.0	2.4	0.34	134.4	1.5	0.14	134.3	1.9	0.15
	LixPFyOz	135.5	1.7	0.46	135.9	2.1	2.89	135.8	2.1	0.71	135.9	1.9	2.26	135.5	1.5	0	136.3	2.4	0.50
	LiPF6	138.1	2.5	0.07	137.5	1.8	0.32	137.9	2.1	1.35	137.7	2.5	0.097	138	2.5	3.57	137.5	1.9	1.23
Li1s	LRO/LiF	55.0	2.0	15.01	56.1	1.7	29.55	56.3	1.8	34.96	56.2	1.7	34.23	56.4	2.0	33.41	56.5	2.9	30.83
	LiPF6	/	/	/	/	/	/	/	/	/	/	/	/	/	/	/	/	/	/

LRMO		Pristine			3.6 V			3.8 V			4.2V			4.4V			4.6V		
Peak	Species	BE (eV)	FWHM (eV)	At%	BE (eV)	FWHM (eV)	At%	BE (eV)	FWHM (eV)	At%	BE (eV)	FWHM (eV)	At%	BE (eV)	FWHM (eV)	At%	BE (eV)	FWHM (eV)	At%
C1s	C-C/C-H	285	1.6	22.81	285	1.5	10.22	285	1.4	5.840	285	1.6	8.043	285	1.6	16.84	285	1.6	24.06
	C-O	286.4	1.5	6.27	286.2	1.6	3.13	286.3	1.5	2.01	286.2	1.7	3.00	286.2	1.6	3.85	286.2	1.7	5.83
	C=O/O-C-O	287.6	1.5	4.24	287.6	1.5	1.08	287.6	1.7	0.51	287.6	1.6	1.03	287.3	1.6	1.41	287.6	1.5	1.29
	O=C-O	288.8	1.6	5.43	289.1	1.6	1.16	288.9	1.6	0.28	289.0	1.6	0.80	289.1	1.6	1.43	288.8	1.6	3.10
	CO3	290.2	1.7	2.12	290.2	1.7	0.29	290.3	2.0	0.31	290.5	2.5	0.30	290.2	2.0	0.69	290.3	1.8	1.23
O1s	O lattice	529.2	1.4	9.29	529.8	1.6	0.33	529.8	1.3	0.1	529.5	1.6	0.39	529.5	1.6	0.97	529.9	1.3	2.61
	ROLi	530.7	1.5	6.05	530.9	1.8	1.92	530.9	1.5	0	530.9	1.7	0.67	530.9	1.6	2.91	530.9	1.5	1.83
	Osurf/CO3/O-C=O	531.9	1.8	22.51	532.2	1.8	5.89	532.2	1.6	4.07	532.2	1.8	2.51	532.0	1.8	11.6	532.2	1.8	4.85
	C-O/O-C=O/OP(OR)3	533.4	1.8	6.17	533.4	1.8	3.09	533.4	1.8	4	533.4	1.8	1.76	533.4	1.7	4.93	533.4	1.8	4.05
	LixPFyOz	535	1.4	0.012	534.9	1.4	0.30	535	1.4	0.12	534.7	1.8	0.57	534.9	1.4	0.49	534.6	1.8	1.23
F1s	LiF	/	/	/	685.5	1.6	26.2	685.5	1.7	33.71	685.4	1.8	24.45	685.3	1.8	17.19	685.5	1.8	15.64
	LixPFyOz	/	/	/	686.5	2.3	10.99	686.6	1.8	3.36	686.5	2.0	15.69	686.5	1.8	11.34	686.7	2.0	7.71
	LiPF6	/	/	/	688.4	2.2	3.52	688.4	2.2	6.29	688.5	2.0	3.17	688.2	2.3	3.11	688.3	2.3	5.95
P2p	phosphate	/	/	/	133.9	2.1	0.19	134.0	2.2	0.15	133.9	2.5	0.16	133.9	2.5	1.08	134.4	2.1	0.22
	LixPFyOz	/	/	/	135.6	2	0.47	135.9	2.3	2.79	135.6	2.0	0.21	136.1	1.8	0.49	136.2	2.5	0.74
	LiPF6	/	/	/	137.6	2.5	0.96	138	1.5	0.05	138	2.5	0.83	137.5	2.1	0.25	138.0	2.4	0.89
Li1s	LRMO/LiF	54.5	2.3	10.59	56.3	1.9	29.6	56.2	1.63	35.93	56.4	2.3	35.87	56.2	2.2	20.32	56.5	2.1	16.67
	LiPF6	/	/	/	/	/	/	/	/	/	/	/	/	/	/	/	/	/	/

REFERENCES

1. Gonzalez Palencia, J.C., Sasamaki T., Araki M., Shiga S. Impact of powertrain electrification, vehicle size reduction and lightweight materials substitution on energy use, CO_2 emissions and cost of a passenger light-duty vehicle fleet. *J. Energy*. **93**, 1489-1504 *(2015)*.
2. Larcher D, Tarascon J. Towards greener and more sustainable batteries for electrical energy storage. *Nature Chemistry*. **7(1)**, 19-29 (2015).
3. Manzetti S., Mariasiu F. Electric vehicle battery technologies: From present state to future systems. *Renewable and Sustainable Energy Reviews* **51**, 1004-1012 (2015).
4. Etacheri V., Marom R., Elazari R., Salitra G., Aurbach D. Challenges in the development of advanced Li-ion batteries: a review. *Energy Environ. Sci.* **4**, 3243-3262 (2011).
5. Bruce P.G., Freunberger S.A., Hardwick L.J., Tarascon J. Li–O2 and Li–S batteries with high energy storage. *Nature Materials* **11**, 19–29 (2012).
6. Andre D, Kim S., Lamp P., Lux S., Maglia F., Paschos O., Stiaszny B. Future generations of cathode materials: an automotive industry perspective J. Mater. Chem. A **3**, 6709–6732 (2015).
7. Armand, M., Tarascon, J.-M. Building Better Batteries. *Nature* **451**, 652–657 (2008).
8. Goodenough, J. B., Kim, Y. Challenges for Rechargeable Li Batteries†. *Chem. Mater.* **22**, 587–603 (2010).
9. Roy P, Srivastava S. K. Nanostructured anode materials for lithium ion batteries *J. Mater. Chem. A* **3**, 2454-2484 (2015).
10. Bruce, P. G., Scrosati, B., Tarascon, J.-M. Nanomaterials for Rechargeable Lithium Batteries. *Angew. Chem. Int. Ed.* **47**, 2930–2946 (2008).
11. Yazami, R., Touzain, P. A Reversible Graphite-Lithium Negative Electrode for Electrochemical Generators. *J. Power Sources* **9**, 365–371 (1983).
12. Mizushima, K., Jones, P. C., Wiseman, P. J., Goodenough, J. B. Li_xCoO_2 ($0<x<1$): A New Cathode Material for Batteries of High Energy Density. *Mater. Res. Bull.* **15**, 783–789 (1980).
13. Thomas, M. G. S. R., David, W. I. F., Goodenough, J. B., Groves, P. Synthesis and Structural Characterization of the Normal Spinel $Li[Ni_2]O_4$. *Mater. Res. Bull.* **20**, 1137–1146 (1985).
14. Dahn J.R., Reimers J.R., Electrochemical and In Situ X-Ray Diffraction Studies of Lithium Intercalation in Li x CoO2. *J. Electrochem. Soc.* **139**, 2091 (1992).
15. Julien C.M., Mauger A., Zaghib K., Groult H. Comparative Issues of Cathode Materials for Li-Ion Batteries *Inorganics* **2**, 132-154 (2014).
16. Huggins RA. Advanced Batteries - Materials Science Aspects *Springer* (2009).
17. Linden D, Reddy TB. Handbook of Batteries, 3rd Edition, McGraw-Hill Inc., 2002
18. Brian L. Ellis, Kyu Tae Lee, and Linda F. Nazar Positive Electrode Materials for Li-Ion and Li-Batteries *Chem. Mater.* **22**, 691–714 (2010).

19. Koltypin M., Aurbach D., Nazar L., Ellis B. More on the performance of LiFePO4 electrodes-The effect of synthesis route, solution composition, aging and temperature *Journal of Power Sources* **174**, 1241–1250 (2007).
20. Huang et al. Oxygen-Vacancy Ordering at Surfaces of Lithium Manganese (III,IV) Oxide Spinel Nanoparticles. *Angew. Chem. Int. Ed.* **50**, 3053 –3057 (2011).
21. Li Y., Lin Z., Li Y., Chen C., He Y., Yang X. Preparation and electrochemical properties of Li-rich spinel-type lithium manganate coated LiMn2O4. *Materials Research Bulletin* **46**, 2450-2455 (2011).
22. M. Hirayama et al. Dynamic Structural Changes at LiMn2O4 /Electrolyte Interface during Lithium Battery Reaction *Journal of Power Sources* **168**, 493–500 (2007).
23. Chen Z., Dahn J.R. Improving the Capacity Retention of LiCoO2 Cycled to 4.5 V by Heat-Treatment *Electrochemical and Solid-State Letters* **7**(1), A11-A14 (2004)
24. Thackeray, M. M., Johnson, C. S., Vaughey, J. T., Li, N., Hackney, S. A. Advances in Manganese-Oxide "composite" Electrodes for Lithium-Ion Batteries. *J. Mater. Chem.* **15 (23)**, 2257–2267 (2005).
25. Armstrong, A. R., Holzapfel, M., Novak, P., Johnson, C. S., Kang, S.-H., Thackeray, M. M., Bruce, P. G. Demonstrating Oxygen Loss and Associated Structural Reorganization in the Lithium Battery Cathode Li[Ni0.2Li0.2Mn0.6]O2. *J. Am. Chem. Soc.* **128**, 8694–8698 (2006).
26. Koga, H., Croguennec, L., Ménétrier, M., Douhil, K., Belin, S., Bourgeois, L., Suard, E., Weill, F., Delmas, C. Reversible Oxygen Participation to the Redox Processes Revealed for Li1.20Mn0.54Co0.13Ni0.13O2. *J. Electrochem. Soc.* **160** (6), A786–A792 (2013).
27. Sathiya, M., Rousse, G., Ramesha, K., Laisa, C. P., Vezin, H., Sougrati, M. T., Doublet, M.-L., Foix, D., Gonbeau, D., Walker, W., Reversible Anionic Redox Chemistry in High-Capacity Layered-Oxide Electrodes. *Nat. Mater.* **12** (9), 827–835 (2013).
28. Sathiya, M., Leriche, J.-B., Salager, E., Gourier, D., Tarascon, J.-M., Vezin, H. Electron Paramagnetic Resonance Imaging for Real-Time Monitoring of Li-Ion Batteries. *Nat. Commun.* **6** (2013).
29. Gauthier, M., Carney, T. J., Grimaud, A., Giordani, L., Pour, N., Chang, H.-H., Fenning, D. F., Lux, S. F., Paschos, O., Bauer, C., et al. The Electrode-Electrolyte Interface in Li-Ion Batteries: Current Understanding and New Insights J. Phys. Chem. Lett. **6**, 4653–4672 (2015).
30. Sathiya et al., High Performance Li2Ru1-yMnyO3 ($0.2 \leq y \leq 0.8$) Cathode Materials for Rechargeable Lithium-Ion Batteries: Their Understanding *Chemistry of Materials* **25,** 1121–31 (2013).
31. Kobayashi et al., Structure and lithium deintercalation of $Li_{2-x}RuO_3$ *Solid State Ionics* **82**, 25–31 (1995).
32. Smith, A. J., Burns, J. C., Trussler, S., Dahn, J. R Precision Measurements of the Coulombic Efficiency of Lithium-Ion Batteries and of Electrode Materials for Lithium-Ion Batteries. *J. Electrochem. Soc.* **157**, A196–A202 (2010).

33. Shim, J., Kostecki, R., Richardson, T., Song, X., Striebel, K. A. Electrochemical Analysis for Cycle Performance and Capacity Fading of a Lithium-Ion Battery Cycled at Elevated Temperature. *J. Power Sources* **112**, 222–230 (2002).
34. Menkin, S., Golodnitsky, D., Peled, E. Artificial Solid-Electrolyte Interphase (SEI) for Improved Cycleability and Safety of Lithium–ion Cells for EV Applications. *Electrochem. Commun.* **11**, 1789–1791 (2009).
35. Aurbach, D., Zinigrad, E., Teller, H., Dan, P. Factors Which Limit the Cycle Life of Rechargeable Lithium (Metal) Batteries. *J. Electrochem. Soc.* **147**, 1274–1279 (2000).
36. Crowther, O, West, A. C. Effect of Electrolyte Composition on Lithium Dendrite Growth. *J. Electrochem. Soc.* **155**, A806 (2008).
37. Bhattacharyya, R., Key, B., Chen, H., Best, A. S., Hollenkamp, A. F., Grey, C. P. In Situ NMR Observation of the Formation of Metallic Lithium Microstructures in Lithium Batteries. *Nat Mater* **9**, 504–510 (2010).
38. Reynier, Y. F., Yazami, R., Fultz, B. Thermodynamics of Lithium Intercalation into Graphites and Disordered Carbons. *J. Electrochem. Soc.* **151**, A422–A426 (2004).
39. Wang, J., Raistrick, I. D., Huggins, R. A. Behavior of Some Binary Lithium Alloys as Negative Electrodes in Organic Solvent-Based Electrolytes. *J. Electrochem. Soc.* **133**, 457–460 (1986).
40. Weydanz, W. J., Wohlfahrt-Mehrens, M., Huggins, R. A. A Room Temperature Study of the Binary Lithium–silicon and the Ternary Lithium–chromium–silicon System for Use in Rechargeable Lithium Batteries. *J. Power Sources* **81–82**, 237–242 (1999).
41. Kim, Y., Goodenough, J. B. Lithium Insertion into Transition-Metal Monosulfides: Tuning the Position of the Metal 4s Band. *J. Phys. Chem. C* **112**, 15060–15064 (2008).
42. Goodenough, J. B., Kim, Y. Locating Redox Couples in the Layered Sulfides with Application to $Cu[Cr_2]S_4$. *J. Solid State Chem.* **182**, 2904–2911 (2009).
43. Xing, L., Borodin, O., Smith, G. D., Li, W. Density Functional Theory Study of the Role of Anions on the Oxidative Decomposition Reaction of Propylene Carbonate. *J. Phys. Chem. A* **115**, 13896–13905 (2011).
44. Zhang, X., Pugh, J. K., Ross, P. N. Computation of Thermodynamic Oxidation Potentials of Organic Solvents Using Density Functional Theory. *J. Electrochem. Soc.* **148**, E183–E188 (2001).
45. Borodin, O., Jow, T. R. Quantum Chemistry Studies of the Oxidative Stability of Carbonate, Sulfone and Sulfonate-Based Electrolytes Doped with BF_4^-, PF_6^- Anions. *ECS Trans.* **33**, 77–84 (2011).
46. Wang, Y., Nakamura, S., Ue, M., Balbuena, P. B. Theoretical Studies To Understand Surface Chemistry on Carbon Anodes for Lithium-Ion Batteries: Reduction Mechanisms of Ethylene Carbonate. *J. Am. Chem. Soc.* **123**, 11708–11718 (2001).
47. Leung, K. Two-Electron Reduction of Ethylene Carbonate: A Quantum Chemistry Re-Examination of Mechanisms. *Chem. Phys. Lett.* **568-569**, 1–8 (2013).

48. Vollmer, J. M., Curtiss, L. A., Vissers, D. R., Amine, K. Reduction Mechanisms of Ethylene, Propylene, and Vinylethylene Carbonates A Quantum Chemical Study. *J. Electrochem. Soc.* **151**, A178–A183 (2004).
49. Egashira, M., Takahashi, H., Okada, S., Yamaki, J. Measurement of the Electrochemical Oxidation of Organic Electrolytes Used in Lithium Batteries by Microelectrode. *J. Power Sources* **92**, 267–271. (2001).
50. Xu, K., Ding, S. P., Jow, T. R. Toward Reliable Values of Electrochemical Stability Limits for Electrolytes. *J. Electrochem. Soc.* **146**, 4172–4178 (1999).
51. Hayashi, K., Nemoto, Y., Tobishima, S., Yamaki, J. Mixed Solvent Electrolyte for High Voltage Lithium Metal Secondary Cells. *Electrochim. Acta* **44**, 2337–2344 (1999).
52. Peled, E. The Electrochemical Behavior of Alkali and Alkaline Earth Metals in Nonaqueous Battery Systems—The Solid Electrolyte Interphase Model. *J. Electrochem. Soc.* **126**, 2047–2051 (1979).
53. Kanamura, K., Tamura, H., Shiraishi, S., Takehara, Z. XPS Analysis of Lithium Surfaces Following Immersion in Various Solvents Containing $LiBF_4$. *J. Electrochem. Soc.* **142**, 340–347 (1995).
54. Eshkenazi, V., Peled, E., Burstein, L., Golodnitsky, D. XPS Analysis of the SEI Formed on Carbonaceous Materials. *Solid State Ion.* **170**, 83–91 (2004).
55. Aurbach, D., Weissman, I., Zaban, A., Chusid, O. Correlation between Surface Chemistry, Morphology, Cycling Efficiency and Interfacial Properties of Li Electrodes in Solutions Containing Different Li Salts. *Electrochim. Acta* **39**, 51–71 (1994).
56. Zaban, A., Zinigrad, E., Aurbach, D. Impedance Spectroscopy of Li Electrodes. 4. A General Simple Model of the Li–Solution Interphase in Polar Aprotic Systems. *J. Phys. Chem.* **100**, 3089–3101 (1996).
57. Aurbach, D., Markovsky, B., Shechter, A., Ein-Eli, Y., Cohen, H. A Comparative Study of Synthetic Graphite and Li Electrodes in Electrolyte Solutions Based on Ethylene Carbonate-Dimethyl Carbonate Mixtures. *J. Electrochem. Soc.* **143**, 3809–3820 (1996).
58. Suo, L., Hu, Y-S., Li, H., Armand, M., Chen, L. A new class of Solvent-in-Salt electrolyte for high-energy rechargeable metallic lithium batteries. *Nat. Comm.* **4**, 1481 (2013).
59. Yamada, Y., Furukama, K., Sodeyama, K., Kikuchi, K., Yaegashi, M, Tateyama, Y., Yamada, A. Unusual Stability of Acetonitrile-Based Superconcentrated Electrolytes for Fast-Charging Lithium-Ion Batteries. *J. Am. Chem. Soc.* **136**, 5039-5046 (2014).
60. Thomas, M. G. S. R., Bruce, P. G., Goodenough, J. B. AC Impedance Analysis of Polycrystalline Insertion Electrodes: Application to $Li_{1-x}CoO_2$. *J. Electrochem. Soc.* **132**, 1521–1528 (1985).
61. Kanamura, K., Toriyama, S., Shiraishi, S., Ohashi, M., Takehara, Z. Studies on Electrochemical Oxidation of Non-Aqueous Electrolyte on the LiCoO2 Thin Film Electrode. *J. Electroanal. Chem.* **419 (1)**, 77–84 (1996).
62. Aurbach, D., Levi, M. D., Levi, E., Teller, H., Markovsky, B., Salitra, G., Heider, U., Heider, L. Common Electroanalytical Behavior of Li Intercalation Processes

into Graphite and Transition Metal Oxides. *J. Electrochem. Soc.* **145 (9)**, 3024–3034 (1998).
63. Aurbach, D. Review of Selected Electrode–solution Interactions Which Determine the Performance of Li and Li Ion Batteries. *J. Power Sources* **89 (2)**, 206–218 (2000).
64. Eriksson, T.; Andersson, A. M.; Gejke, C.; Gustafsson, T.; Thomas, J. O. Influence of Temperature on the Interface Chemistry of LixMn2O4 Electrodes. *Langmuir* **18 (9)**, 3609–3619 (2002).
65. Edström, K., Gustafsson, T. & Thomas, J. O. The cathode-electrolyte interface in the Li-ion battery. *Electrochimica Acta* **50,** 397–403 (2004)
66. Lu, Y.-C.; Mansour, A. N.; Yabuuchi, N.; Shao-Horn, Y. Probing the Origin of Enhanced Stability of "AlPO4" Nanoparticle Coated LiCoO2 during Cycling to High Voltages: Combined XRD and XPS Studies. *Chem. Mater.* **21 (19)**, 4408–4424 (2009).
67. Yabuuchi et al., Detailed Studies of a High-Capacity Electrode Material for Rechargeable Batteries, Li2MnO3–LiCo1/3Ni1/3Mn1/3O2 *JACS* **133**, 4404–4419 (2011).
68. Browning, J. F.; Baggetto, L.; Jungjohann, K. L.; Wang, Y.; Tenhaeff, W. E.; Keum, J. K.; Wood, D. L.; Veith, G. M. In Situ Determination of the Liquid/Solid Interface Thickness and Composition for the Li Ion Cathode LiMn1.5Ni0.5O4. *ACS Appl. Mater. Interfaces* **6 (21)**, 18569–18576 (2014).
69. Cherkashinin, G.; Motzko, M.; Schulz, N.; Späth, T.; Jaegermann, W. Electron Spectroscopy Study of Li[Ni,Co,Mn]O2/Electrolyte Interface: Electronic Structure, Interface Composition, and Device Implications. *Chem. Mater.* **27 (8)**, 2875–2887 (2015).
70. Aurbach, D., Gamolsky, K., Markovsky, B., Salitra, G., Gofer, Y., Heider, U., Oesten, R., Schmidt, M. The Study of Surface Phenomena Related to Electrochemical Lithium Intercalation into Li_xMO_y Host Materials (M = Ni, Mn). *J. Electrochem. Soc.* **147**, 1322–1331 (2000).
71. O. Borodin et al. Oxidative Stability and Initial Decomposition Reactions of Carbonate, Sulfone, and Alkyl Phosphate-Based Electrolytes, *J. Phys. Chem. C* **117**, 8661-8682, (2013).
72. Tarascon et al., *In Situ* Structural and Electrochemical Study of $Ni_{1-x}Co_xO_2$ Metastable Oxides Prepared by Soft Chemistry *J.Solid State Chem.* **147**, 410–420, (1999).
73. Goodenough J. B. and Kim Y., Challenges for Rechargeable Li Batteries *Chem. Mater.* **22**, 587–603 (2010).
74. Fransson, L., Eriksson, T., Edström, K., Gustafsson, T. & Thomas, J. O. Influence of carbon black and binder on Li-ion batteries. *J. Power Sources* **101,** 1–9 (2001).
75. Lux, S. F., Pollak, E., Boesenberg, U., Richardson, T. & Kostecki, R. Electrochemical reactivity of pyrolytic carbon film electrodes in organic carbonate electrolytes. *Electrochem. Commun.* **46,** 5–8 (2014).
76. Pasquier, A. D. *et al.* Differential Scanning Calorimetry Study of the Reactivity of Carbon Anodes in Plastic Li-Ion Batteries. *J. Electrochem. Soc.* **145,** 472–477 (1998).

77. Younesi, R. *et al.* Analysis of the Interphase on Carbon Black Formed in High Voltage Batteries. *J. Electrochem. Soc.* **162,** A1289–A1296 (2015).
78. Dedryvère, R. *et al.* Surface film formation on electrodes in a LiCoO2/graphite cell: A step by step XPS study. *J. Power Sources* **174,** 462–468 (2007).
79. Madec, L. *et al.* Effect of Sulfate Electrolyte Additives on LiNi1/3Mn1/3Co1/3O2/Graphite Pouch Cell Lifetime: Correlation between XPS Surface Studies and Electrochemical Test Results. *J. Phys. Chem. C* **118,** 29608–29622 (2014).
80. Ouatani, L. E., Dedryvère, R., Siret, C., Biensan, P. & Gonbeau, D. Effect of Vinylene Carbonate Additive in Li-Ion Batteries: Comparison of LiCoO2 / C , LiFePO4 / C , and LiCoO2 / Li4Ti5O12 Systems. J. Electrochem. Soc. **156,** A468–A477 (2009).
81. Mastin L. Quanta and Wave-Particle Duality (2009). http://www.physicsoftheuniverse.com/topics_quantum_quanta.html
82. Paynter R. XPS Theory Training INRS-ÉMT
83. Dong C-L., Guo J., Chen Y.-Y., Chang, C.-L. Soft x-ray spectroscopy probes nanomaterial-based devices *Newsroom* 1-3 (2007).
84. Ago, H. *et al.* Work Functions and Surface Functional Groups of Multiwall Carbon Nanotubes. *J. Phys. Chem. B* **103,** 8116–8121 (1999).
85. Kozlowski, C. & Sherwood, P. M. A. X-ray photoelectron-spectroscopic studies of carbon-fibre surfaces. Part 5. The effect of pH on surface oxidation. *J. Chem. Soc. Faraday Trans. 1 Phys. Chem. Condens. Phases* **81,** 2745–2756 (1985).
86. Aurbach, D. *et al.* The Study of Surface Phenomena Related to Electrochemical Lithium Intercalation into LixMOy Host Materials (M = Ni, Mn). *J. Electrochem. Soc.* **147,** 1322–1331 (2000).
87. Dupin, J.-C., Gonbeau, D., Vinatier, P. & Levasseur, A. Systematic XPS studies of metal oxides, hydroxides and peroxides. *Phys. Chem. Chem. Phys.* **2,** 1319–1324 (2000).
88. Rendek, L. J., Chottiner, G. S. & Scherson, D. A. The Reactivity of Linear Alkyl Carbonates toward Metallic Lithium X-Ray Photoelectron Spectroscopy Studies in Ultrahigh Vacuum. *J. Electrochem. Soc.* **149,** E408–E412 (2002).
89. Dupin, J. C., Gonbeau, D., Benqlilou-Moudden, H., Vinatier, P. & Levasseur, A. XPS analysis of new lithium cobalt oxide thin-films before and after lithium deintercalation. *Thin Solid Films* **384,** 23–32 (2001).
90. Appapillai, A. T., Mansour, A. N., Cho, J. & Shao-Horn, Y. Microstructure of LiCoO2 with and without 'AlPO4' Nanoparticle Coating: Combined STEM and XPS Studies. *Chem. Mater.* **19,** 5748–5757 (2007).
91. Dedryvère, R. *et al.* Surface film formation on electrodes in a LiCoO2/graphite cell: A step by step XPS study. *J. Power Sources* **174,** 462–468 (2007).
92. Bryngelsson, H., Stjerndahl, M., Gustafsson, T. & Edström, K. How dynamic is the SEI? *J. Power Sources* **174,** 970–975 (2007).
93. Verdier, S. *et al.* XPS Study on Al_2O_3 and $AlPO_4$ Coated $LiCoO_2$ Cathode Material for High-Capacity Li Ion Batteries. *J. Electrochem. Soc.* **154,** A1088–A1099 (2007).
94. Murakami, M., Yamashige, H., Arai, H., Uchimoto, Y. & Ogumi, Z. Direct Evidence of LiF Formation at Electrode/Electrolyte Interface by 7Li and 19F

Double-Resonance Solid-State NMR Spectroscopy. *Electrochem. Solid-State Lett.* **14,** A134–A137 (2011).
95. Aydinol M.K., Kohan A.F., Ceder G., Cho K., Joannopoulos J. Ab initio study of lithium intercalation in metal oxides and metal dichalcogenides *Phys. Rev. B.* **56**, 1354 (1997).
96. Gallant B., Mitchell R.R., Kwabi D.G., Zhou J., Zuin L., Thompson C.V., Shao-Horn Y. Chemical and Morphological Changes of Li-O2 Battery Electrodes upon Cycling *J Phys. Chem. C* **116**, 20800–805 (2012).
97. Qiao R., Chuang Y-D, Yan S., Yang W. Soft X-Ray Irradiation Effects of Li_2O_2, Li_2CO_3 and Li_2O Revealed by Absorption Spectroscopy *Plos One*, **7(11)**, e49182 (2012).
98. de Groot F.M.F, Grioni M., Fuggle J.C., Ghijsen J., Sawatzky G.A., Petersen H. Oxygen 1s x-ray-absorption edges of transition-metal oxides *Phys. Rev. B* **40**, 5715–23 (1989).
99. Tsai H.M., Babu P.D. et al., Comparison of electronic structures of Ru O 2 and Ir O2 nanorods investigated by x- ray absorption and scanning photoelectron microscopy *Appl. Phys. Lett.* **90**, 042108 (2007).
100. Pchelkina Z. V., Pitman A.L., Moewes A. et al. Electronic Structure of Li2RuO3 studied by LDA and LDA+DMFT calculations and soft x-ray spectroscopy *Phys. Rev. B* **91**, 115138 (2015).
101. Ensling D., Cherkashinin, Schmid S., Bhuvaneswari S., Thissen A. and Jaegermann W. *Chem. Mater.* **26**, 3948–56 (2014).
102. Hong W.T., Stoerzinger K.A., Moritz B., Devereaux T.P.,Yang W., Shao-Horn Y. Probing LaMO3 Metal and Oxygen Partial Density of States Using X-ray Emission, Absorption, and Photoelectron Spectroscopy *J. Phys. Chem. C* **119**, 2063-2072 (2015).